RSC Advances

PAPER

View Article Online
View Journal | View Issue

Cite this: *RSC Adv.*, 2025, **15**, 48261

Investigating chronic myeloid leukemia therapeutics: AI-optimized design and synthesis of 4-methylthiazole-2-amine derivatives with translocation control activity

Zaheer Ahmad,[a] Labaina Shakoor,[a] Sajid Mahmood,[b] Aneeqa Batool,[c] Nusrat Shafiq,*[c] Aniqa Moveed,[c] Syeda Aaliya Shehzadi,[d] Mohamed Mohany,[e] Lei Zhang,[f] Salim S. Al-Rejaie[g] and Humaira Razzaq[a]

A series of 4-methylthiazole-2-amine derivatives (**3a–3f**, **6g–j** and **7**) were prepared *via* a Hantzsch-type multicomponent reaction and characterized by FT-IR, ^{1}H-NMR and ^{13}C-NMR spectroscopy techniques. The cytotoxic effects of the synthesized products on the chronic myeloid leukemia K562 and U937 cell lines were tested using the MTT assay. Compounds **3a**, **3b**, **3c**, **6g**, **6h** and **6i** exhibited high cytotoxic potential with IC_{50} values ranging from 1.5 to 5 0 μM, which showed a dose-dependent inhibition. Stable ligand–receptor interaction was observed by molecular docking studies against the chosen CML-associated proteins (2GQG, 5MO4, 2AZ5 and 5MAR) with the highest docking scores obtained for **6h** and **6i** (−8.37 and −8.97 kcal mol^{-1}, respectively). Strong binding affinities (ΔG = −53.36 kcal mol^{-1}) were confirmed by MM-GBSA calculations. Further, density functional theory (by using B3LYP/6-311G basic function set) was used to gain information on the electronic configurations, HOMO–LUMO gaps and charge distribution, which favored stability of the molecules and reactivity. The combined experimental and computational findings indicated that compounds **6h** and **6i** are potential scaffolds that can be used to develop new thiazole-based anticancer agents against chronic myeloid leukemia.

Received 23rd September 2025
Accepted 20th November 2025

DOI: 10.1039/d5ra07232h

rsc.li/rsc-advances

1 Introduction

Many natural products contain five-membered heterocycles having nitrogen and sulphur heteroatoms at positions 1 and 3. For example, in vitamin B1 (1), the thiazolium ring acts as an electron sink, and its coenzyme structure is essential for the decarboxylation of α-keto acids (2). It is used as an intermediate in the preparation of drugs and dyes. The aromatic nature of the thiazole is due to the delocalization of the lone pair of electrons on the sulfur atom.[1] The most demanding and investigated class of aromatic five-membered heterocycles is thiazoles. Hantzsch and Weber were the first scientists who illustrated the structure of thiazole in 1887 (1) (Fig. 1).

Thiazoles are essential due to their countless biological and pharmaceutical properties.[2] Many thiazole drugs are antioxidant, anti-inflammatory, anti-Alzheimer, antidiabetic, antimicrobial, anti-HIV, anticancer, antihypertensive and anticonvulsant.[3] Thiazoles are also present in many clinically utilized drugs, such as abafungin (antifungal drug), ritonavir (antiretroviral drug) and sulfathiazole (antimicrobial drug).[4] Nizatidine is a drug used as antagonist and drug of neonicotinoids class act as (insects) behavior product.[5] Nitazoxanide is a broad-spectrum medication play a role in traeting the diarrhea (as antiparasitic agent)[6] and in many other work such

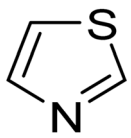

Thiazole

Fig. 1 Basic core structure of thiazole.

[a]*Department of Chemistry, University of Wah, The Quaid Avenue, Wah Cantt 47040, Pakistan. E-mail: dr.zaheer.ahmad@uow.edu.pk*

[b]*Department of Chemistry, University of Education Lahore, Vehari Campus, Vehari, Pakistan*

[c]*Synthetic and Natural Product Drug Discovery Lab., Department of Chemistry, Government College Women University, Faisalabad-3800, Pakistan. E-mail: dr.nusratshafiq@gcwuf.edu.pk; gqumarin@gmail.com*

[d]*Sulaiman Bin Abdullah Aba Al-Khail-Centre for Interdisciplinary Research in Basic Sciences (SA-CIRBS), International Islamic University, Islamabad-44000, Pakistan*

[e]*Department of Pharmacology and Toxicology, College of Pharmacy, King Saud University, P.O. Box 55760, Riyadh 11451, Saudi Arabia*

[f]*MOE International Joint Research Laboratory on Synthetic Biology and Medicines, School of Biology and Biological Engineering, South China University of Technology, Guangzhou, P. R. China*

[g]*Department of Pharmacology and Toxicology, College of Pharmacy, King Saud University, P.O. Box 55760, Riyadh 11451, Saudi Arabia*

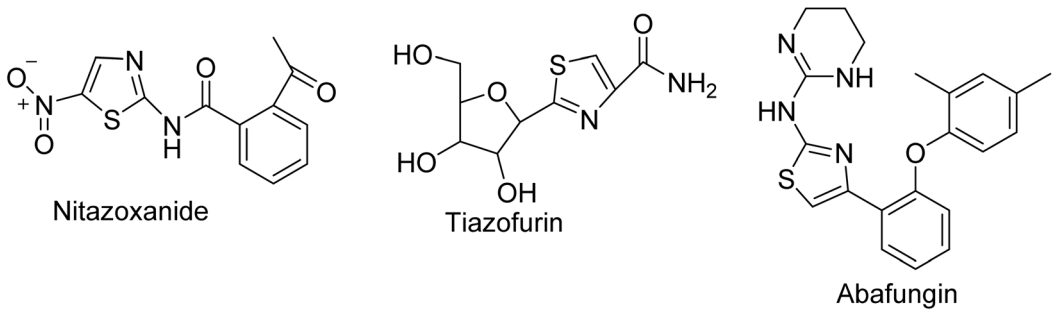

Fig. 2 Examples of thiazole-bearing drugs.

as anti-inflammatory agents. In the development of novel therapeutic agents and drug, design the most recent rumor of thiazole core structure have been put forwarded many applications (Fig. 2).

The properties of thiazoles are comparable to those of oxazoles, and the nitrogen atom with an unshared pair of electrons is vital in nature. Thiazoles holds a noticeable position within the drug innovation process among the distinctive aromatic heterocycles.[7] This ring structure is found in a few marketed drugs. Therefore, thiazoles are often included in the core structure for the amalgamation of chemical libraries.[8] Consequently, the thiazole core has been much considered within the field of medicinal and organic chemistry.

Since decades, huge populations are affected by cancer. Next to coronary disease, cancer is the second most dangerous disease. In accordance with the world health organization

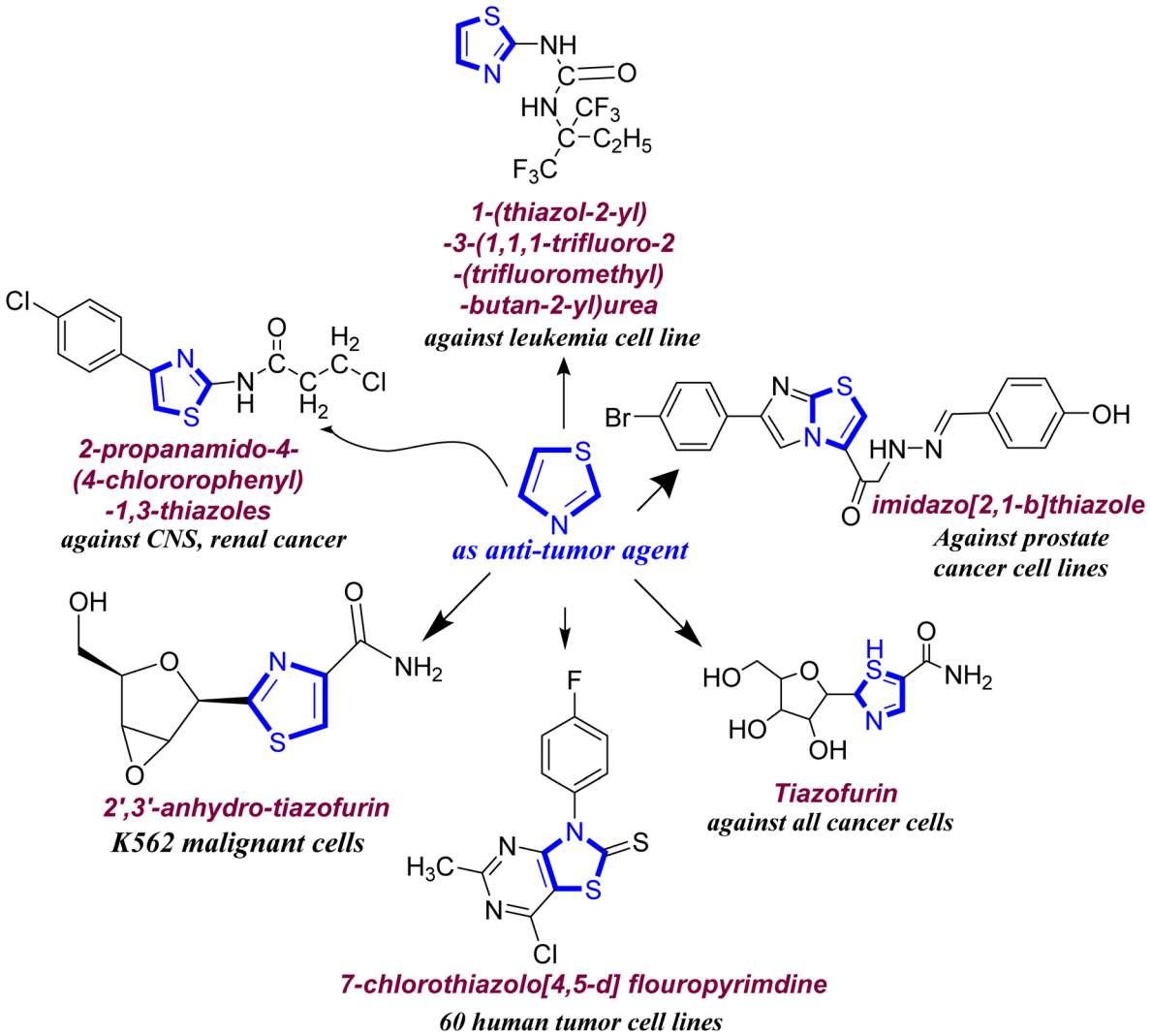

Fig. 3 Antitumor drugs containing a thiazole ring.

(WHO) report, the number of latest cases expected to increase by 70% more than two decades. Central and South America, Africa and Asia account for 60% of the world's total latest yearly cancer cases and 70% of the world's cancer deaths. By adoptation of suitable treatment for cancer control, struggle against cancer is taken as worldwide confront in this distressing condition. According to the stages and types of cancers, various treatment options such as surgery, chemotherapy, radiation therapy, targeted therapy and precision medicine, hormone therapy, immunotherapy, and stem cell transplant are available. Among all these treatment options, chemotherapy is broadly acknowledged and chosen due to its different administration routes such as oral, intraperitoneal, intravenous, intraarterial, intrathecal and topical modes.[9]

Now-a-days, most of the studies are focused on discovering the accurate target and developing potential chemotherapeutic agents for the control, treatment and eradication of this lethal disease. The medicines currently available on the market generally have nitrogen-containing heterocyclic compounds.[10] Furthermore, it is confirmed that the flexible thiazole core has significant anti-cancer effects, and is found in numerous novel chemotherapeutic agents.[11] There are numerous examples of medicines that contain the thiazole core as a fundamental structure. These drugs have revealed significant anti-cancer activities (Fig. 3).

2 Materials and methods

2.1. General procedure for the synthesis of thiazole derivatives

Different ketones having alpha hydrogen were used for the preparation of 2,4-disubtituted thiazole derivatives. The Hantzsch mechanism was followed for the preparation of thiazole derivatives. Three- and four-component single-step reactions occurred (Scheme 1).

2.1.1. General procedure for the synthesis of thiazole derivatives (3a–f). For the preparation of thiazole derivatives, a mixture of substituted ketones (0.2 mole), amides (0.2 mole), thiourea (0.3 mole) and bromine (0.2 mole) was added to a round-bottom flask and refluxed for 2 h at 110 °C. The reaction mixture was cooled to room temperature (25 °C) and then 100 mL water was added. Then, the solution was filtered off and washed with ethyl acetate to remove unreacted parts especially bromine or iodine. Excess of ethyl acetate was removed and the filtrate was poured into boiling water. Filter off the hot solution immediately. Then, it was set aside and left for half an hour. The pH of the solution was maintained at 8–9 by making it alkaline with a ammonium hydroxide solution. The products obtained were filtered. The solid product was washed sequentially with water (2 × 150 mL). Aqueous ethanol (1 : 1) was used to crystallize the product (Scheme 2).

2.1.2. General procedure for the synthesis of compounds 6g–j. A mixture of amino thiazole derivatives (0.02 mole) and chloroacetyl chloride (0.5 g) in 20 mL DCM was taken in a 200 mL round-bottom flask. Sodium bicarbonate ($NaHCO_3$) was added to the mixture and refluxed for several hours with constant stirring. After completion, the reaction mixture was poured into ice-cold water (200 mL). Then the precipitate was filtered-off and crystalized with ethanol (Scheme 3).

2.1.3. General procedure for the synthesis of azothiazole (7). For the synthesis of azothiazole (7) (Scheme 4), an aqueous solution of $NaNO_2$ and acidic solution of aniline were prepared. Then, 0.01 mole of $NaNO_2$ in 12.5 mL water and 0.01 mole of $C_6H_5NH_2$ in 7.5 mL of hydrochloric acid were prepared. Then,

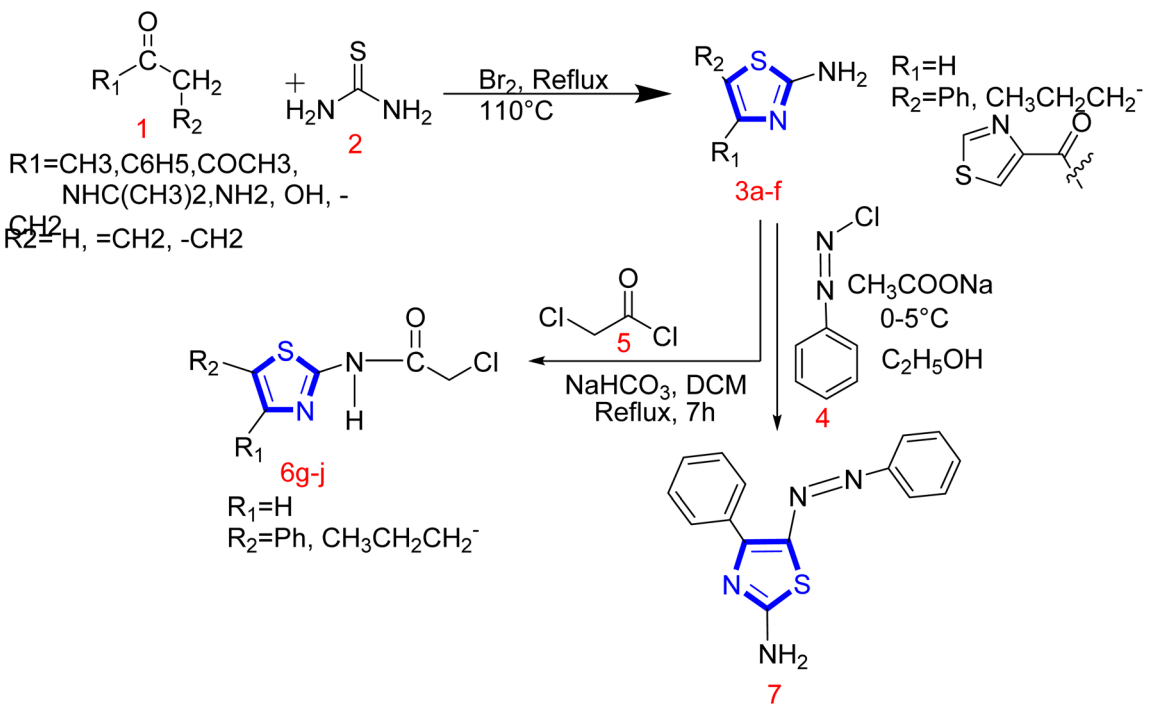

Scheme 1 General reaction mechanism for the synthesis of thiazole derivatives followed by the Hantzch synthesis.

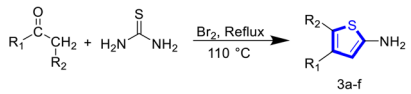

Different functional groups attached to the R_1 and R_2 positions in compounds.			
S. no.	Compounds	R_1	R_2
1	**3a**	$-CH_3$	–H
2	**3b**	$-C_6H_5$	–H
3	**3c**	$-NH_2$	$=CH_2$
4	**3d**	$-CH_2$	$-CH_2$
5	**3e**	$-COCH_3$	H
6	**3f**	$-NH(CH_3)_2$	$=CH_2$

Scheme 2 General reaction for the preparation of thiazole derivatives (3a–f).

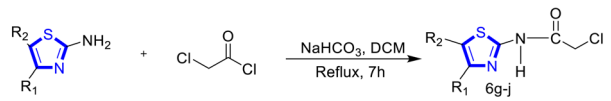

Different functional groups attached to the R_1 and R_2 positions in compounds.			
S. no.	Compound	R_1	R_2
1	**6g**	$-CH_3$	H
2	**6h**	$-C_6H_5$	H
3	**6i**	$-CH_2-$	$-CH_2-$
4	**6j**	$-COCH_3$	H

Scheme 3 General reaction of compounds 7d–e.

a $NaNO_2$ solution was added to an aniline solution drop-wise maintaining at 5 °C, and a diazonium salt was formed. A diazonium salt was added to cool the mixture of 2-amino-4-phenyl thiazole (0.01 mole) and 7.5 g of CH_3COONa in ethanol. The reaction mixture was continuously stirred at a temperature of 5 °C for 2 h. Water was added to the mixture, and the solution was filtered. A solid mass was washed with water and recrystallized with aqueous ethanol (9 : 1).

2.2. Characterization of the targeted synthesized compounds (3a–f, 6g–j and 7)

2.2.1. 2-Amino-4-methylthiazole (3a). Physical appearance: white crystals; yield: 74.5%; RF value: 0.75; FTIR (cm^{-1}): 3370.24 ($-NH_{stretch}$), 1590.53 (C=N), 1083.20 (C–$N_{stretch}$), 2962.08 ($CH_{stretch}$), 1406.71 (C=C_{ring}), 730.04 (thiazole nucleus); ^{1}HNMR (DMSO, 300 MHz): δ 7.06 (s, 2H, 2-NH_2), 6.48 (s, 1H, H-5), 2.28 (s, 3H, 4-CH_3); ^{13}CNMR (DMSO, 125 MHz): δ 169.1 (C-2), 147.8 (C-4), 101.3 (C-5), 16.8 (4-CH_3); molecular formula: $C_4H_6N_2S$; molecular weight: 114.17 g mol^{-1}.

2.2.2. 2-Amino-4-phenyl thiazole (3b). Physical appearance: yellow crystals; yield: 80%; RF value: 0.69; FT-IR (cm^{-1}): 3249.51 ($NH_{stretch}$); 1596.71 (C=N); 1021.65 (C–$N_{stretch}$); 1530.66 (C=$C_{aromatic}$); 1440.74 (C=C_{ring}); 710.95 (thiazole nucleus); ^{1}HNMR (DMSO, 300 MHz) δ 6.998 (s, $-NH_2$), 7.78 (dd, J = 2.00 Hz, 2H, H-7, 11), 7.38 (d, 2H, J = 2.04 Hz, H-8, 10), 7.27 (dd, 1H, J = 1.02 Hz, H-9), 7.074 (s, 1H, H-5); ^{13}CNMR (DMSO, 125 MHz): δ 168.6 (C-2), 150.29 (C-4), 125.98 (C-9), 127.63 (C-7, 11), 128.92 (C-8, 10), 135.38 (C-6), 101.94 (C-5); molecular formula: $C_9H_8N_2S$; molecular weight: 176.24 g mol^{-1}.

2.2.3. Bis-(2-aminothiazole-4-yl)-methanone (3c). Physical appearance: brown crystals; yield: 83%; RF value: 0.89; FT-IR value: 3318.45 ($NH_{stretch}$), 1655.26 (C=N), 1129.41 (C–$N_{stretch}$), 1706.78 (C=$O_{stretch}$), St of thiazole nucleus, 720.08; C=C (ring), 1430.75; ^{1}HNMR (DMSO, 300 MHz): δ 6.99 (s, 4H, 2,2′-NH_2), 8.38 (s, 2H, H-5,5′); ^{13}CNMR (DMSO, 125 MHz): δ 194.9 (C-6), 168.9 (C-2,2′), 144.9 (C-4,4′), 113.5 (C-5,5′); molecular formula: $C_7H_6N_4S_2O$; molecular weight: 226.00 g mol^{-1}.

2.2.4. N^4-Isopropyl-5-methylene-4,5-dihydrothiazole-2-4-diamine (3d). Physical appearance: green crystals; yield: 76.5%; RF value: 0.67; FTIR (cm^{-1}): 3277.59 ($NH_{stretch}$), 1620.42 (C=N), 1153.88 (C–$N_{stretch}$), 1253.89 ($CH_{aromatic}$), 1650.82 (C=C_{ring}), 1549.06_(NH_{bend}) ($CH_{stretch}$), 2876.22 (CH_3), 2932.69 ($CH_{stretch}$) 727.51 (thiazole nucleus); ^{1}HNMR (DMSO, 300 MHz): δ 7.06 (s, 2H, $-NH_2$), 6.48 (s, 1H, H-5), 2.28 (s, 3H, 4-CH_3); ^{13}CNMR (DMSO, 125 MHz): δ 169.1 (C-2), 147.8 (C-4), 101.3 (C-5), 16.8 (4-CH_3); molecular formula: $C_7H_{13}N_3S$; molecular weight: 171.26 g mol^{-1}.

2.2.5. 5,6-Dihydro-4*H*-cyclopenta[*d*]thiazole-2-amine (3e). Physical Appearance: white powder; yield: 79%; RF value: 0.61; FTIR (cm^{-1}): 3376.24 ($NH_{stretch}$), 1608.08 (C=N), 1081.78 (C–$N_{stretch}$), 3147.59 ($CH_{aromatic}$), 1441.36 (C=C_{ring}), 727.51 (thiazole nucleus); ^{1}HNMR (DMSO, 300 MHz): δ 7.06 (s, 2H, $-NH_2$), 6.48 (s, 1H, H-5), 2.28 (s, 3H, 4-CH_3); ^{13}CNMR (DMSO, 125 MHz): δ 169.1 (C-2), 147.8 (C-4), 101.3 (C-5), 16.8 (4-CH_3); molecular formula: $C_6H_8N_2S$; molecular weight: 140.21 g mol^{-1}.

2.2.6. 5-Methylene-4-5-dihydrothiazole-2-4-diamine (3f). Physical Appearance: white crystals; yield: 83.6%; RF value: 0.61; FTIR (cm^{-1}): 3346.20 ($NH_{stretch}$), 1602.63 (C=N), 1081.30 (C–$N_{stretch}$), 3118.98 ($CH_{aromatic}$), 1665.89 (C=C_{ring}), 727.51 (thiazole nucleus); ^{1}HNMR (DMSO, 300 MHz): δ 7.06 (s, 2H, $-NH_2$), 6.48 (s, 1H, H-5), 2.28 (s, 3H, 4-CH_3); ^{13}CNMR (DMSO, 125 MHz): δ 169.1 (C-2), 147.8 (C-4), 101.3 (C-5), 16.8 (4-CH_3); molecular formula: $C_4H_7N_3S$; molecular weight: 129.18 g mol^{-1}.

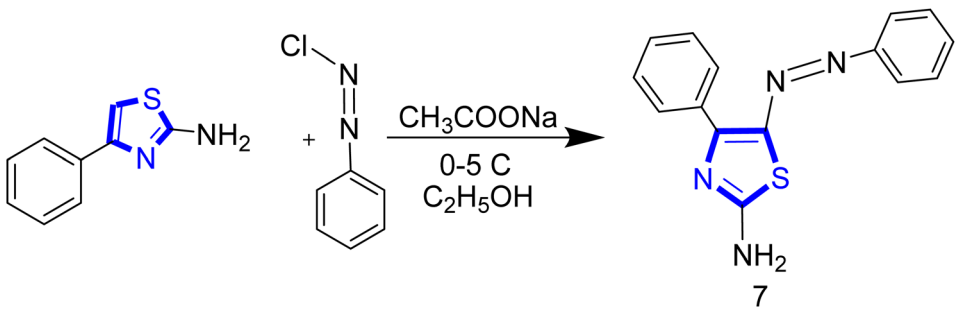

Scheme 4 Reaction for the preparation of azothiazole (7).

2.2.7. 2-Chloro-*N*-(4-phenylthiazole-2-yl)acetamide (6g). Physical appearance: brownish crystals; yield: 80%; RF value: 0.70; FT-IR value: 3249.36 ($N–H_{stretch}$), 1566.86 (C=N), 1137.87 (C–N), 1263.03 ($C–N_{aromatic}$), 1654.79 ($C=O_{stretch}$), 1566.86 ($CH_{aromatic}$), 669.81 ($Cl_{stretch}$), 718.66 (thiazolo nucleus); ^{1}HNMR (DMSO, 300 MHz): δ 12.68 (s, 2H, NH_2-2), 7.92 (dd, 2H J = 1 Hz, H-7,11), 7.45 (dd, 2H, J = 0.94 Hz, H-8,10), 7.34 (dd, 1H, J = 0.58 Hz, H-9), 7.67 (s, 1H, H-5), 4.43 (s, 2H, CH_2-12); ^{13}CNMR (DMSO, 125 MHz): δ 165.6 (C=O), 157.92 (C-2), 149.53 (C-4), 134.58 (C-6), 129.22 (C-8,10), 128.35 (C-7,11), 126.15 (C-9), 109.03 (C-5), 42.79 (–CH_2); molecular formula: $C_{11}H_9ClN_2OS$; molecular weight: 252.72 g mol^{-1}.

2.2.8. 2-Chloro-*N*-(5,6-dihydro-4*H* cyclopenta[*d*]thiazol-2-yl)acetamide (6h). Physical appearance: yellow crystals; yield: 78%; RF value: 0.78; FT-IR (cm^{-1}): 3319.15 ($NH_{stretch}$), 1584.04 ($NH_{bending}$), 1640.60 ($C=N_{stretch}$), 1228.02 ($C–N_{aromatic}$); 1117.57 ($CN_{stretch}$), 1667.22 ($C=O_{stretch}$), 2979.28 ($CH_{aromatic}$), 672.37 ($Cl_{stretch}$); ^{1}HNMR (DMSO, 300 MHz): δ 12.5 (2H, s, 2-NH_2), 2.87 (2H, t, 6-CH_2), 2.54 (2H, m, 7-CH_2), 2.52 (2H, m, 8-CH_2); ^{13}CNMR (DMSO, 125 MHz): δ 164.2 (C=O), 148.2 (C-4), 118.9 (C-5), 28.2 (C-6), 26.0 (C-7), 30.9 (C-8); molecular formula: $C_8H_9ClN_2OS$; molecular weight: 216.69 g mol^{-1}.

2.2.9. *N*,*N*′-(4,4′-Carbonylbis(thiazole-4,2-diyl))bis(2-chloroacetamide) (6i). Physical appearance: grey powder; yield: 73%; RF value: 0.57; FTIR (cm^{-1}): 3383.72 ($NH_{stretch}$), 1574.54 ($NH_{bending}$), 1630.14 ($C=N_{stretch}$), 1224.23 ($C–N_{aromatic}$), 1118.70 ($C–N_{stretch}$), 1654.82 ($C=O_{stretch}$), 670.82 ($Cl_{stretch}$); ^{1}HNMR (DMSO, 300 MHz): δ 12.4 (2H, s, 2,2′-NH), 4.87 (4H, t, 8,8′-CH_2), 8.98 (2H, s, 5,5′-CH_2); ^{13}CNMR (DMSO, 125 MHz): δ 192.9 (C-9), 164.5 (C-7,7′), 144.2 (C-4,4′), 113.9 (C-5,5′), 42.7 (C-8,8′), 26.0 (C-7), 30.9 (C-8); molecular formula: $C_{11}H_{10}ClN_4O_3S_2$; molecular weight: 379.23 g mol^{-1}.

2.2.10. 2-Chloro-*N*-(4-methylthiazole-2-yl)acetamide (6j). Physical appearance: white powder; yield: 82%; RF value: 0.59; FTIR (cm^{-1}): 3264.01 ($N–H_{stretch}$), 1582.5 (C=N), 1072.49 ($C–N_{stretch}$), 1287.11 ($C–N_{aromatic}$), 1683.96 ($C=O_{stretch}$), 2919.77 ($CH_{stretch}$), 670.34 ($Cl_{stretch}$), 722.57 (thiazole nucleus); ^{1}HNMR (DMSO, 300 MHz): δ 12.68 (s, 1H, 6-NH-), 7.67 (s, 1H, H-5), 4.43 (s, 2H, CH_2-8); ^{13}CNMR (DMSO, 125 MHz): δ 165.6 (C=O), 162.92 (C-2), 144.7 (C-4), 104.3 (C-5), 42.79 (8-CH_2) molecular formula: $C_6H_7ClN_2OS$; molecular weight: 190.65 g mol^{-1}.

2.2.11. 4-Phenyl-5-(phenyldiazenyl)thiazole-2-amine (7). Physical appearance: grey powder; yield: 69%; RF value: 0.66 FT-

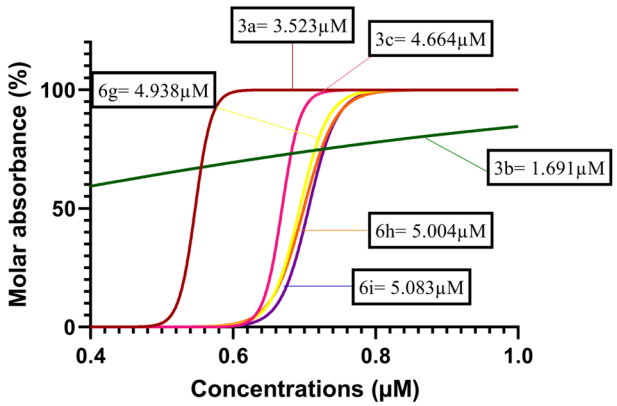

Fig. 4 Graphical representation of the K562 cell line inhibitory concentration of the synthesized drugs.

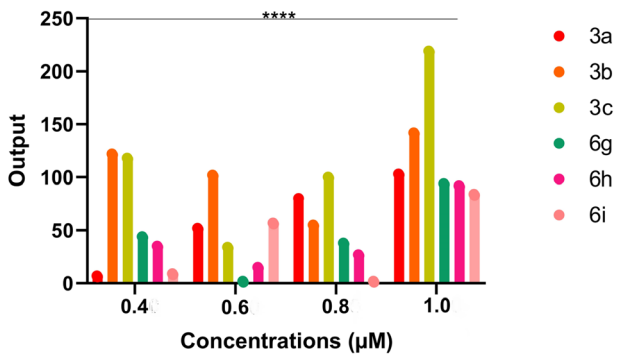

Fig. 5 Graphical representation of two-way ANOVA of all the synthesized drugs against the K562 cell line.

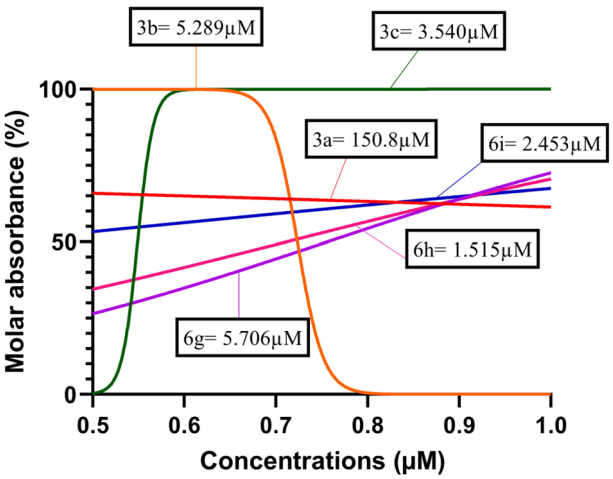

Fig. 6 Graphical representation of the U937 cell line inhibitory concentration of the synthesized drugs.

Table 1 Two-way ANOVA results of all the synthesized drugs against the K562 cell line

ANOVA table	SS	DF	MS	F (DFn, DFd)	P Value
Interaction	30 666	15	2044	F (15, 24) = 4089	P < 0.0001
Row factor	47 982	3	15 994	F (3, 24) = 31 988	P < 0.0001
Column factor	48 244	5	9649	F (5, 24) = 19 297	P < 0.0001
Residual	12.00	24	0.5000		

Table 2 Two-way ANOVA of all the synthesized drugs against the U937 cell line

ANOVA table	SS	DF	MS	*F* (DFn, DFd)	*P* Value
Interaction	120 506	15	8034	$F(15, 24) = 12\,051$	$P < 0.0001$
Row factor	86 859	3	28 953	$F(3, 24) = 43\,429$	$P < 0.0001$
Column factor	50 671	5	10 134	$F(5, 24) = 15\,201$	$P < 0.0001$
Residual	16.00	24	0.6667		

IR value: 3246.76 ($NH_{stretch}$), 1597.30 (C=N), 1038 ($C–N_{stretch}$), 1282.04 ($C–N_{aromatic}$), 1517.64 (N=N), 1483.26 ($CH_{aromatic}$), 1441.32 ($C=C_{aromatic}$), 772.17 (thiazolo nucleus); ^{1}HNMR (DMSO, 300 MHz): δ 8.61 (2H, s, 2-NH_2), 8.20 (2H, dd, J = 8, 1.0 Hz, H-7,11), 7.38 (2H, dd, J = 1.0, 2.5 Hz, H-8,10), 7.45 (1H, ddd, J = 1.5 Hz, 2.5 Hz, H-9), 7.26 (2H, dd, J = 8.5, 1.0 Hz, H-7′, 11′), 7.34 (2H, dd, J = 8.0 Hz, H-8′,10′), 7.10 (1H, dd, J = 8.0 Hz, H-9′); ^{13}CNMR (DMSO, 125 MHz): δ 1770.2 (C-2), 154.4 (C-4), 138.0 (C-5), 133.1 C-6), 126.1 (C-7,11), 128.9 (C-8,10), 128.6 (C-9), 128.6 (C-6′), 127.9 (C-7′,11′), 128.6 (C-8′, 10′), 126.2 (C-9′) molecular formula: $C_{15}H_{12}N_4S$; molecular weight: 280.35 g mol^{-1}.

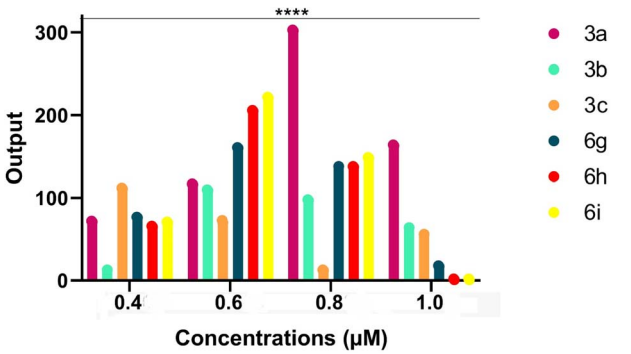

Fig. 7 Graphical representation of the U937 cell line inhibitory concentration of the synthesized drugs.

2.3. Anti-tumor activity of the synthesized compounds

Different thiazole derivatives were prepared and screened by the MTT assay.[12] For this purpose, two chronic myeloid leukemia model cell lines, namely, K562 and U937, were selected as translocation controls. The targeted cell lines were purchased from the German Collection of Microorganisms and Cell Cultures (DSMZ, Braunschweig, Germany) through the local vendor (Musaji Adam & Sons, Lahore). RPMI1640 media

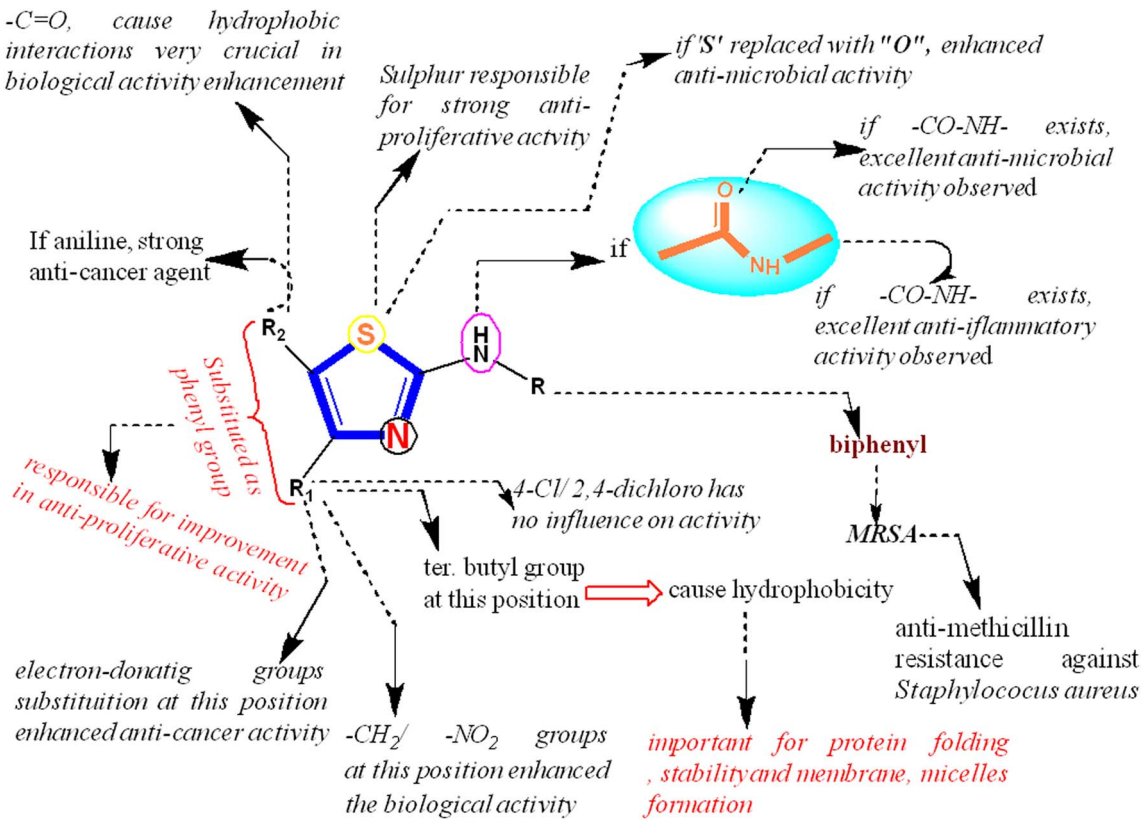

Fig. 8 Structure–activity relationship of thaizole derivatives.

Table 3 Docking scores with the corresponding interactions

S. no.	PDB ID	Compounds	Docking score	Type of interaction	Amino acid residue	Distance
1	2GQG	5-Fluorouracil	−7.064	H-bond	MET318	1.91
				H-bond	MET318	1.86
		3a	−6.727	H-bond	MET318	2.38
				H-bond	MET318	1.83
		3b	−6.245	H-bond	LEU248	2.42
		3c	−6.472	H-bond	GLU286	2.42
		3d	−6.147	H-bond	GLU286	1.89
		3e	−7.688	H-bond	MET318	2.21
				H-bond	MET318	1.88
		3f	−7.606	H-bond	MET318	2.20
				H-bond	MET318	2.21
				H-bond	GLU316	1.87
		6g	−6.700	H-bond	THR315	2.18
		6h	−8.370	H-bond	MET318	2.28
				H-bond	MET318	1.87
		6i	−8.973	H-bond	MET318	2.09
				H-bond	THR315	2.28
				Halogen bond	TYR253	3.19
				Halogen bond	GLY251	3.09
		6j	−7.284	H-bond	MET318	2.40
				H-bond	MET318	1.86
		7	−7.184	H-bond	GLU316	1.78
2	5MO4	5-Fluorouracil	−6.329	H-bond	MET337	2.10
				Pi–Pi stacking	TYR272	5.02
		3a	−5.590	—	—	—
		3b	−7.447	Pi–Pi stacking	TYR272	4.81
		3c	−5.870	H-bond	ASP400	2.32
		3d	−6.741	H-bond	GLU305	2.63
		3e	−6.791	H-bond	MET337	2.22
				Pi–Pi stacking	TYR272	5.14
		3f	−6.212	H-bond	ALA288	2.18
				H-bond	ILE332	2.12
		6g	−8.441	H-bond	ASP400	2.32
				Pi–Pi stacking	TYR272	5.03
		6h	−7.292	H-bond	ASP400	1.88
				Pi-cation	LYS290	6.55
		6i	−7.384	H-bond	ASP400	2.40
				H-bond	GLU305	2.24
		6j	−6.154	H-bond	ASP400	2.55
		7	−6.044	—	—	—
3	2AZ5	5-Fluorouracil	−5.598	H-bond	TYR B:151	1.97
				H-bond	LEU B:120	2.74
		3a	−4.960	H-bond	SER B:60	2.06
				Pi–Pi stacking	TYR B:119	4.98
		3b	−5.923	H-bond	LEU A:120	1.85
				Pi–Pi stacking	TYR B:119	5.35
		3c	−5.054	H-bond	LEU A:120	2.27
				H-bond	LEU A:120	2.16
				H-bond	SER B:60	2.47
				Pi–Pi stacking	TYR B:119	5.12
		3d	−5.335	H-bond	SER B:60	2.22
		3e	−5.494	H-bond	GLY A:121	1.99
		3f	−5.613	H-bond	GLY A:121	1.84
				H-bond	TYR B:151	2.34
		6g	−5.339	H-bond	LEU A:120	3.47
				Pi–Pi stacking	TYR A:59	4.18
		6h	−5.838	—	—	—
		6i	−5.118	Halogen bond	TYR B:119	3.42
				H-bond	GLY A:121	2.34
		6j	−5.030	H-bond	GLY A:121	2.19
		7	−6.289	H-bond	SER A:60	2.19
				Pi–Pi stacking	TYR B:59	5.09
				Pi–Pi stacking	TYR B:119	5.49

Table 3 (*Contd.*)

S. no.	PDB ID	Compounds	Docking score	Type of interaction	Amino acid residue	Distance
4	5MAR	5-Fluorouracil	−6.676	H-bond	LYS 287	2.19
				H-bond	ASN286	1.85
				H-bond	ASP95	1.68
		3a	−5.130	H-bond	ALA85	2.73
				H-bond	GLY261	2.12
		3b	−4.653	H-bond	SER263	2.65
		3c	−6.292	H-bond	GLU288	1.83
				H-bond	ARG97	2.01
				H-bond	PHE96	1.89
		3d	−5.071	H-bond	ASP95	1.95
				H-bond	GLU288	2.07
		3e	−5.246	H-bond	ALA85	2.37
		3f	−5.528	H-bond	GLU288	1.68
				H-bond	ASN286	2.09
		6g	−5.398	Halogen bond	ARG97	2.82
				Halogen bond	TYR104	2.42
		6h	−5.977	H-bond	SER263	2.56
				H-bond	ALA85	2.28
		6i	−5.535	H-bond	ARG A:97	2.60
				H-bond	SER A:263	2.04
				H-bond	HIS A:187	2.31
				Halogen bond	ARG A:97	3.48
				Halogen bond	TYR A:104	2.59
		6j	−5.534	H-bond	SER263	2.21
				H-bond	ALA85	1.97
				Halogen bond	ARG97	2.64
		7	−4.378	—	—	—

supplemented with 10% fetal bovine serum (FBS; Gibco/Invitrogen, Karlsruhe, Germany), 1% penicillin/streptomycin (P/S) and 1% L-glutamine were used to culture the cell lines. This assay was performed using a previously reported method.[12] For this purpose, the compounds at concentrations of 0.4 μM, 0.6 μM, 0.8 μM, and 1.0 μM were used. The cell viability was calculated, IC_{50} was determined using GraphPad Prism and further statistical analyses of results were done by applying two-way ANOVA for the proper presentation of results.

2.4. Molecular docking study

Molecular docking of the synthesized compounds from thiazole and azothiazol was performed using Maestro Schrodinger 13.4. The protein structures are generally refined for their topologies, incomplete and terminal amide groups, bond ordering, formal charges and missing hydrogen atoms.[13] Water molecules larger than 5 Å were eliminated. The most stable ionization states that were produced in the protein structure were selected. The orientations of the remaining water molecules were adjusted.[14] Lastly, the protein structure was minimized by reorienting side-chain hydroxyl groups and steric conflicts using the OPLS2005 force field.[15]

2.4.1. Ligand preparation. A dataset of thiazole derivatives were prepared by the synthesis of thiazole and azothiazol. Thiazole derivative structures were identified by the characterization of these compounds. The structures were drawn by using ChemDraw (ChemDraw 19.1), then names, and smiles of these thiazole derivatives were generated (as shown in Table S1 (SI)). For molecular docking, thiazole derivatives are saved in the SDF format along with the reference drug. The Maestro Schrodinger suite 2022 software was used for ligand preparation through the LigPrep interface.[16] By follwoing the Schrodinger software's specifications, all ligands were selected from the workspace, eliminate the tautomer, neutralize and create the ligand.[17]

2.4.2. Receptor grid generation. For receptor grid generation, the ligands remained in the crystal structure of the prepared protein. For checking the accuracy of docking studies, the lowest energy pose of the co-crystallized ligands was determined by the scoring function, which closely reflects the experimental binding mode determined by X-ray crystallography.[17] The co-crystallized ligand was separated from the protein's binding site using the Glide docking approach. The receptor grid and the ligands were used to perform the glide docking of the synthesized compounds.[18]

We used the Maestro Schrodinger version 13.5 software, which use the step wise preparation by following the sequence of protein preparation, receptor grid generation, ligand preparation and docking. Protein amino acid interaction with receptor (ligand) was enclosed by active site grid.[19] Through molecular docking study, these ligands were converted into 3D structures and the best docking score was recorded.

2.5. MM-GBSA calculation

Ligand–protein complexes were subjected to MM-GBSA built in Maestro Schrodinger 13.5 version to calculate the binding

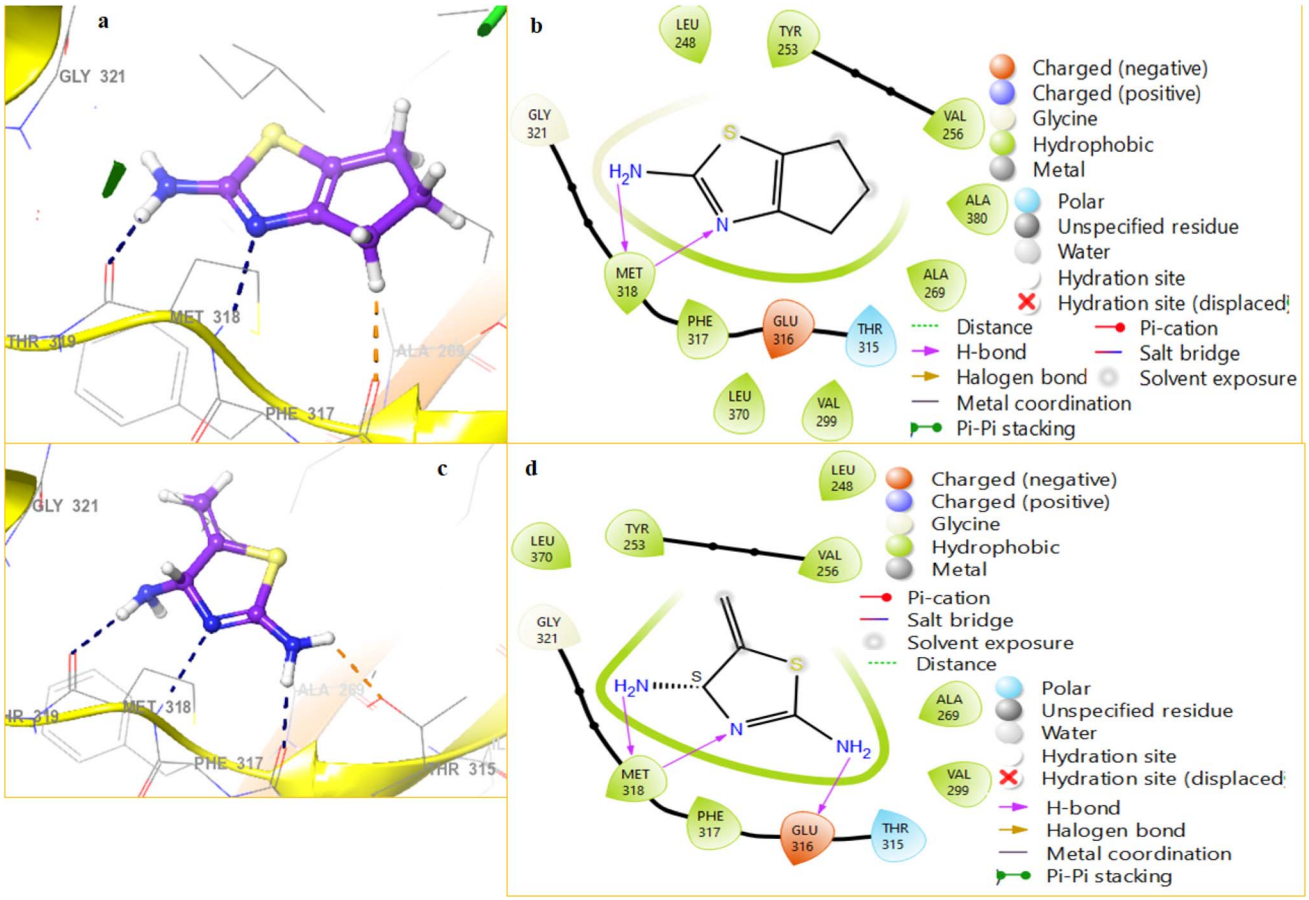

Fig. 9 (a) 3D-interaction of **3e** in complex with the protein 2GQG; (b) 2D interaction of **3e** in complex with the protein 2GQG; (c) 3D interaction of **3f** in complex with the protein 2GQG; and (d) 2D interaction of **3f** in complex with the protein 2GQG.

energy. Using this software, proteins were prepared by the removal of water and minimization of H-bonds, and ligands were also prepared by the LigPrep tool using the OPLS2005 force field.[20] Ligand–protein complexes were optimized using Prime with the OPLS 2005 force field. Different factors of energies were calculated for the MM-GBSA study such as binding free energy, coulomb binding free energy, covalent binding free energy, hydrogen bond binding free energy and lipophilic binding free energy.[21]

2.6. Optimization of geometry parameters and spectral data by DFT studies

Density functional theory (DFT) calculations were performed to check the optimization geometry of the compounds using the Gaussian 09W and Gauss View 6.0.16 software. The B3LYP 6-311G basis set was used to calculate the energy gap between the LUMO and HOMO orbitals and the stability and reactivity of the compounds.[22]

2.6.1. Computational details of the protocol. Theoretical analyses of compounds **6h** (2-chloro-*N*-(5,6-dihydro-4*H* cyclopenta[*d*]thiazol-2-yl)acetamide) and **6i** (*N*,*N*′-(4,4′-carbonylbis(thiazole-4,2-diyl))bis(2-chloroacetamide)) were performed using the Gaussian and Gauss View program.[23] Geometry optimization and frequency calculation were also conducted by the density functional theory (DFT) calculation of quantum mechanics with the B3LYP parameter and the 6-311G basis set as correlation functions.[24] The B3LYP model gives the stable IR and NMR DFT calculations with good experimental calculation of IR and NMR according to studies. Transition energies of the lowest unoccupied molecular orbital (LUMO) and the highest occupied molecular orbital (HOMO), energy gap, FMO, MEP, dipole moments and other properties were calculated using this model.[25] The vibrational data of IR obtained from the Gauss View was computed to Origin program to generate the IR spectra. Proton and carbon NMR spectra were generated using the GIAO (gauge independent atomic orbital) approach and compared with the experimental calculations. Using tetramethylsilane (TMS HF/6-31G(d)) GIAO as the internal reference, the optimized parameters obtained from the B3LYP/6 311G method were used to determine the proton and carbon isotropic shielding.[26] The natural bond orbital (NBO) was obtained using the second order of perturbation theory from the B3LYP 6-311G basis set. Further studies of natural population analysis (NPA) and Mulliken's population analysis (MPA) were calculated from the second order of perturbation theory NBOs.[27]

2.6.2. Hirshfeld population analysis. To check the charge distribution at the atomic level and understand the non-covalent

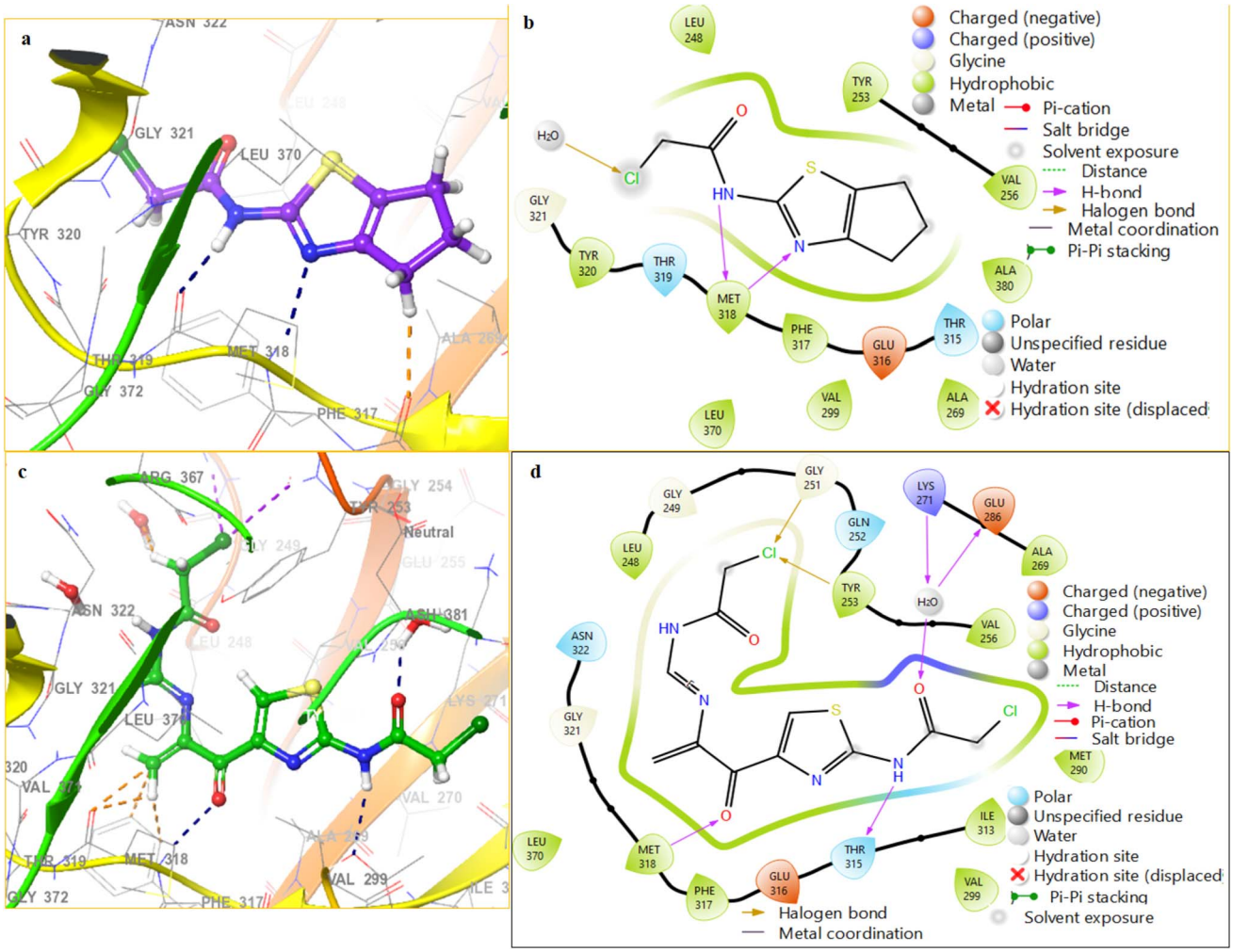

Fig. 10 (a) 3D interaction of **6h** in complex with the protein 2GQG; (b) 2D interaction of **6h** in complex with the protein 2GQG; (c) 3D interaction of **6i** in complex with the protein 2GQG; and (d) 2D interaction of **6i** in complex with the protein 2GQG.

nature of compounds **6h** and **6i**, the Hirshfeld surface population analysis and CM5 atomic charge calculation were performed on the basis of the DFT results. All the optimization of geometry for targeted compounds **6h** and **6i** was done at the B3LYP 6-311G level using the Gaussian 09W software. The components of dipole moment (D_x, D_y, and D_z), Hirshfeld atomic charges (Q-H) and CM5 charges (Q-CM5) were determined from the converged wave-function through the population analysis tools, and further process proceeded with Multiwfn.[28] This study gave an idea about partial atomic charges and charge separation directions in the molecule that are fundamental to explaining the electrostatic interactions, intra-molecular polarization and ability to bind with biological targets.[29] Red color area indicates the atoms with positive dipole contributions and blue to violet color area indicates the negative dipole contributions, consistent with the electron-withdrawing or electron-donating characteristics.[30] The gradient in the plot, observed as red (e^--poor) to blue (e^--rich) direction, indicates significant polarization in the molecular structure, which could have a significant impact on the orientation and strength of the non-covalent interactions in the biological context.

2.6.3. Non-covalent bond interactions (NCI) study. Non-covalent interactions (NCI) for targeted compounds **6h** and **6i** were analyzed by the reduced density gradient (RDG) analysis due to the density of electrons, which was calculated by the density functional theory (DFT) calculation. The optimized geometry of compounds **6h** and **6i** was determined using the Gaussian software at the B3LYP 6-311G level. The respective wave function (wfn) file was created and used for RDG analysis. The mathematical operations were performed by applying the Multiwfn program that calculates the value of RDG and also determines the area of weak interactions within the molecular system.[31] The visualization of the RDG isosurfaces was performed using the Visual Molecular Dynamics (VMD) software. This tool set can offer this kind of in-depth analysis of several non-covalent forces, such as van der Waals forces, hydrogen bonding and steric effects, by studying the distribution of electron density and gradient.[32]

2.6.4. Electron localization function (ELF) and localized orbital locator (LOL). The electronic structure of the **6h** and **6i** compounds was determined in the framework of density functional theory (DFT), providing insights into the character of

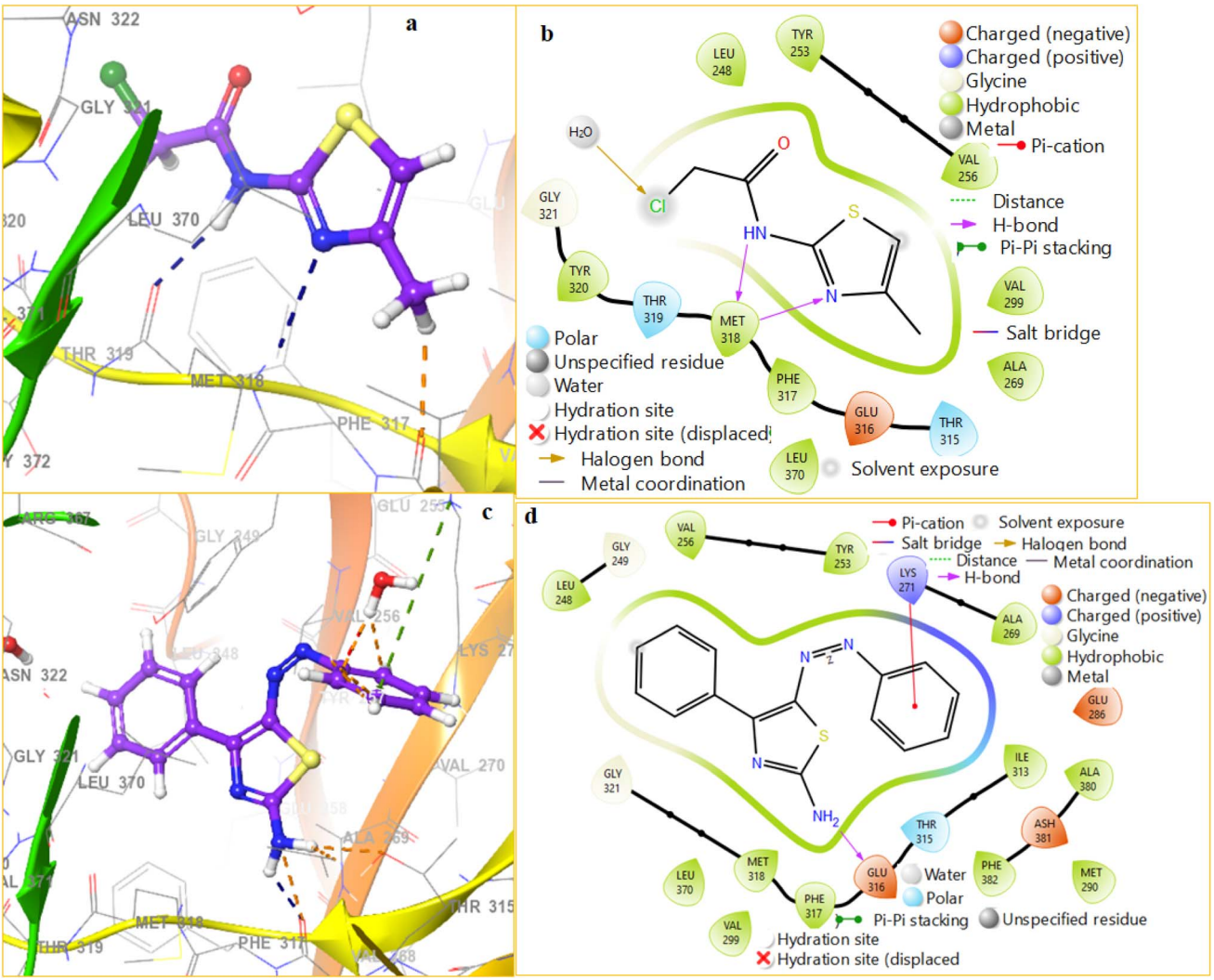

Fig. 11 (a) 3D interaction of **6j** in complex with the protein 2GQG; (b) 2D interaction of **6j** in complex with the protein 2GQG; (c) 3D interaction of compound **7** in complex with the protein 2GQG; and (d) 2D interaction of compound **7** in complex with the protein 2GQG.

electron localization and bonding interaction of these compounds as well as their electron localization function (ELF) and localized orbital locator (LOL). These gauges allow precious information about covalent bonding, lone pairs and delocalized electrons and ELF gives an indication of the likelihood of occurrence of electron pairs and the LOL looks at the distribution of kinetic energy density.[33] A set of ELF and LOL calculations were performed using the Multiwfn program, allowing a quantitative and visual analysis of the features of the localization of the wavefunctions and their convergence with the DFT results.[34] The resulting 3D isosurfaces and contour plots were visualized in VMD (Visual Molecular Dynamics), which made the bonding environments of the **6h** and **6i** structures clear to interpret.

3 Results and discussion

3.1. Chemistry

The synthesized compounds were characterized for their structure by spectroscopic analysis. The FT-IR spectral data of all compounds displayed characteristic peaks of the thiazole nucleus at 772.17 cm^{-1} to 672.37 cm^{-1} with other functional group peaks like –NH and –C=C– at their specific values compared to the literature. The ^{1}H-NMR spectral data of compound **3a** displayed a singlet at δ 7.06 ppm for the amino group with two more singlets at 6.48 ppm and 2.28 ppm for the ring proton and methyl moiety present at the 5-position of the ring, respectively. The ^{13}C-NMR spectra were also found in accordance with the ^{1}H-NMR data displaying a specific carbon signal at δ 169.1 ppm for quarterly carbon attached to an amino group shifting downfield. A signal was observed at δ 147.8 ppm corresponding to the carbon attached to a methyl group whose signal at δ 16.8 ppm and a signal at δ 101.3 ppm correspond to the methane proton.[35] The spectral data of **3b** and **3c** were also found to be similar to **3a** except the presence of a phenyl ring in place of methyl in compound **3b** and the presence of a carbonyl group with the double signals of the thaizole skeleton, confirming the dimer of compound **3c**. Basic spectral signals of compounds **3d**, **3e** and **3f** were found to be similar to **3a** except the additional signals of substituents found in them. Similarly, the ^{1}H-NMR spectra of compound **7** displayed the additional

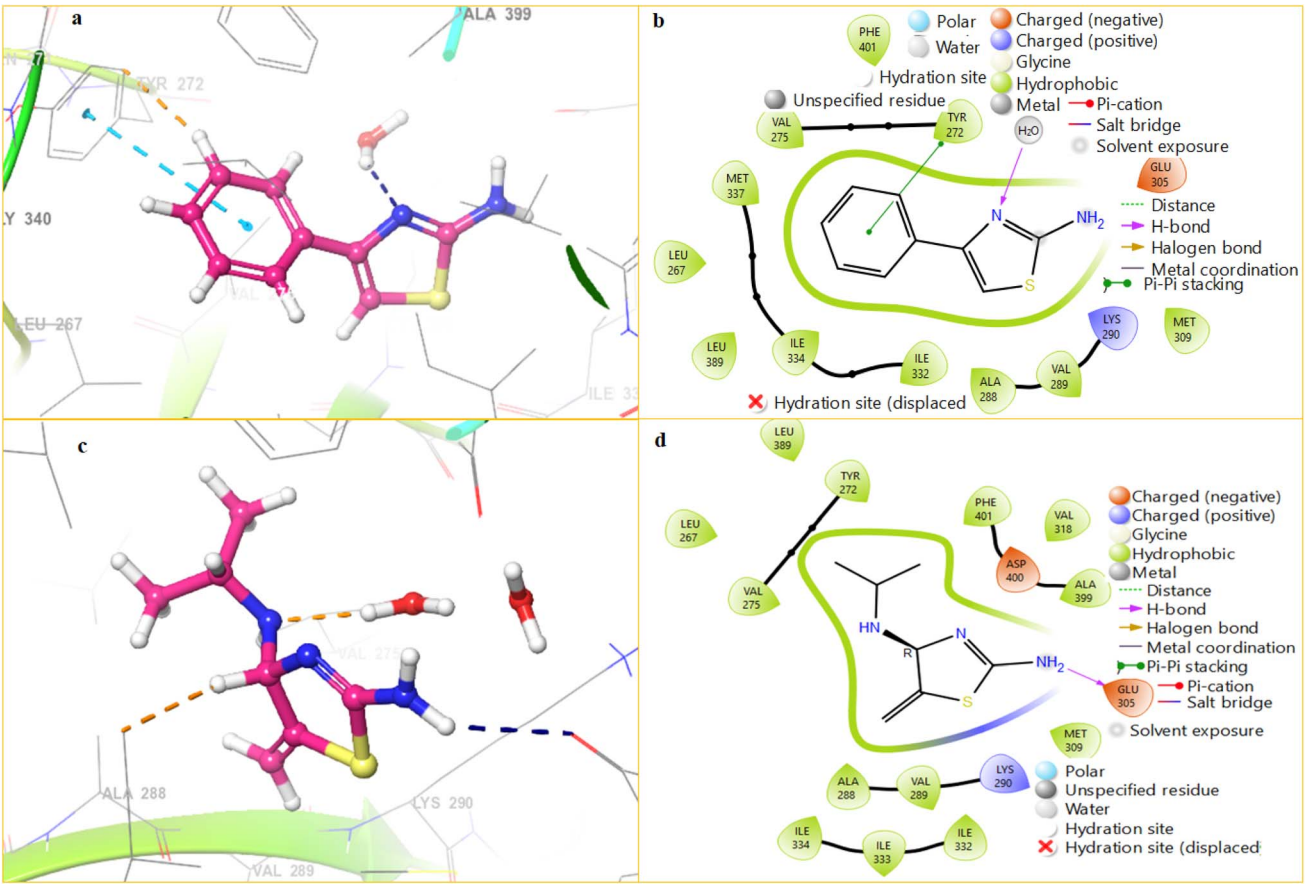

Fig. 12 (a) 3D interaction of **3b** in complex with the protein 5MO4; (b) 2D interaction of **3b** in complex with the protein 5MO4; (c) 3D interaction of **3d** in complex with the protein 5MO4; (d) 2D interaction of **3d** in complex with the protein 5MO4.

signals of a biphenyl skeleton in addition to the thaizole signals as in the case of **3b**. The ^{13}C-NMR spectral data of compound 7 also support the ^{1}H-NMR data, confirming the structure of 7. All spectral analyses of **6g** were found to be the same as that for compound **3b** with additional signals of a –OCH_2-moiety both in proton and in carbon NMR data. Similarly, the spectral data of **6h** were observed to be similar to **6g** in the presence of the propene ring and the absence of signals for the phenyl group. Spectral data (^{1}H- and ^{13}C-NMR) of **6i** were found to be in accordance with those of **3c** with additional signals for the –$COCH_2$ moiety. Similarly, spectral analysis of **6j** displayed the signals similar to that of compound **3a** with additional signals for the –$COCH_2$ moiety. All the spectral analysis of targeted compounds elucidated their structures.

3.2. Anti-tumor activity of the synthesized compounds

Targeted compounds were screened for their anti-tumor potential against chronic myeloid leukemia models K562 and U937, pro-monocytic model cell lines, by the MTT assay. The compounds **3a**, **3b**, **3c** and **6g** showed excellent inhibition against the mentioned cancer cell lines. The results are shown in Fig. 4–8 as graphical representation for both cell lines. The absorbance values obtained by the MTT assay were used to measure the cell toxicity and cell viability by measuring the activity of cellular enzymes. The cells were incubated with the MTT reagent, which was converted by cell's mitochondrial enzymes into a colored formazan product. The amount of formazan product was proportional to the number of viable cells present. To calculate the cell viability, the absorbance of the treated cultures was compared with the absorbance of untreated cultures. The percentage cytotoxicity was calculated using the following equation:

$$\%\ \text{Cytotoxicity} = 100\% - \%\ \text{cell viability}$$

Overall, the compounds showed a dose–response manner of activity; however, the compounds **3d**, **3e**, **3f**, **6j** and 7 did not show any significant toxicity against both cell lines at all concentrations, while the compound **6h** exhibited significant toxicity against both cell lines, with 82% toxicity against U937 and 84% against K562 at 10 μM concentration. Among the compounds **3b** and **3c**, the compound **3c** showed outstanding activity against U937 with 57% toxicity at 10 μM concentration. In summary, compound **6g**, **6i**, **6h**, **3b** and **3c** have potential to be promising anti-tumor compounds; however, the *in vivo* study could support the findings of the *in vitro* study.

3.2.1. Antitumor activity of targeted compounds against the cell line K562. The graph (Fig. 4) showed the dose–response curves of a number of compounds tested on the K562 cancer cell

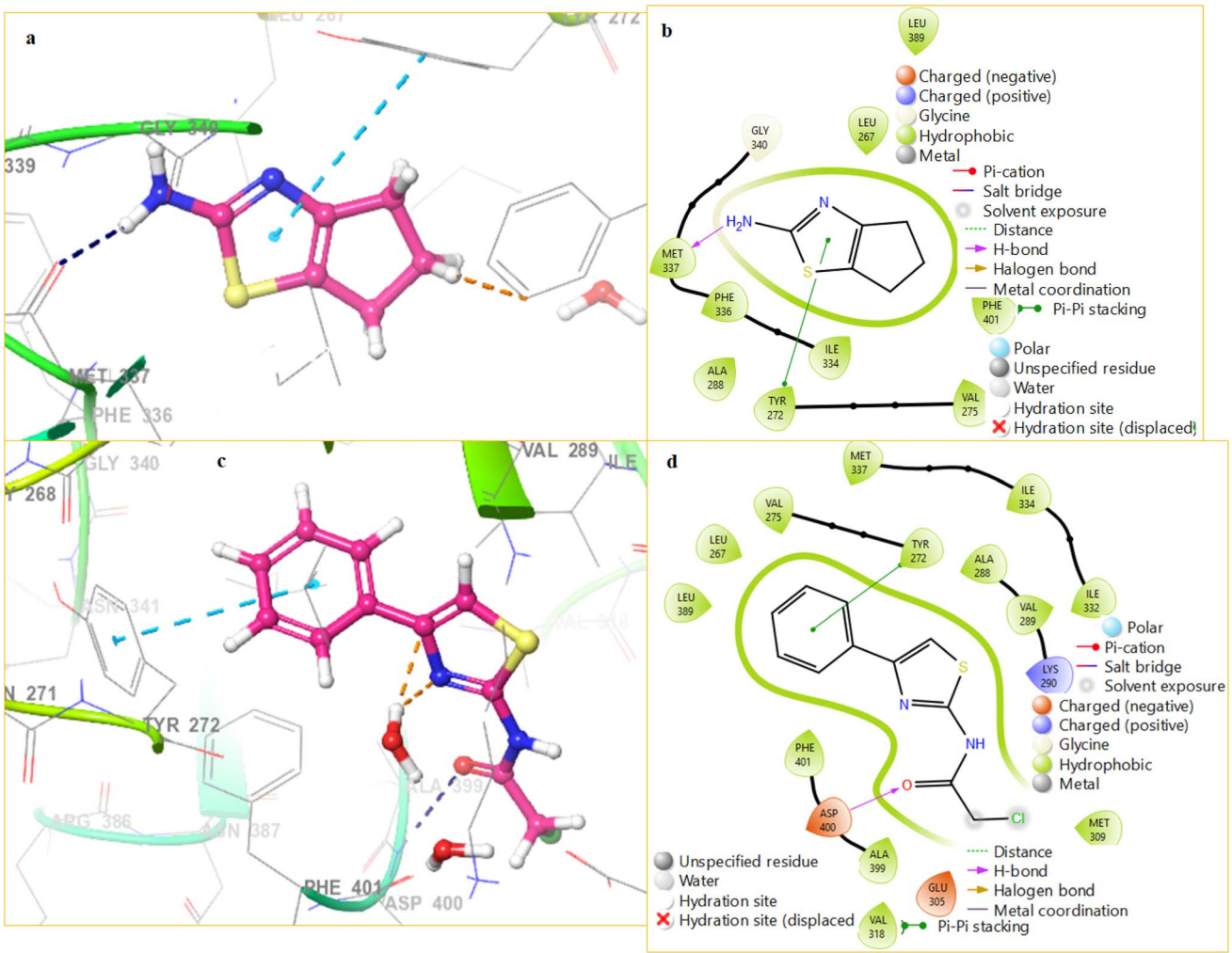

Fig. 13 (a) 3D interaction of **3e** in complex with the protein 5MO4; (b) 2D interaction of **3e** in complex with the protein 5MO4; (c) 3D interaction of **6g** in complex with the protein 5MO4; and (d) 2D interaction of **6g** in complex with the protein 5MO4.

line with molar absorbance (%) *versus* the levels of the compound (μM). The concentration in which 50 percent inhibition is observed, the IC_{50} value, is labeled next to each compound. The highest antitumor activity was observed to be exhibited by compound **3a** with the lowest value of IC_{50} of 3.523, followed by the next powerful compound **3c** (4.664), **6g** (4.938), **6h** (5.004) and **6i** (5.083) (Fig. 4). These compounds (**3c**, **6g**, **6h** and **6i**) show the good inhibitory concentration (IC_{50}) as all the compounds are under 50 value against K562 cell line. The compounds were evaluated at multiple concentrations: 0.4 μM, 0.6 μM, 0.8 μM, and 1.0 μM, as shown in Fig. 4 and 5 supported by the descriptive data reported. These data indicate that **3a** has a great potential against the K562 cell line, and it is the most effective analog compared with the others.[36] The well-defined sigmoidal curves support the standard dose–response effect, which enhances the validity of IC_{50} measurements of this screening test.

3.2.1.1. Two-way ANOVA application on anti-tumor results against the K562 cell line. The ANOVA values (Table 1 and Fig. 5) of the antitumor activity of the compounds (**3a**, **3c**, **6g**, **6h** and **6i**) against the K562 cell line have indicated extreme variability of all factors. The row factor (compounds) obtained an *F*-value of 31 988 (**P** < 0.0001), which meant that there was a lot of variation between the effects of the compounds. The interaction term and the column factor (which would be the likely concentrations) also displayed significant *F*-values of 19 297 and 4 089, respectively, with **P** < 0.0001. This is supported by the fact that the residual variance (MS = 0.5) is very low, which implies that the results are accurate and statistically significant.

3.2.1.1.1 Tukey's test. Tukey's post hoc indicated that there is a statistically significant difference between Row 1 and every other row, with the greatest mean difference occurring between Row 1 and Row 3 (78.67, $q = 385.4$). The mean differences as observed by the comparison of Row 2, Row 3 and Row 4 are smaller, and the least significant of them is the comparison of Row 2 to Row 4 (difference in means = −5.33, $q = 26.13$). Compared to Row 1, the strong statistical significance is also illustrated by high q values (>300). In general, the variability between Row 1 and the others is very high, and the differences

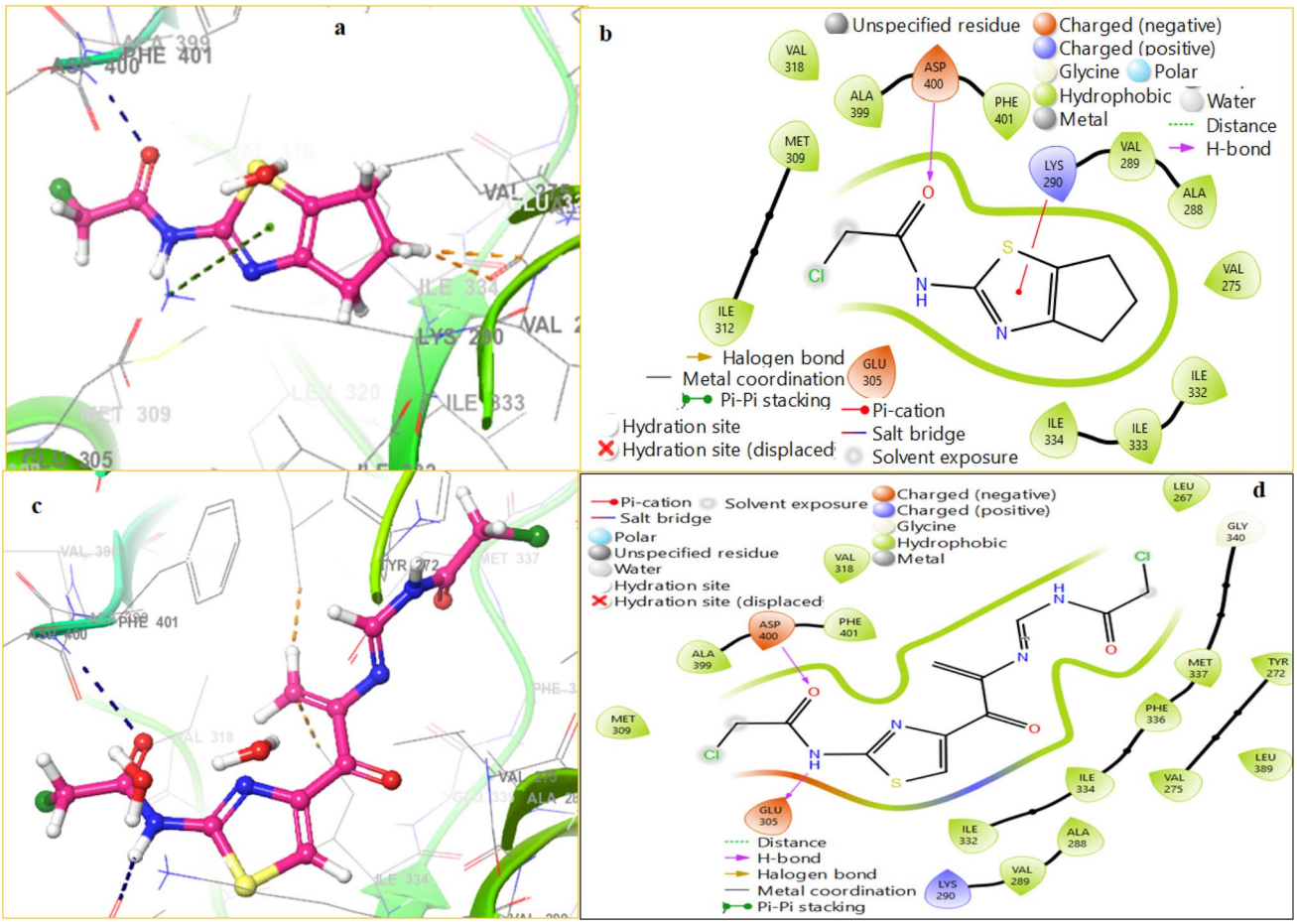

Fig. 14 (a)3D interaction of **6h** in complex with the protein 5MO4; (b) 2D interaction of **6h** in complex with the protein 5MO4; (c) 3D interaction of **6i** in complex with the protein 5MO4; and (d) 2D interaction of **6i** in complex with the protein 5MO4.

between the second, third and fourth rows are relatively not high (Table S2: SI).

3.2.1.1.2 Bonferroni's test. The multiple comparison test developed by Bonferroni proves that the differences between Row 1 and the others are highly significant, with the greatest average difference being between Row 1 and Row 3 (78.67, t = 272.5). The results of the comparison (Row 2 *vs.* 3; t = 23.67, Row 2 *vs.* 4; t = 18.48 and Row 3 *vs.* 4; t = 42.15) are also statistically different having lower t values. The standard error is very small (0.2887) and the t values are very large; hence, there is a likelihood that all the pairwise comparisons are significant even after Bonferroni's correction. These findings lead to the conclusion that Row 1 is significantly more different than the other rows, whereas the other rows are different to a smaller degree (Table S3: SI).

3.2.2. Antitumor activity data against cell line U937. The anticancer properties of the chosen compositions against the U937 cell line and IC_{50} were determined from the plot of molar absorbance (percent) against concentration (μM). The most promising compound in tests of cytotoxicity activity was **6h** with an IC_{50} value of 1.515, followed by **6i** (2.453), **3c** (3.540 2), **3b** (5.289 2), and **6g** (5.706 2) (Fig. 6). The weakest activity was observed with the compound **3a** whose IC_{50} is 150.8 μM. These compounds also show good inhibitory concentration (IC_{50}) against the U937 cell line, and the compounds were evaluated at multiple concentrations: 0.5 μM, 0.6 μM, 0.7 μM, 0.8 μM, 0.9 μM and 1.0 μM, as shown in Fig. 6 by the descriptive data. These findings indicate the fact that **6h** and **6i** were the best candidates that can be further examined in terms of anticancer activity against U937 cells.[37]

3.2.2.1. Two-way ANOVA application on anti-tumor results against the U937 cell line. The two-way ANOVA was applied on the results for compounds tested to reveal the effect on the U937 cell line showed that the differences are significantly high across the factors (Table 2 and Fig. 7). The row factor (compounds) exhibits an F-value of 43 429 (P < 0.0001), which indicates that there is a large variation in the antitumor activity among the compounds. The column factor (warmer-probable concentrations) also reveals a huge influence with an F-value of 15 201 (P < 0.0001). The interaction effect (compound × concentration) is also significant, F = 12 051, and shows different patterns of response to treatments. The reliability of the model is established by the low residual variance.

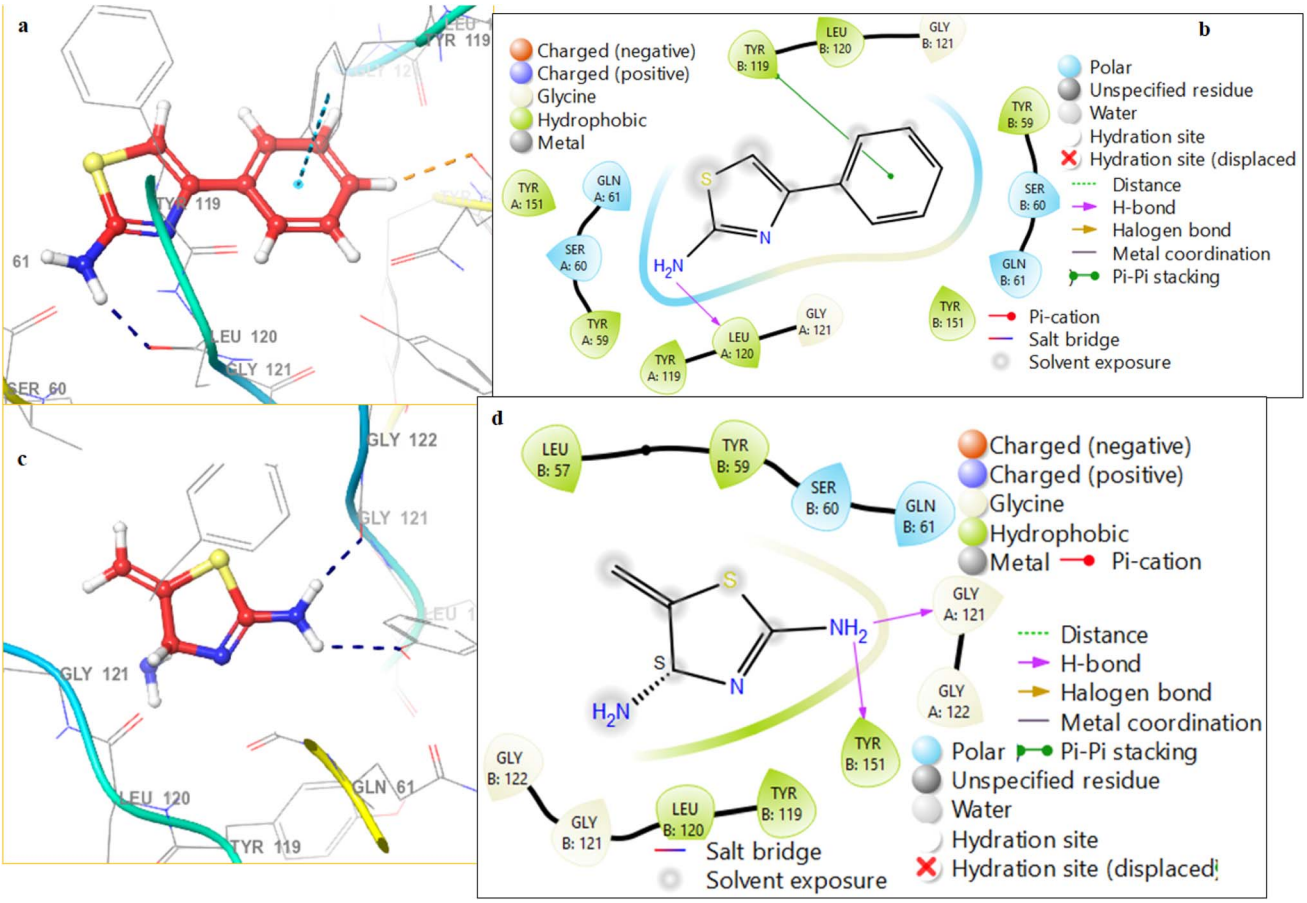

Fig. 15 (a) 3D interaction of **3b** in complex with the protein 2AZ5; (b) 2D interaction of **3b** in complex with the protein 2AZ5; (c) 3D interaction of **3f** in complex with the protein 2AZ5; and (d) 2D interaction of **3f** in complex with the protein 2AZ5.

3.2.2.1.1 Turkey's test. All the pairs of compounds give a significant difference, as observed in Tukey's test of the U937 cell line. The greatest contrast is that between Row 2 and Row 4 (mean diff. = 96.67, $q = 410.1$), Row 3 and Row 4 ($q = 376.2$) and Row 1 and Row 2 ($q = 336.6$). Even the smallest difference, Row 2 *vs.* Row 3 ($q = 33.94$), is statistically significant (because of the low standard error). These findings support the fact that all the compounds behave differently but in a significant manner in their antitumor effects in the U937 cell line, and Row 4 behaves differently, as represented in Table S4 in the SI.

3.2.2.1.2 Bonferroni's test. Bonferroni's *post-hoc* test of the U937 cell line affirms as highly true the existence of differences between compound pairs. The largest difference was calculated between Rows 2 and 4 ($t = 290.0$) and 3 and 4 ($t = 266.0$), which means that a high variation was observed in terms of antitumor effects (Table S5, SI). The differences between Row 1 and Row 2 ($t = 238.0$) and Row 1 and Row 3 ($t = 214.0$)[38] were also quite significant. The smallest contrast, Row 2 *vs.* Row 3 ($t = 24.0$) is still significant, even after Bonferroni's correction because the standard error is very small. The findings demonstrate clear and strong activity variances among the compounds that are tested (Table S5: SI).

3.2.3. Structure–activity relationship of the targeted compounds. The structure–activity relationship of targeted compounds was found to be mainly structured/influenced at the 4-position at the ring of thiazole as a site of substitution (Fig. 8), which is predominant in the anticancer activity. Adding small electron-donating alkyl groups (compound **3a** and **6g**) greatly increased the cytotoxicity, but phenyl-aromatic usage (**3b**, **6h**) increased π–π stacking interactions with key residues, which reduced activity moderate to high. Electron-withdrawing acyl (–$COCH_3$) groups of compounds **3e** and **6j** significantly lowered the activity. At position-2, unsubstituted hydrogen preferred the most favorable binding orientation, whereas a flexible linker like –CH_2–CH_2– in compound **6i** increased the flexibility at the binding pocket, leading to intensive H-bonding and halogen interactions. Amino substituents in compound **3f** that were bulky reduced the activity because of steric hindrance. Altogether, **3a**, **6g**, **6h** and **6i** proved to be the most effective ones, and the evidence of their power was based on the *in vitro* cytotoxicity and docking evidence.

3.3. Docking analysis

On the basis of electrostatic interaction between the protein and the ligand, molecular interaction also predicts the binding conformation that can be quantified. All interactions were observed to be docking scores of ligands. The docking score is shown as a negative energy value (kcal mol^{-1}). A lower energy

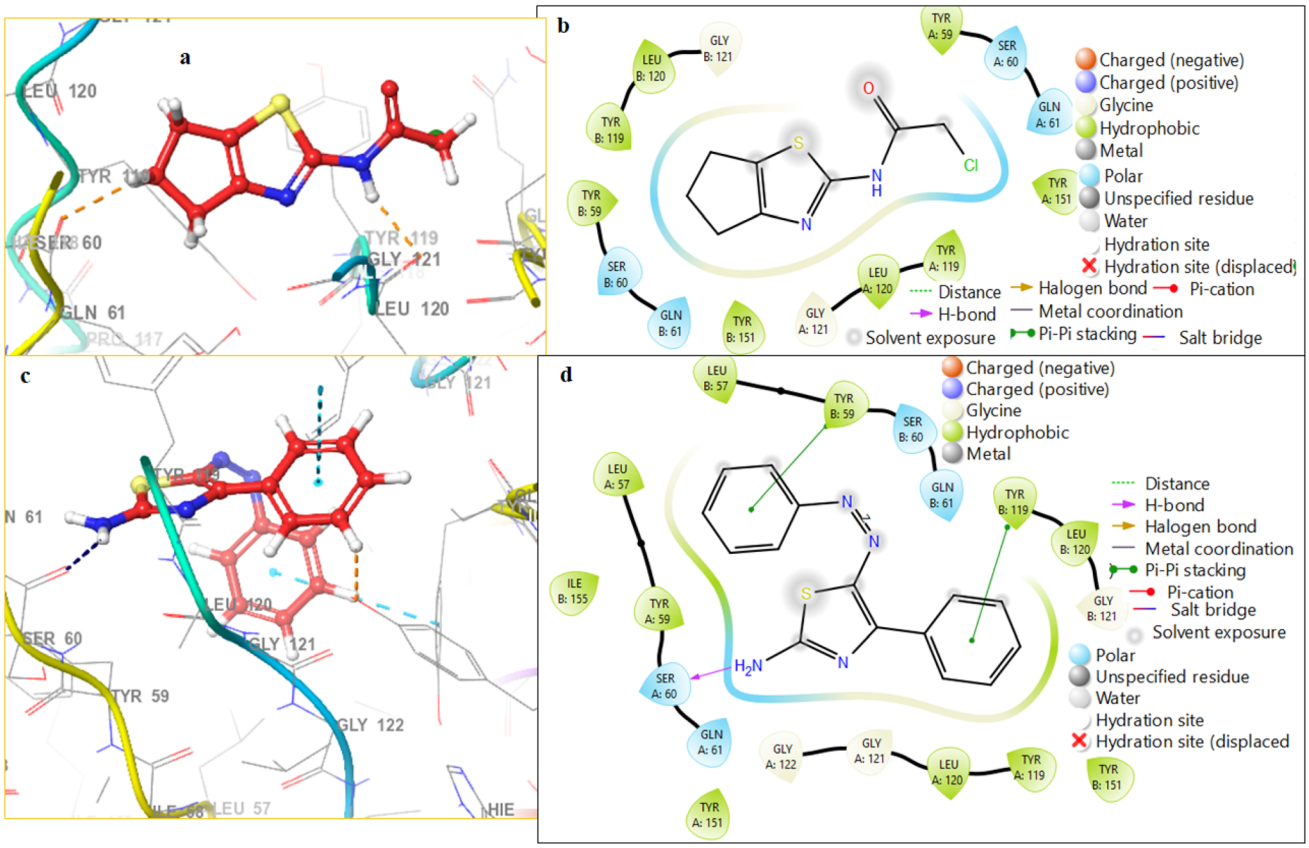

Fig. 16 (a) 3D interaction of **6h** in complex with the protein 2AZ5; (b) 2D interaction of **6h** in complex with the protein 2AZ5; (c) 3D interaction of compound **7** in complex with the protein 2AZ5; and (d) 2D interaction of compound **7** in complex with the protein 2AZ5.

value shows strong interaction between the protein and ligands.[39] Docking studies give the best binding conformation ligands and interaction of residues and ligands at enzymes active sites. 5MO4 and 2GQG proteins were selected for the chronic myeloid leukemia model K562 cell line and 2AZ5 and 5MAR proteins for the chronic myeloid leukemia model U937 cell line. Docking result showed that the good binding energy of ligands than the standard drug (5-fluorouracil) was observed, as 6 synthesized compounds out of 12 compounds showed strong interaction with 2GQG protein, 6 compounds with 5MO4 protein, 4 compounds with 2AZ5 protein and 5 compounds with 5MAR protein shown in Table 3.

3.3.1. 2GQG protein. With protein 2GQG, out of all docked compounds (Fig. S1–S5: SI and Table 3), six compounds showed a good binding score as compared to the standard drug. Compound **3e** showed 2H-bond interactions with the amino acid residue MET318 along with distances of 2.21 and 1.88 Å (Fig. 9(a and b)). Compound **3f** showed 3H-bond interactions with the amino acid residues MET318, MET318 and GLU316 with distances of 2.20, 2.21 and 1.87 Å (Fig. 9(c and d)). Compound **6h** showed 2H-bond interactions with the amino acid residue MET318 with distances of 2.28 and 1.87 Å (Fig. 10(a and b)). Compound **6i** showed 2H-bond and 2 halogen bond interactions with the amino acid residues MET318, THR315, TYR253 and GLY251 with distances of 2.09, 2.28, 3.19 and 3.09 Å (Fig. 10(c and d)). Compound **6j** showed 2H-bond interactions with the amino acid residue MET318 along with distances 2.40 and 1.86 Å (Fig. 11(a and b)). Out of the docked compounds, compound 7 show 1H-bond interaction with the amino acid residue GLU316 with a distance of 1.78 Å (Fig. 11(c and d)). In comparison with the above-mentioned compounds, 5-flourouracil standard drug shows −7.064 docking score (Fig. S6: SI).

3.3.2. Docking analysis in complex with the 5MO4 protein. From protein 5MO4 docking results of all compounds (Fig. S7–S12: SI and Table 3), 6 compounds show a good binding score as compared to the standard drug. Compound **3b** showed the Pi–Pi stacking interaction with the amino acid residue TYR272 with a distance of 4.81 Å (Fig. 12(a and b)). Compound **3d** showed 1H-bond interaction with the amino acid residue GLU305 with a distance of 2.63 Å (Fig. 12(c and d)). Compound **3e** showed 1H-bond and Pi–Pi stacking interactions with the amino acid residues MET337 and TYR272 with distances of 2.22 and 5.14 Å (Fig. 13(a and b)). Compound **6g** showed 1H-bond and Pi–Pi stacking interactions with the amino acid residues ASP400 and TYR272 with distances of 2.32 and 5.03 Å (Fig. 13(c and d)). Compound **6h** showed 1H-bond and Pi-cation interactions with the amino acid residues ASP400 and LYS290 with distances of 1.88 and 6.55 Å (Fig. 14(a and b)). Compound **6i** showed 2H-bond interactions with the amino acid residues ASP400 and GLU305 with distances of 2.40 and 2.24 Å (Fig. 14(c

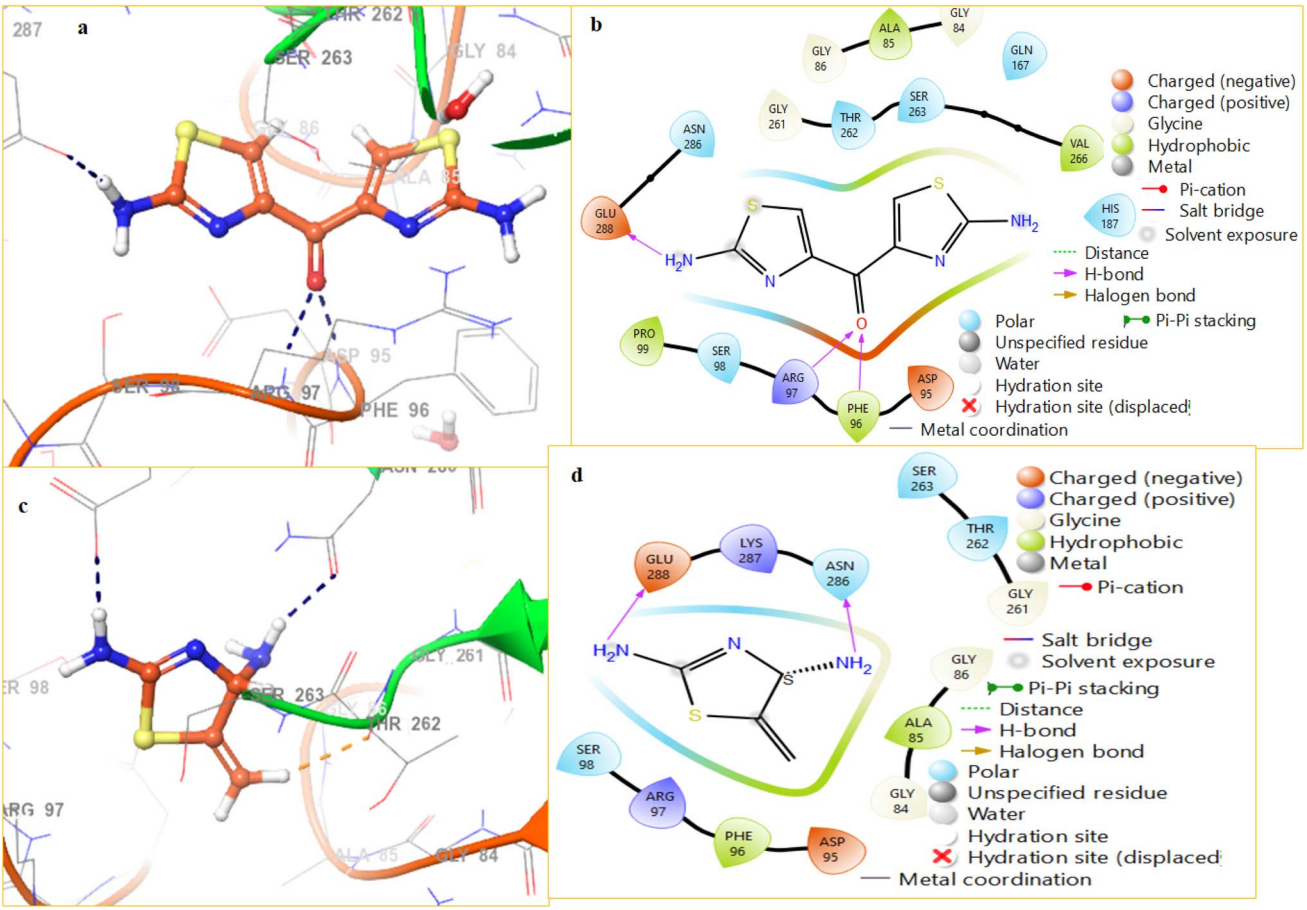

Fig. 17 (a)3D interaction of **3c** in complex with the protein 5MAR; (b) 2D interaction of **3c** in complex with the protein 5MAR; (c) 3D interaction of **3f** in complex with the protein 5MAR; and (d) 2D interaction of **3f** in complex with the protein 5MAR.

and d)). The standard drug 5-flourouracil showed a docking score of −6.329 with the 5MO4 protein as compared to those mentioned above (Fig. S12, SI).

3.3.3. 2AZ5 protein. From the protein 2AZ5, out of all the compounds, 4 compounds showed a good binding score in comparison to the standard drug (Fig. S13–S18: SI and Table 3). Compound **3b** showed 1H-bond and Pi–Pi stacking interactions with the amino acid residues LEU A: 120 and TYR B: 119 with distances of 1.85 and 5.35 (Fig. 15(a and b)). Compound **3f** showed 2H-bond interactions with the amino acid residues GLY A: 121 and TYR B: 151 with distances of 1.84 and 2.34 (Fig. 15(c and d)). Compound **6h** showed no interaction with the amino acid residue, but the docking score is higher than that of the standard drug (Fig. 16(a and b)). Compound 7 showed 1H-bond and 2Pi–Pi stacking interactions with the amino acid residues SER A:60, TYR B:59 and TYR B:119 with distances of 2.19, 5.09 and 5.49 (Fig. 16(c and d)). 5-Flourouracil standard drug showed −5.598 docking score with the 2AZ5 protein (Fig. S19: SI).

3.3.4. 5MAR protein. From the protein 5MAR, 5 compounds showed a good binding score as compared to the standard drug and other compounds (Fig. S20–S25: SI and Table 3). Compound **3c** showed 3H-bond interactions with the amino acid residues GLU288, ARG97 and PHE96 with distances of 1.83, 2.01 and 1.89 (Fig. 17a and b). Compound **3f** showed 2H-bond interactions with the amino acid residues GLU288 and ASN286 with distances of 1.68 and 2.09 (Fig. 17c and d). Compound **6h** showed 2H-bond interactions with the amino acid residues SER263 and ALA85 with distances of 2.56 and 2.28 (Fig. 18a and b). Compound **6i** showed 3H-bond and 2 halogen bond interactions with the amino acid residues ARG A:97, SER A:263, HIS A:187, ARG A:97 and TYR A:104 with distances of 2.60, 2.04, 2.31, 3.48 and 2.59 (Fig. 18c and d). Compound **6j** showed 2H-bond and 1 halogen bond interactions with the amino acid residues SER263, ALA85 and ARG97 with distances of 2.21, 1.97 and 2.64 (Fig. 19a and b). In comparison to the above-mentioned compounds, the 5-flourouracil standard drug showed −6.676 docking score with the 5MAR protein (Fig. S26: SI).

3.4. MM-GBSA analysis of complexes

After molecular docking studies, protein–ligand complexes were subjected to the Prime MM-GBSA method to calculate the binding free energy.[40] MMBSA was performed on chronic myeloid leukemia model K562 cell line proteins (5MO4 and 2GQG) and chronic myeloid leukemia model U937 cell line proteins (2AZ5 and 5MAR) with all ligands. On protein preparation, the 5MO4 protein was screened out among all other proteins because the highest binding free energy was observed

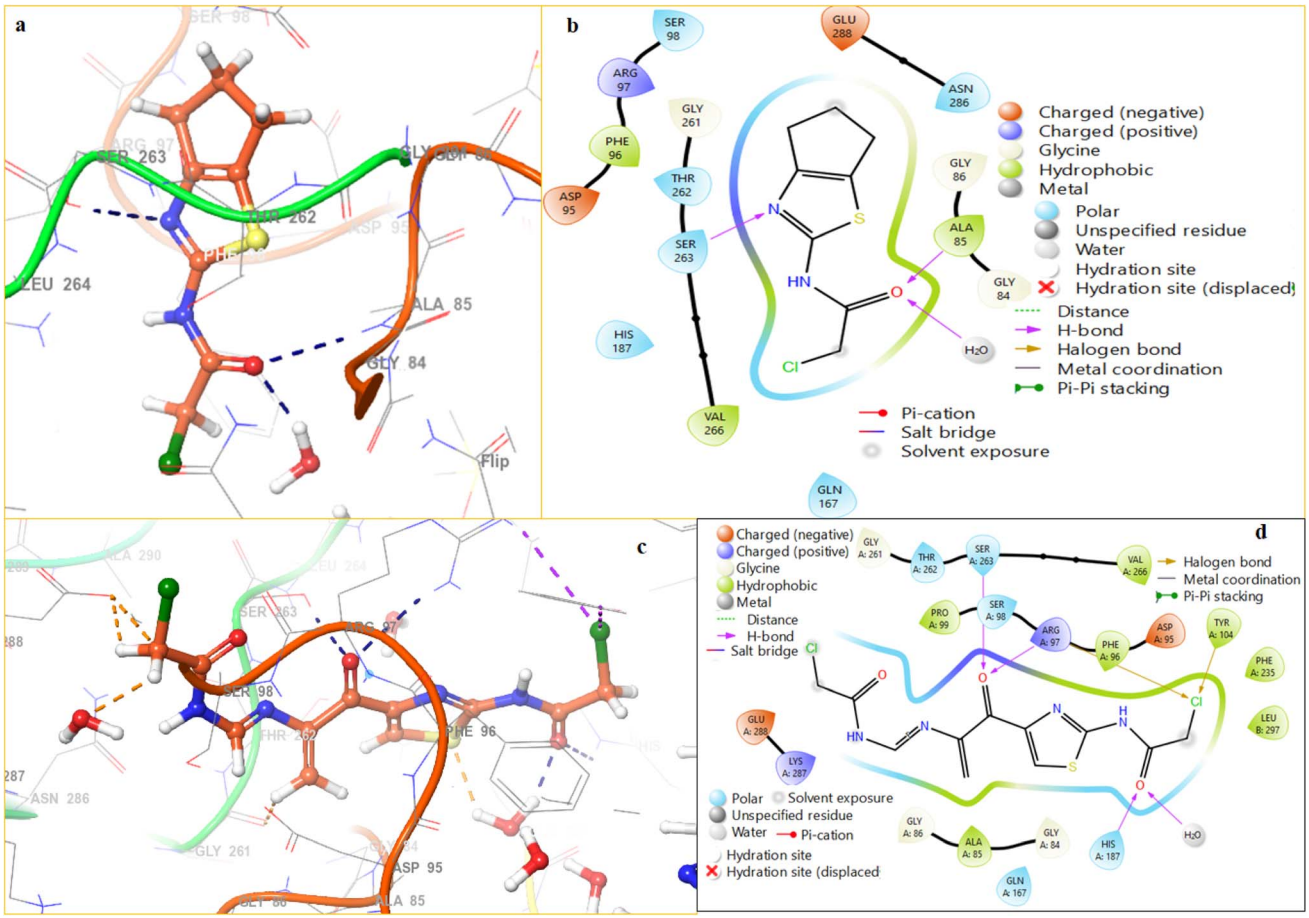

Fig. 18 (a) 3D interaction of **6h** in complex with the protein 5MAR; (b) 2D interaction of **6h** in complex with the protein 5MAR; (c) 3D interaction of **6i** in complex with the protein 5MAR; and (d) 2D interaction of **6i** in complex with the protein 5MAR.

as −53.36, respectively. The other proteins 2GQG, 2AZ5 and 5MAR showed −51.54, −36.05 and −21.92 kcal mol^{-1} negative binding free energies values. 5MO4 protein shows the negative binding free energy value of Coulomb, lipophilic and hydrogen bonding contributes positively while covalent binding free energy values contribute unfavorably (Table 4). Higher value of

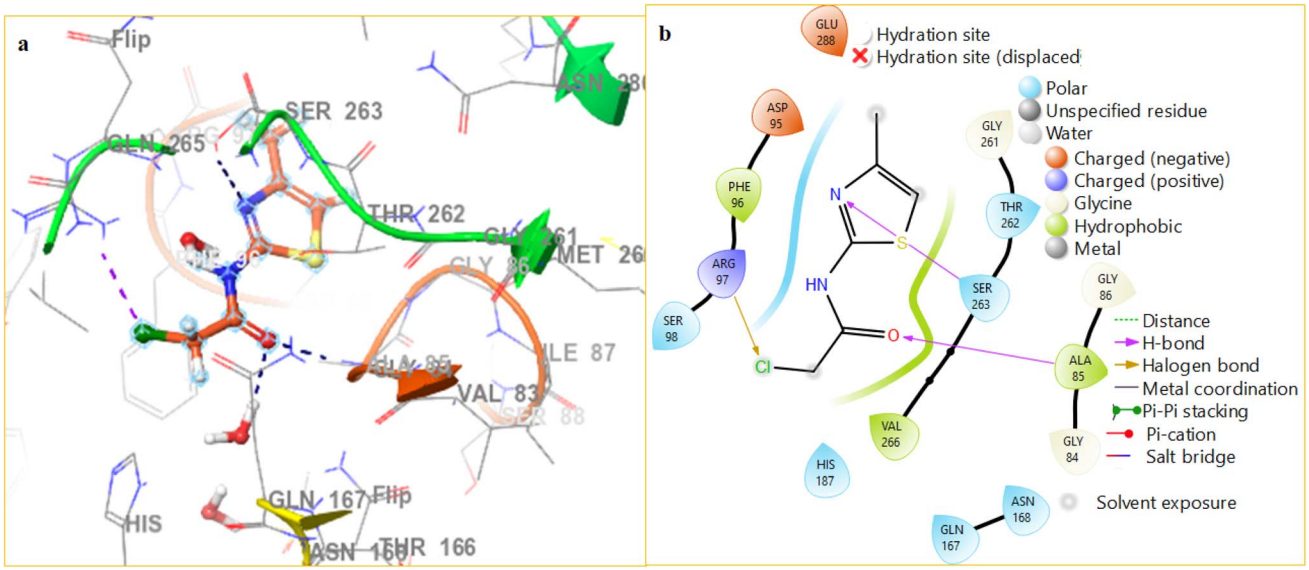

Fig. 19 (a) 3D interaction of **6j** in complex with the protein 5MAR and (b) 2D interaction of **6j** in complex with the protein 5MAR.

Table 4 Binding free energy study of protein–ligand complexes using the Prime MM-GBSA method

S. no.	Protein–ligand complex	ΔG bind (kcal mol^{-1})	ΔG bind coulomb	ΔG bind covalent	ΔG bind H-bond	ΔG bind lipophilic	ΔG bind packing
1	5MO4–**6g**	−53.36	−11.96	3.07	−1.08	−21.11	−1.79
2	5MO4–**3b**	−36.05	−7.2	3.33	−0.75	−17.53	−1.91
3	5MO4–**6i**	−44.94	−16.36	2.26	−1.35	−12.13	0
4	5MO4–**6h**	−45.11	−11.48	−0.97	−0.58	−13.53	0
5	5MO4–**3e**	−34.27	−6.4	1.12	−0.77	−14.61	−0.84
6	5MO4–**3d**	−36.19	−11.74	1.36	−1.61	−13.24	0
7	5MO4–5-fluorouracil	−23.95	−6.27	0.15	−0.55	−4.7	−0.79
8	5MO4–**3f**	−24.86	−14.56	1.32	−1.6	−4.28	0
9	5MO4–**6j**	−36.41	−10.81	−0.94	−1.01	−8.84	0
10	5MO4–7	−4.96	−0.84	14.93	−0.44	−20.87	−0.8
11	5MO4–**3c**	−25.01	−11.35	3.26	−1.46	−5.71	0
12	5MO4–**3a**	−17.65	−5.09	0.26	−0.76	−5.11	0

protein–ligand complex binding free energy suggested that the higher the affinities of protein–ligand docking along with their docking score validation will be higher.

3.5. Geometry and spectroscopic evaluation by density functional theory analysis

Density functional theory (DFT) was used for the detailed molecular structure study of the synthesized compounds and their structure–activity relationship by calculating their chemical descriptors and geometrical parameters.[41] The B3LYP functional set was used to evaluate the closely related theoretical values in comparison with the experimental values. The 2D structure of these synthesized compounds was converted into a 3D structure using PerkinElmer ChemDraw and ChemDraw 3D. Then these compounds were run on the Gaussian09W software, and DFT calculations were done for optimizing their structures[42] The DFT calculation results for ionization potential, electron affinity, energy gap, absolute softness and hardness, electronegativity, nucleophilic and electrophilic index and chemical potential values are presented in Table 5.

3.5.1. Natural bond orbital (NBO) analysis. Interpretation of the data provided by natural bond analysis (NBO) regarding the intra-molecular and intermolecular interactions, affected the molecular stabilization. Natural bond analysis gives information about electron density distribution between Lewis and non-Lewis-type donors that are bonding and anti-bonding orbitals from the second-order perturbation theory study. NBO analysis was performed using the Gaussian 09 program, which provides an understanding of the intramolecular and intermolecular interactions with their stability.[43] Stabilization energy (E^2) of compound **6h** for electron acceptor interaction is higher than the electron donor interaction. Eqn (1) illustrates the stabilization energy (E^2) calculation according to the second-order perturbation theory:

$$E^2 = q_i \frac{(F_{i,j})^2}{\varepsilon_j - \varepsilon_i} \quad (1)$$

where E^2 is the stabilization energy, $F_{(i,j)}$ is the diagonal, and ε_j and ε_i are also off diagonal of the Fock matrix element in NBOs. The structural representation and numbering of **6h** (2-chloro-*N*-(5,6-dihydro-4*H* cyclopenta[*d*]thiazol-2-ylacetamide)) and **6i** (*N*,*N*′-(4,4′-carbonylbis(thiazole-4,2-diyl))bis-(2-chloroacetamide)) compounds are represented in Fig. S27 (SI).

Natural Bond Orbital (NBOs) analysis for the lead compound **6h** (2-chloro-*N*-(5, 6-dihydro-4*H* cyclopenta[*d*]thiazol-2-yl) acetamide) mentioned in Table shows the highest transition observed as π (C2–N3) to π* (C4–C5) with 19.16 kcal mol^{-1}

Table 5 Chemical descriptors of compounds **6h** and **6i** calculated by the B3LYP 6-311G basis set of DFT

Parameters	**6h** Compound	**6i** Compound
E_{HOMO}	−0.27911 (−7.5949 hartree)	−0.27423 (−7.4622 hartree)
E_{LUMO}	−0.04535 (−1.2340 hartree)	−0.07854 (−2.1372 hartree)
Ionization potential (I)	7.5949	7.4622
Electron affinity (A)	1.2340	2.1372
Energy gap (ΔE)	6.3609	5.325
Absolute hardness (η)	3.1804	2.6625
Absolute softness (σ)	0.3144	0.3755
Electronegativity (χ)	4.4144	4.7997
Chemical potential (CP)	−4.4144	−4.7997
Electrophilicity index (ω)	3.0635	4.3262
Nucleophilicity index (N)	0.3264	0.2311
Additional electronic charges (ΔN_{max})	1.3880	1.8027
Global softness (S)	0.1572	0.1877

Table 6 Second-order perturbation theory analysis of Fock matrix in NBO basis for the compound **6h**[a]

S. no.	Donor (i)	Type	Acceptor (j)	Type	E^2 (kcal mol^{-1})	$E_i - E_j$	$F_{i,j}$
1	S1–C2	Σ	C4–C8	σ*	1.47	1.12	0.036
2	S1–C2	Σ	C5–C6	σ*	7.11	1.12	0.08
3	S1–C2	Σ	N9–H20	σ*	2.91	1.05	0.05
4	S1–C5	Σ	C2–N9	σ*	4.11	1.22	0.064
5	S1–C5	Σ	N3–C4	σ*	0.74	1.22	0.027
6	S1–C5	Σ	C4–C5	σ*	1.1	1.37	0.035
7	S1–C5	Σ	C4–C8	σ*	4.25	1.19	0.064
8	S1–C5	Σ	C5–C6	σ*	0.86	1.19	0.029
9	S1–C5	Σ	C6–C7	σ*	0.68	1.15	0.025
10	C2–N3	Σ	C2–N9	σ*	2.75	1.32	0.054
11	C2–N3	Σ	N3–C4	σ*	0.93	1.32	0.031
12	C2–N3	Σ	C4–C8	σ*	6.17	1.29	0.08
13	C2–N3	Σ	N9–C10	σ*	3.45	1.28	0.06
14	C2–N3	Π	C2–N3	π*	0.9	0.3	0.016
15	**C2–N3**	**Π**	**C4–C5**	**π***	**19.16**	**0.36**	**0.078**
16	C2–N9	Σ	C2–N3	σ*	2.16	1.4	0.049
17	C2–N9	Σ	N3–C4	σ*	2.35	1.34	0.05
18	C2–N9	Σ	N9–C10	σ*	2.09	1.3	0.047
19	C2–N9	Σ	N9–H20	σ*	0.6	1.24	0.024
20	C2–N9	Σ	C10–O11	σ*	1.12	1.4	0.035
21	N3–C4	Σ	C2–N3	σ*	0.6	1.3	0.025
22	N3–C4	Σ	C2–N9	σ*	7.63	1.24	0.087
23	N3–C4	Σ	C4–C5	σ*	2.18	1.39	0.049
24	N3–C4	σ	C4–C8	σ*	1.32	1.21	0.036
25	N3–C4	σ	C5–C6	σ*	2.43	1.21	0.048
26	C4–C5	σ	S1–C5	σ*	0.88	0.99	0.026
27	C4–C5	σ	C2–N9	σ*	1.51	1.19	0.038
28	C4–C5	σ	N3–C4	σ*	1.91	1.19	0.043
29	C4–C5	σ	C4–C8	σ*	3.08	1.16	0.053
30	C4–C5	σ	C5–C6	σ*	4.24	1.16	0.063
31	C4–C5	σ	C8–H18	σ*	0.53	1.21	0.023
32	**C4–C5**	**π**	**C2–N3**	**π***	**10.6**	**0.26**	**0.05**
33	C4–C5	π	C6–H14	σ*	3.65	0.74	0.048
34	C4–C5	π	C6–H14	σ*	3.09	0.65	0.041
35	C4–C5	π	C8–H18	σ*	2.65	0.75	0.041
36	C4–C5	π	C8–H19	σ*	2.79	0.73	0.042
37	C4–C8	σ	S1–C5	σ*	5.24	0.86	0.06
38	C4–C8	σ	C2–N3	σ*	2.12	1.12	0.044
39	C4–C8	σ	N3–C4	σ*	1.41	1.06	0.035
40	C4–C8	σ	C4–C5	σ*	3.56	1.21	0.059
41	C4–C8	σ	C6–C7	σ*	0.56	0.99	0.021
42	**C4–C8**	**σ**	**C7–C8**	**σ***	**0.51**	**0.96**	**0.02**
43	C4–C8	σ	C7–H17	σ*	0.66	1.02	0.023
44	C4–C8	σ	C8–H18	σ*	1.08	1.08	0.031
45	C4–C8	σ	C8–H19	σ*	0.86	1.06	0.027
46	C5–C6	σ	S1–C5	σ*	0.57	0.89	0.02
47	C5–C6	σ	N3–C4	σ*	4.56	1.09	0.063
48	C5–C6	σ	C4–C5	σ*	4.85	1.24	0.07
49	C5–C6	σ	C6–C7	σ*	0.82	1.03	0.026
50	C5–C6	σ	C6–H14	σ*	1.02	1.1	0.03
51	C5–C6	σ	C6–H15	σ*	0.62	1.01	0.022
52	C5–C6	σ	C7–C8	σ*	0.53	0.99	0.02
53	C5–C6	σ	C7–H17	σ*	1.36	1.05	0.034
54	C6–C7	σ	S1–C5	σ*	9.1	0.85	0.078
55	C6–C7	σ	N3–C4	σ*	0.52	1.05	0.021
56	C6–C7	σ	C4–C8	σ*	0.54	1.02	0.021
57	C6–C7	σ	C5–C6	σ*	1.8	1.02	0.038
58	C6–C7	σ	C6–H14	σ*	0.98	1.06	0.029
59	C6–C7	σ	C6–H15	σ*	0.54	0.97	0.02
60	C6–H14	σ	C4–C5	σ*	1.15	1.11	0.032
61	C6–H14	σ	C4–C5	π*	3.52	0.54	0.042
62	C6–H14	σ	C5–C6	σ*	0.54	0.93	0.02
63	C6–H14	σ	C7–C8	σ*	0.88	0.86	0.025
64	C6–H14	σ	C7–H16	σ*	0.89	0.85	0.025
65	C6–H14	σ	C7–H17	σ*	1.01	0.92	0.027
66	C6–H15	σ	C4–C5	σ*	1.97	1.09	0.041
67	C6–H15	σ	C4–C5	π*	2.93	0.52	0.038
68	C6–H15	σ	C7–C8	σ*	1.5	0.84	0.032
69	C6–H15	σ	C7–H16	σ*	1.22	0.83	0.029
70	C7–C8	σ	S1–C5	σ*	1.09	0.81	0.027
71	C7–C8	σ	N3–C4	σ*	7.08	1.02	0.076
72	C7–C8	σ	C4–C8	σ*	0.93	0.99	0.027
73	C7–C8	σ	C5–C6	σ*	0.54	0.99	0.021
74	C7–C8	σ	C6–H15	σ*	0.66	0.94	0.022
75	C7–C8	σ	C8–H18	σ*	0.76	1.04	0.025
76	C7–C8	σ	C8–H19	σ*	0.67	1.01	0.023
77	C7–H16	σ	C4–C8	σ*	0.52	0.88	0.019
78	C7–H16	σ	C5–C6	σ*	0.58	0.88	0.02
79	C7–H16	σ	C6–H14	σ*	1.29	0.92	0.031
80	C7–H16	σ	C6–H15	σ*	1.52	0.83	0.032
81	C7–H16	σ	C8–H18	σ*	1.15	0.93	0.029
82	C7–H16	σ	C8–H19	σ*	1.37	0.9	0.031
83	C7–H17	σ	C4–C8	σ*	0.87	0.9	0.025
84	C7–H17	σ	C5–C6	σ*	1.16	0.91	0.029
85	C7–H17	σ	C6–H14	σ*	1.2	0.95	0.03
86	C7–H17	σ	C8–H18	σ*	0.89	0.95	0.026
87	C8–H18	σ	C4–C5	σ*	1.52	1.1	0.037
88	C8–H18	σ	C4–C5	π*	2.47	0.54	0.035
89	C8–H18	σ	C6–C7	σ*	0.82	0.89	0.024
90	C8–H18	σ	C7–H16	σ*	0.55	0.85	0.019
91	C8–H18	σ	C7–H17	σ*	0.84	0.92	0.025
92	C8–H19	σ	C4–C5	σ*	1.15	1.08	0.032
93	C8–H19	σ	C4–C5	π*	5.11	0.52	0.049
94	C8–H19	σ	C6–C7	σ*	1.11	0.87	0.028
95	C8–H19	σ	C7–H16	σ*	1.28	0.83	0.029
96	N9–C10	σ	C2–N3	σ*	1.94	1.37	0.046
97	N9–C10	σ	C2–N9	σ*	2.6	1.3	0.052
98	N9–C10	σ	C12–Cl13	σ*	0.84	0.9	0.025
99	N9–H20	σ	S1–C2	σ*	6.65	0.79	0.066
100	N9–H20	σ	C2–N3	σ*	0.94	1.15	0.03
101	N9–H20	σ	C2–N9	σ*	0.66	1.09	0.024
102	N9–H20	σ	C10–O11	σ*	1.65	1.16	0.039
103	N9–H20	σ	C10–C12	σ*	5.37	0.91	0.063
104	C10–O11	σ	C2–N9	σ*	3.04	1.48	0.06
105	C10–O11	σ	N9–C10	σ*	0.94	1.44	0.033
106	C10–O11	σ	C10–C12	σ*	0.66	1.3	0.027
107	C10–O11	π	C10–O11	π*	1.06	0.35	0.018
108	C10–O11	π	C12–H21	σ*	0.74	0.77	0.021
109	C10–O11	π	C12–H22	σ*	1.58	0.8	0.032
110	C10–C12	σ	N9–H20	σ*	2.07	0.99	0.04
111	**C10–C12**	**σ**	**C10–O11**	**σ***	**0.51**	**1.15**	**0.022**
112	C12–Cl13	σ	N9–C10	σ*	2.74	1.03	0.048
113	C12–Cl13	σ	C10–O11	σ*	0.59	1.14	0.023
114	C12–H21	σ	C10–O11	σ*	2.56	1.07	0.047
115	C12–H21	σ	C10–O11	π*	1.59	0.54	0.028
116	C12–H21	σ	C12–Cl13	σ*	0.79	0.6	0.02
117	C12–H22	σ	C10–O11	π*	4.2	0.55	0.046
118	C12–H22	σ	C12–Cl13	σ*	0.91	0.61	0.021
119	S1	LP1	C2–N3	σ*	3.14	1.15	0.054
120	S1	LP1	C4–C5	σ*	2.41	1.23	0.049
121	S1	LP1	C5–C6	σ*	0.8	1.06	0.026
122	S1	LP1	C12–Cl13	σ*	0.75	0.68	0.02
123	**S1**	**LP2**	**C2–N3**	**π***	**31.07**	**0.24**	**0.078**
124	S1	LP2	C4–C5	π*	25.32	0.29	0.078
125	N3	LP1	S1–C2	σ*	17.31	0.5	0.084

Table 6 (*Contd.*)

S. no.	Donor (i)	Type	Acceptor (j)	Type	E^2 (kcal mol^{-1})	$E_i - E_j$	$F_{i,j}$
126	N3	LP1	C2–N9	σ*	3.22	0.8	0.046
127	N3	LP1	C4–C5	σ*	6.29	0.95	0.07
128	N3	LP1	C4–C8	σ*	0.79	0.77	0.023
129	N9	LP1	S1–C2	σ*	0.99	0.43	0.02
130	**N9**	**LP1**	**C2–N3**	**π***	**49.68**	**0.25**	**0.102**
131	**N9**	**LP1**	**C10–O11**	**π***	**56.91**	**0.26**	**0.112**
132	O11	LP1	N9–C10	σ*	1.51	1.1	0.037
133	O11	LP1	C10–C12	σ*	1.66	0.95	0.036
134	**O11**	**LP2**	**C2–N9**	**σ***	**0.61**	**0.7**	**0.019**
135	O11	LP2	N9–C10	σ*	22.05	0.66	0.109
136	O11	LP2	C10–C12	σ*	22.14	0.52	0.096
137	Cl13	LP2	C12–H21	σ*	3.02	0.7	0.041
138	Cl13	LP2	C12–H22	σ*	3.55	0.73	0.046
139	Cl13	LP3	C10–C12	σ*	4.91	0.57	0.048
140	Cl13	LP3	C12–H22	σ*	1.26	0.71	0.027
141	Cl13	LP3	C12–H22	σ*	0.62	0.74	0.019
142	C2–N3	π*	C4–C5	π*	41.07	0.06	0.07
143	C2–N3	π*	C10–O11	π*	1.02	0.01	0.005
144	C4–C5	π*	C6–H14	σ*	1.05	0.43	0.047
145	C4–C5	π*	C6–H15	σ*	0.79	0.34	0.036
146	C4–C5	π*	C8–H18	σ*	0.85	0.44	0.043
147	C4–C5	π*	C8–H19	σ*	1.06	0.42	0.046
148	C10–O11	π*	C12–Cl13	σ*	1.24	0.06	0.021
149	C10–O11	π*	C12–H22	σ*	1.06	0.45	0.053

[a] *$E^{(2)}$ means the energy of the hyper conjugative interaction (stabilization energy in kcal mol^{-1}). *Energy difference $E_{(j)} - E_{(i)}$ between the donor and the acceptor i and j NBO orbitals. *$F_{(i,j)}$ is the Fock matrix element between the i and j NBO orbitals.

stabilization energy. Its highest energy value shows high stabilization and the strongest interaction between the electron donor and acceptor. The second highest transition is π (C4–C5) to π* (C2–N3) with a high stabilization energy of 10.6 kcal mol^{-1}. The σ (C4–C8)-to-σ* (C7–C8) transition shows the smallest stabilization energy as 0.51 kcal mol^{-1}. Its lowest stabilization energy shows weak interactions between the electron donor (σ) and acceptor (σ*). Other σ (C10–C12)-to-σ* (C10–C11) transitions also exhibit the lowest stabilization energy of 0.51 kcal mol^{-1}. Similarly, LP1 (N9) to π* (C10–C11), LP1 (N9) to π* (C2–N3) and LP2 (S1) to π* (C2–N3) transitions were observed at the highest stabilization energies of 56.91 kcal mol^{-1}, 49.68 kcal mol^{-1} and 31.07 kcal mol^{-1}, while the LP2 (O11)-to-σ* (C2–N9) transition produces the lowest stabilization energy of 0.61 kcal mol^{-1} that shows the low interaction energy (Table 6).

NBO analysis of the compound **6i** (*N*,*N*′-(4,4′-carbonylbis(-thiazole-4,2-diyl)))-bis-(2-chloroacetamide) mentioned in Table 7 shows the highest transition observed as π (C10–N11) to π* (C7–C8) with 19.53 kcal mol^{-1} stabilization energy. This compound has the highest energy value, which shows high stabilization and the strongest interaction between the electron donor (π) and the acceptor (π*). The second highest transition is π (C7–C8) to π* (C6–O12) with a high stabilization energy of 17.91 kcal mol^{-1}, while σ (C16–Cl17)-to-σ* (C14–O15) transition shows the smallest stabilization energy of 0.51 kcal mol^{-1}. Its lowest stabilization energy shows weak interactions between the electron donor and acceptor. Similarly, LP1 (N13)-to-π* (N1–C2) and LP1 (N18)-to-π* (C19–O20) transitions were observed at the highest stabilization energy of 55.92 kcal mol^{-1} and 53.66 kcal mol^{-1}, while LP3 (Cl17)-to-σ* (C16–H27) transition produced the lowest stabilization energy of 0.53 kcal mol^{-1} that shows the low interaction energy (Table 7).

3.5.2. Mulliken's population and natural population analysis. Mulliken's population analysis (MPA) and natural population analysis (NPA) of compounds **6h** and **6i** were determined by the B3LYP method with the 6-311G basis set for the detailed study of reactive sites of the biologically active compounds, as shown in Table S1 (SI). The Mulliken population analysis can be used to describe the phenomena of transformation of atomic charge in reaction, electronegativity equalization and electrostatic potential of system.[44] In MPA and NPA analysis all hydrogen atoms show positive charges and all oxygen and nitrogen show negative charges. If hydrogen is attached with a negatively charged carbon atom, then it shows the charge transfer from hydrogen to carbon atom. Similarly, in chemical bonding, nitrogen and oxygen atoms show the same behavior.[45] Our goal is to assess the reactivity of the depicted charges using the quantum chemical technique and to provide a detailed description of the electron distribution of these compounds. Charge analysis of compound **6h** indicates that N9–H20–O11 is involved in strong intramolecular hydrogen bonding as compared to N3, while C2, C4 and C5 are positively charged and give the best pathway to other chemical moieties for attachment. All hydrogen atoms transform their charges to carbon atoms, and S1 and Cl13 atoms show electron-withdrawing behavior. The graphical representation of compound **6h** with Mulliken's population analysis (MPA) and natural population analysis (NPA) is shown in Fig. 20.

The charge analysis of compound **6i** indicates that N13–H25–O15 and N18–H28–O20 are involved in strong intramolecular hydrogen bonding as compared to other negatively charged nitrogen N1 and N11. C2, C5, C7 and C10 are also positively charged, providing a path for new moieties to attach. O12, O15 and O20 are the strong carbonyl acceptors and provide an ideal site for intramolecular hydrogen bonding. The graphical representation of compound **6i** with Mulliken's population analysis (MPA) and natural population analysis (NPA) is shown in Fig. 21.

3.5.3. Frontier molecular orbital (FMO) analysis. Frontier molecular orbital (FMO) is an important parameter in DFT that is used to check the chemical strength of compounds. Quantum orbitals as the lowest unoccupied molecular orbital (LUMO) and highest occupied molecular orbitals (HOMO) give us qualitative information about HOMO that can donate its electron to LUMO for the measurement of chemically reactive descriptors.[46] Energy gap can also be calculated by HOMO–LUMO and provide us information about stability and chemical reactivity of compounds. Contour and energy diagram of frontier molecular orbitals of both compounds along with energy gap is shown in Fig. 22 and 23.

The above-mentioned HOMO–LUMO energy values of compounds **6h** and **6i** are calculated at the B3LYP 6-311G basis set of DFT. Frontier molecular orbitals (FMOs) can also be used

Table 7 Second-order perturbation theory analysis of Fock matrix in NBO basis for the compound **6i**[a]

S. no.	Donor (i)	Type	Acceptor (j)	Type	E^2 (kcal mol^{-1})	$E_i - E_j$	$F_{i,j}$
1	N1–C2	σ	N1–C5	σ*	0.73	1.28	0.027
2	N1–C2	σ	C2–N13	σ*	2.63	1.33	0.053
3	N1–C2	σ	C5–C6	σ*	3.27	1.31	0.059
4	N1–C2	σ	N13–H25	σ*	1.39	1.31	0.038
5	N1–C2	π	N1–C2	π*	1.31	0.31	0.019
6	N1–C2	π	C4–C5	π*	15.52	0.33	0.067
7	N1–C5	σ	N1–C2	σ*	0.52	1.27	0.023
8	N1–C5	σ	C2–N13	σ*	8.26	1.19	0.089
9	N1–C5	σ	C4–C5	σ*	1.33	1.26	0.037
10	N1–C5	σ	C4–H23	σ*	2.48	1.18	0.049
11	N1–C5	σ	C5–C6	σ*	0.92	1.17	0.03
12	N1–C5	σ	C6–C7	σ*	1.1	1.17	0.032
13	N1–C5	σ	C6–O12	π*	0.74	0.75	0.022
14	C2–S3	σ	C4–H23	σ*	3.34	1.15	0.055
15	C2–S3	σ	C5–C6	σ*	0.81	1.13	0.027
16	C2–S3	σ	N13–C14	σ*	4.65	1.12	0.065
17	C2–S3	σ	N13–H25	σ*	0.74	1.13	0.026
18	C2–N13	σ	N1–C2	σ*	2.78	1.39	0.056
19	C2–N13	σ	N1–C5	σ*	2.79	1.26	0.053
20	C2–N13	σ	N13–C14	σ*	1.42	1.28	0.039
21	C2–N13	σ	N13–H25	σ*	0.84	1.29	0.029
22	C2–N13	σ	C14–O15	σ*	1.1	1.42	0.035
23	S3–C4	σ	N1–C2	σ*	0.68	1.21	0.026
24	S3–C4	σ	N1–C5	σ*	1.53	1.08	0.036
25	S3–C4	σ	C2–N13	σ*	4.28	1.13	0.063
26	S3–C4	σ	C5–C6	σ*	4.98	1.12	0.067
27	C4–C5	σ	N1–C5	σ*	0.79	1.12	0.027
28	C4–C5	σ	C2–N13	σ*	1.2	1.18	0.034
29	C4–C5	σ	C4–H23	σ*	1.55	1.17	0.038
30	C4–C5	σ	C5–C6	σ*	2.57	1.16	0.049
31	C4–C5	σ	C6–O12	σ*	1.2	1.26	0.035
32	C4–C5	π	N1–C2	π*	8.86	0.26	0.046
33	C4–C5	π	C4–C5	π*	0.53	0.28	0.011
34	C4–C5	π	C6–C7	σ*	1.19	0.71	0.026
35	C4–C5	π	C6–O12	σ*	1.2	0.81	0.029
36	C4–C5	π	C6–O12	π*	12.07	0.29	0.053
37	C4–H23	σ	N1–C5	σ*	3.59	0.95	0.052
38	C4–H23	σ	C2–S3	σ*	0.52	0.72	0.018
39	C4–H23	σ	S3–C4	σ*	0.69	0.73	0.02
40	C4–H23	σ	C4–C5	σ*	1.47	1.07	0.035
41	C5–C6	σ	N1–C2	σ*	1.94	1.19	0.043
42	C5–C6	σ	N1–C5	σ*	0.8	1.06	0.026
43	C5–C6	σ	S3–C4	σ*	2.53	0.84	0.041
44	C5–C6	σ	C4–C5	σ*	3.33	1.18	0.056
45	C5–C6	σ	C6–C7	σ*	1.34	1.1	0.035
46	C5–C6	σ	C6–O12	σ*	1.26	1.2	0.035
47	C5–C6	σ	C7–C8	σ*	3	1.17	0.053
48	C6–C7	σ	N1–C5	σ*	2.07	1.07	0.042
49	C6–C7	σ	C4–C5	π*	0.75	0.68	0.022
50	C6–C7	σ	C5–C6	σ*	1.49	1.1	0.037
51	C6–C7	σ	C6–O12	σ*	1.06	1.21	0.032
52	C6–C7	σ	C7–C8	σ*	3.19	1.17	0.055
53	C6–C7	σ	C7–N11	σ*	1.53	1.13	0.037
54	C6–C7	σ	C8–S9	σ*	2.09	0.86	0.038
55	C6–C7	σ	C10–N11	σ*	3.11	1.18	0.054
56	C6–O12	σ	C4–C5	σ*	1.36	1.55	0.041
57	C6–O12	σ	C5–C6	σ*	1.94	1.46	0.048
58	C6–O12	σ	C6–C7	σ*	1.78	1.47	0.046
59	C6–O12	σ	C7–N11	σ*	1.35	1.49	0.04
60	C6–O12	π	N1–C5	σ*	1.13	0.75	0.026
61	C6–O12	π	C4–C5	σ*	0.72	0.87	0.022
62	C6–O12	π	C4–C5	π*	4.8	0.36	0.04
63	C6–O12	π	C7–C8	π*	6.82	0.34	0.047
64	C7–C8	σ	C6–C6	σ*	1.51	1.16	0.038
65	C7–C8	σ	C6–C7	σ*	3.33	1.16	0.056
66	C7–C8	σ	C7–N11	σ*	1.43	1.19	0.037
67	C7–C8	σ	C8–H24	σ*	1.93	1.2	0.043
68	C7–C8	σ	C10–N18	σ*	1.39	1.12	0.035
69	**C7–C8**	**π**	**C6–O12**	**π***	**17.91**	**0.29**	**0.065**
70	C7–C8	π	C7–C8	π*	0.76	0.28	0.013
71	C7–C8	π	C10–N11	π*	12.84	0.25	0.054
72	C7–N11	σ	C6–C7	σ*	1.13	1.25	0.034
73	C7–N11	σ	C6–O12	σ*	1.32	1.36	0.038
74	C7–N11	σ	C7–C8	σ*	1.87	1.32	0.044
75	C7–N11	σ	C8–H24	σ*	1.82	1.29	0.043
76	C7–N11	σ	C10–N11	σ*	1.27	1.32	0.037
77	C7–N11	σ	C10–N18	σ*	8.27	1.21	0.09
78	C8–S9	σ	C6–C7	σ*	4.85	1.16	0.068
79	C8–S9	σ	C7–N11	σ*	1.25	1.18	0.034
80	C8–S9	σ	C10–N11	σ*	0.65	1.23	0.025
81	C8–S9	σ	C10–N18	σ*	4.18	1.11	0.061
82	C8–H24	σ	C7–C8	σ*	1.89	1.07	0.04
83	C8–H24	σ	C7–N11	σ*	3.81	1.02	0.056
84	C8–H24	σ	S9–C10	σ*	0.74	0.7	0.021
85	S9–C10	σ	C6–C7	σ*	0.98	1.14	0.03
86	S9–C10	σ	C8–H24	σ*	3.48	1.17	0.057
87	S9–C10	σ	N18–C19	σ*	4.13	1.12	0.061
88	S9–C10	σ	N18–H28	σ*	0.73	1.14	0.026
89	C10–N11	σ	C6–C7	σ*	4.01	1.33	0.066
90	C10–N11	σ	C7–N11	σ*	1.33	1.35	0.038
91	C10–N11	σ	C10–N18	σ*	1.99	1.29	0.045
92	C10–N11	σ	N18–H28	σ*	1.16	1.33	0.035
93	**C10–N11**	**π**	**C7–C8**	**π***	**19.53**	**0.33**	**0.076**
94	C10–N11	π	C10–N11	π*	0.79	0.31	0.015
95	C10–N18	σ	C7–N11	σ*	2.74	1.31	0.054
96	C10–N18	σ	C10–N11	σ*	2.1	1.36	0.048
97	C10–N18	σ	N18–C19	σ*	1.3	1.27	0.037
98	C10–N18	σ	N18–H28	σ*	0.78	1.29	0.028
99	C10–N18	σ	C19–O20	σ*	1.69	1.38	0.043
100	N13–C14	σ	C2–S3	σ*	2.78	0.98	0.047
101	N13–C14	σ	C2–N13	σ*	2.52	1.26	0.051
102	N13–C14	σ	N13–H25	σ*	0.52	1.24	0.023
103	N13–C14	σ	C14–C16	σ*	0.58	1.17	0.024
104	N13–C14	σ	C16–Cl17	σ*	1.33	0.95	0.032
105	N13–H25	σ	N1–C2	σ*	5.17	1.19	0.07
106	N13–H25	σ	C2–N13	σ*	0.54	1.12	0.022
107	N13–H25	σ	C14–O15	σ*	1.3	1.23	0.036
108	N13–H25	σ	C14–C16	σ*	3.49	1.03	0.054
109	C14–O15	σ	C2–N13	σ*	2.74	1.48	0.057
110	C14–O15	σ	N13–C14	σ*	0.54	1.45	0.025
111	C14–O15	σ	C14–C16	σ*	1.63	1.39	0.043
112	C14–O15	π	C14–O15	π*	0.9	0.36	0.017
113	C14–O15	π	C16–H26	σ*	1.43	0.75	0.029
114	C14–O15	π	C16–H27	σ*	1.53	0.72	0.03
115	C14–C16	σ	N13–H25	σ*	2.12	1.08	0.043
116	C14–C16	σ	C14–O15	σ*	1.29	1.21	0.035
117	C16–Cl17	σ	N13–C14	σ*	3.77	1.08	0.058
118	**C16–Cl17**	**σ**	**C14–O15**	**σ***	**0.51**	**1.22**	**0.022**
119	C16–H26	σ	C14–O15	σ*	2.24	1.06	0.044
120	C16–H26	σ	C14–O15	π*	5.94	0.51	0.052
121	C16–H26	σ	C16–Cl17	σ*	0.58	0.64	0.017
122	C16–H27	σ	C14–O15	σ*	2.15	1.06	0.043
123	C16–H27	σ	C14–O15	π*	4.64	0.51	0.046
124	C16–H27	σ	C16–Cl17	σ*	0.71	0.64	0.019
125	N18–C19	σ	S9–C10	σ*	2.26	0.98	0.043

Table 7 (*Contd.*)

S. no.	Donor (i)	Type	Acceptor (j)	Type	E^2 (kcal mol^{-1})	$E_i - E_j$	$F_{i,j}$
126	N18–C19	σ	C10–N18	σ*	2.12	1.23	0.046
127	N18–C19	σ	N18–H28	σ*	0.69	1.27	0.026
128	N18–C19	σ	C19–C21	σ*	0.63	1.2	0.025
129	N18–C19	σ	C21–Cl22	σ*	1.48	0.97	0.034
130	N18–H28	σ	C10–N11	σ*	5.02	1.19	0.069
131	N18–H28	σ	C19–O20	σ*	0.95	1.21	0.03
132	N18–H28	σ	C19–C21	σ*	3.52	1.05	0.055
133	C19–O20	σ	C10–N18	σ*	2.56	1.41	0.054
134	C19–O20	σ	N18–C19	σ*	0.92	1.43	0.033
135	C19–O20	σ	C19–C21	σ*	1.48	1.38	0.041
136	C19–O20	π	C19–O20	π*	0.85	0.35	0.016
137	C19–O20	π	C21–H29	σ*	1.48	0.75	0.03
138	C19–O20	π	C21–H30	σ*	2.2	0.7	0.035
139	C19–C21	σ	N18–C19	σ*	0.55	1.09	0.022
140	C19–C21	σ	N18–H28	σ*	2.28	1.11	0.045
141	C19–C21	σ	C19–O20	σ*	1.22	1.2	0.034
142	C21–Cl22	σ	N18–C19	σ*	3.35	1.08	0.055
143	C21–Cl22	σ	C19–O20	σ*	0.61	1.19	0.024
144	C21–H29	σ	C19–O20	σ*	2.43	1.04	0.045
145	C21–H29	σ	C19–O20	π*	4.06	0.51	0.043
146	C21–H30	σ	C19–O20	σ*	0.97	1.03	0.028
147	C21–H30	σ	C19–O20	π*	5.29	0.5	0.049
148	C21–H30	σ	C21–Cl22	σ*	0.68	0.63	0.019
149	N1	LP1	C2–S3	σ*	17.41	0.52	0.085
150	N1	LP1	C2–N13	σ*	2.25	0.8	0.039
151	N1	LP1	C4–C5	σ*	5.23	0.86	0.061
152	N1	LP1	C5–C6	σ*	0.91	0.78	0.024
153	N1	LP1	C16–Cl17	σ*	1.46	0.48	0.024
154	S3	LP1	N1–C2	σ*	3.63	1.17	0.058
155	S3	LP1	C4–C5	σ*	2.08	1.16	0.044
156	S3	LP2	N1–C2	π*	33.32	0.23	0.08
157	S3	LP2	C4–C5	π*	21.08	0.26	0.067
158	S9	LP1	C7–C8	σ*	2.04	1.16	0.044
159	S9	LP1	C10–N11	σ*	3.16	1.16	0.054
160	S9	LP2	C7–C8	π*	23.71	0.26	0.071
161	S9	LP2	C10–N11	π*	31.24	0.23	0.076
162	N11	LP1	C6–C7	σ*	1.87	0.79	0.035
163	N11	LP1	C7–C8	σ*	6.61	0.86	0.069
164	N11	LP1	S9–C10	σ*	17.14	0.5	0.083
165	N11	LP1	C10–N18	σ*	2.62	0.75	0.041
166	N11	LP1	C21–Cl22	σ*	1.21	0.48	0.022
167	O12	LP1	C5–C6	σ*	1.96	1.1	0.042
168	O12	LP1	C6–C7	σ*	2.58	1.11	0.048
169	O12	LP2	C5–C6	σ*	18.86	0.68	0.102
170	O12	LP2	C6–C7	σ*	17.86	0.68	0.099
171	O12	LP2	C7–N11	σ*	0.59	0.7	0.019
172	**N13**	**LP1**	**N1–C2**	**π***	**55.92**	**0.25**	**0.107**
173	N13	LP1	C14–O15	π*	49.44	0.27	0.107
174	O15	LP1	N13–C14	σ*	1.03	1.07	0.03
175	O15	LP1	C14–C16	σ*	2.5	1.02	0.046
176	O15	LP2	C2–N13	σ*	1.1	0.69	0.025
177	O15	LP2	N13–C14	σ*	23.29	0.65	0.111
178	O15	LP2	C14–C16	σ*	20.73	0.59	0.1
179	Cl17	LP2	C16–H26	σ*	4.3	0.67	0.048
180	Cl17	LP2	C16–H27	σ*	4.72	0.64	0.049
181	Cl17	LP3	N13–C14	σ*	0.84	0.68	0.022
182	Cl17	LP3	C14–C16	σ*	5.73	0.63	0.054
183	Cl17	LP3	C16–H26	σ*	2.13	0.67	0.034
184	**Cl17**	**LP3**	**C16–H27**	**σ***	**0.53**	**0.64**	**0.017**
185	N18	LP1	C10–N11	π*	51.61	0.24	0.102
186	**N18**	**LP1**	**C19–O20**	**π***	**53.66**	**0.27**	**0.111**
187	O20	LP1	N18–C19	σ*	1.65	1.09	0.038
188	O20	LP1	C19–C21	σ*	2.26	1.04	0.044
189	O20	LP2	C10–N18	σ*	0.58	0.63	0.017
190	O20	LP2	N18–C19	σ*	23.66	0.65	0.112
191	O20	LP2	C19–C21	σ*	19.2	0.6	0.097
192	Cl22	LP2	C21–H29	σ*	4.01	0.68	0.047
193	Cl22	LP2	C21–H30	σ*	3.31	0.63	0.041
194	Cl22	LP3	N18–C19	σ*	0.64	0.69	0.019
195	Cl22	LP3	C19–C21	σ*	6.09	0.64	0.056
196	Cl22	LP3	C21–H29	σ*	0.54	0.68	0.017
197	Cl22	LP3	C21–H30	σ*	2.38	0.63	0.035
198	N1–C2	π*	C4–C5	π*	69.71	0.02	0.063
199	N1–C2	π*	C14–O15	π*	0.56	0.03	0.006
200	C4–C5	π*	C4–C5	σ*	0.7	0.51	0.042
201	C4–C5	π*	C6–C7	σ*	0.57	0.43	0.033
202	C6–O12	π*	N1–C5	σ*	0.59	0.39	0.042
203	C7–C8	π*	C6–O12	π*	105.05	0.02	0.077
204	C10–N11	π*	C7–C8	π*	84.14	0.03	0.071
205	C10–N11	π*	C19–O20	π*	0.53	0.03	0.006
206	C14–O15	π*	C16–H26	σ*	0.79	0.39	0.044
207	C14–O15	π*	C16–H27	σ*	1.07	0.36	0.05
208	C19–O20	π*	C21–H29	σ*	0.83	0.4	0.045
209	C19–O20	π*	C21–H30	σ*	1.58	0.35	0.057

[a] *$E^{(2)}$ means the energy of the hyper-conjugative interaction (stabilization energy in kcal mol^{-1}). *Energy difference $E_{(j)} - E_{(i)}$ between the donor and acceptor i and j NBO orbitals. *$F_{(i,j)}$ is the Fock matrix element between the i and j NBO orbitals.

to calculated the values of energy gap, softness and hardness, electronegativity and chemical potential. All the calculated energy parameters with their values are shown in Table 5. First descriptive parameter E_{HOMO} is shown in Table 5, and its high value shows that it can donate electron to acceptor molecules. A higher value of E_{HOMO} is also favorable to the biological activity of compound. Compound **6i** is a better electron donor than compound **6h** due to its high value. The second descriptive parameter is E_{LUMO}, and its low value shows that it can accept electrons from the donating molecule. A lower value of E_{LUMO} also increases the biological activity of the compound. Compound **6i** is a better electron acceptor than compound **6h** due to its lower value. Third descriptive parameter is energy gap (ΔE) calculated by the HOMO–LUMO values, where the HOMO is more stable than the LUMO. Compound **6i** shows a smaller value of energy gap than compound **6h**. A smaller energy gap value shows that compound **6i** is chemically more reactive and biologically more active.

Frontier molecular orbital (FMO) studies can investigate the structure–activity relationship and bioactivities of these synthesized compounds for drug designing. The HOMO value is higher in compound **6i**, which shows that it could be a good electron donor drug. Compound **6i** is more reactive and more accepting than the other compound **6h** due to its lower ionization potential (I), higher electron affinity (A), lower absolute hardness (η), higher absolute softness (σ), higher electronegativity (χ), lower chemical potential (CP) and higher electrophilicity index (ω).

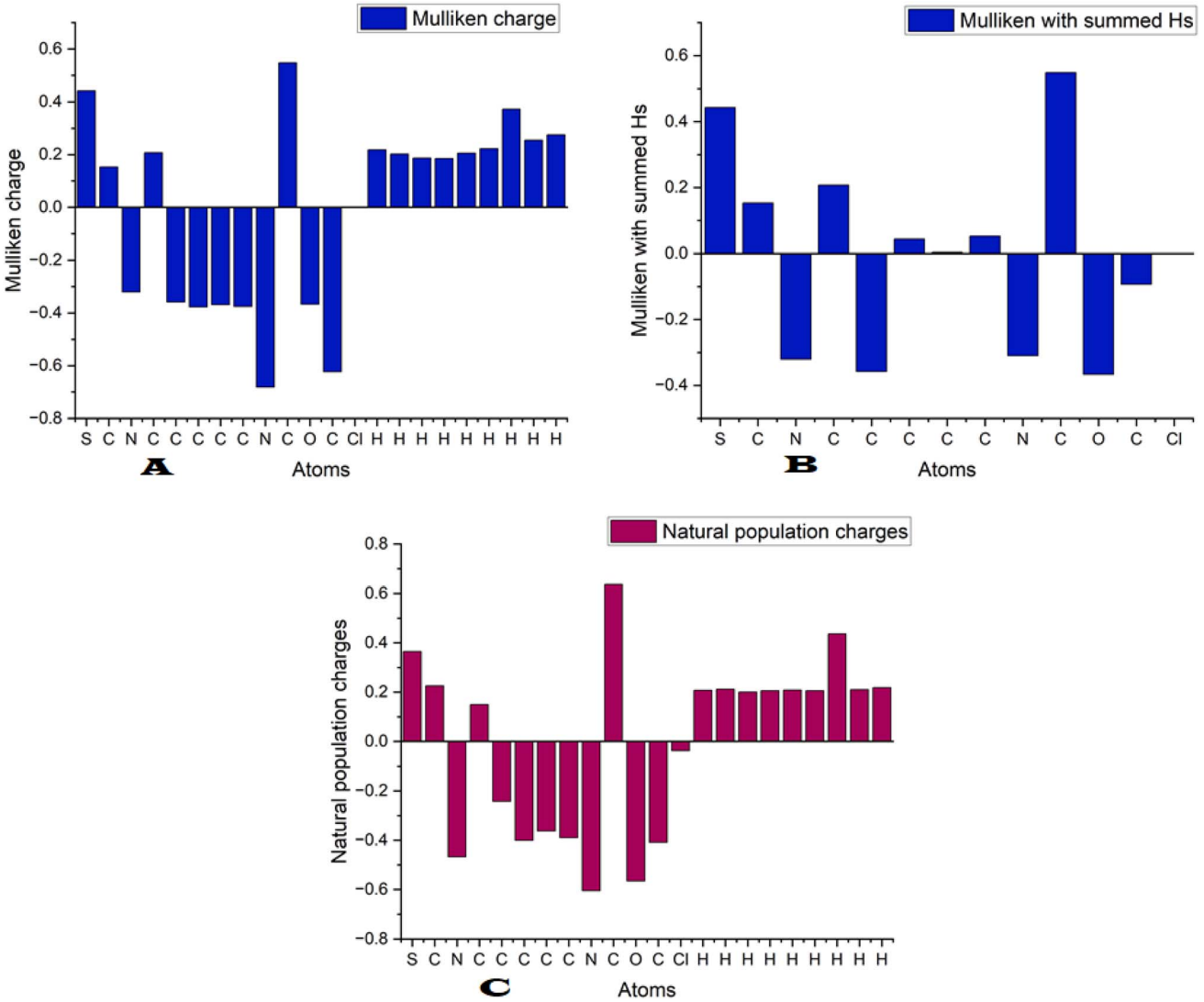

Fig. 20 Atomic charge analysis: (A) graphical representation of Mulliken's charges for compound **6h**, (B) graphical representation of Mulliken's charges with summed hydrogen atoms for compound **6h** and (C) natural population charges (NPA) for compound **6h**.

3.5.4. Molecular electrostatic potential (MEP). The determination of chemical mechanism and investigation of compounds can be done by calculating the MEP contour and map. Hydrogen bonding interaction and electrophilic–nucleophilic behavior of compounds can also be interpreted by MEP. MEP calculations using the Gaussian09W software give us some important indication about molecules by negative, positive and neutral electrostatic potential. The MEP scale gives us information about the relationship of physicochemical properties with the structure of compounds of drugs.[47] The MEP contour and map of compounds **6h** and **6i** were calculated using the same B3LYP 6-311G basis set of DFT.

In MEP, the negatively charged red-yellow color region of electrostatic potential shows the electrophilic attack sites, where O atoms can react with electrophiles, while the positively charged blue region of electrostatic potential showed nucleophilic attack sites where H atoms can react with nucleophiles. The green color showed the neutral reactivity, and the benzene ring remained neutral.[48] The molecular electrostatic potential (MEP) contour and map are shown in Fig. 24.

3.5.5. IR analysis. In IR spectroscopic analysis, functional group moieties were determined by vibrational modes, which are present in a molecule. Theoretical calculations were performed for compounds **6h** and **6i** to gain vibrational analysis information with the 6-311G B3LYP basis set to generate FTIR spectra using an FT-Raman spectrophotometer, which is presented in Table 8. As we study these compounds, compound **6h** contains 22 atoms with 60 normal vibrations modes, while compound **6i** contains 30 atoms with 84 normal modes of vibrations by these calculations. Fig. 20a and b show the comparison graphs between the experimental and theoretical FTIR data of compounds **6h** and **6i**.

3.5.5.1. N–H, C–N and C=N vibrations. The IR vibrational peaks value range for heterocyclic compound where amines (N–H) stretching vibration are from 3200 cm^{-1} to 3500 cm^{-1}.[49] As the N–H, C=O, and C–H vibrational modes show the maximum

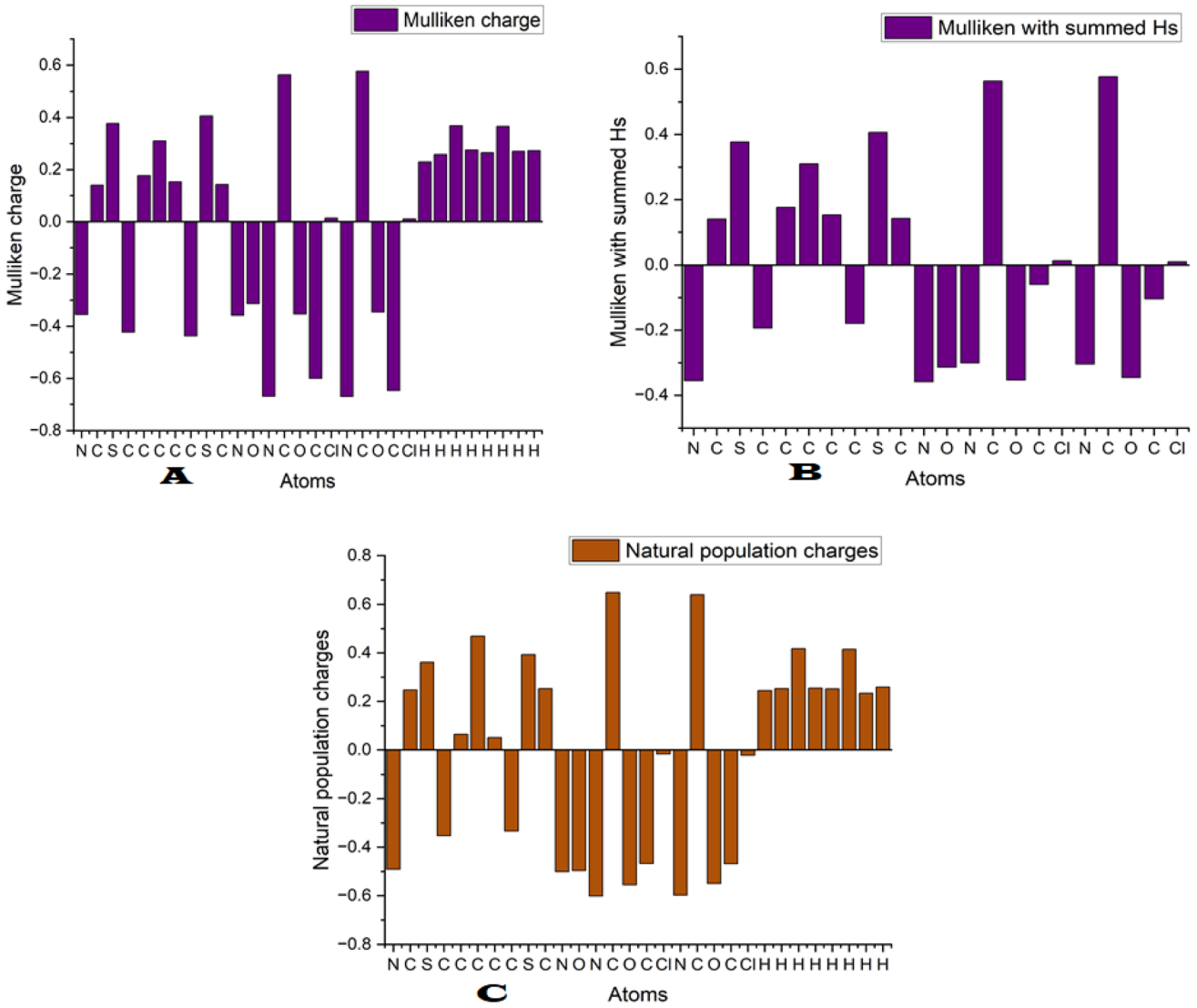

Fig. 21 Atomic charge analysis: (A) graphical representation of Mulliken's charges for compound **6i**, (B) graphical representation of Mulliken's charges with summed hydrogen atoms for compound **6i** and (C) natural population charges (NPA) for compound **6i**.

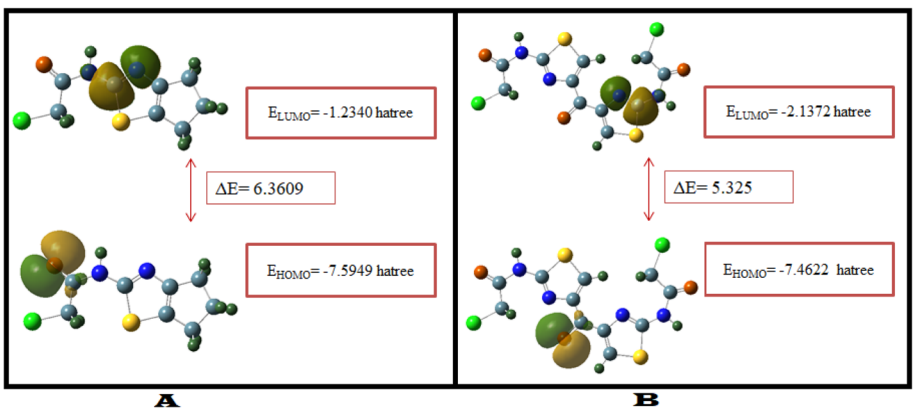

Fig. 22 Contour diagram of HOMO–LUMO of compounds **6h** (A) and **6i** (B) with their energy gap.

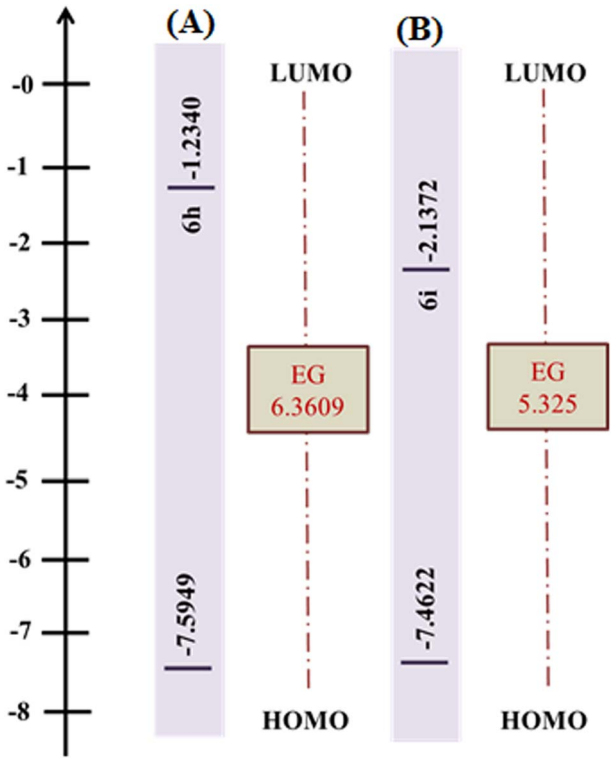

Fig. 23 HOMO–LUMO energy diagram of compounds **6h** (A) and **6i** (B) with their energy gap.

intensity and high polarity. In compound **6h**, two polar stretching vibrations are shown for the N–H group at 3310.79 cm^{-1} and 3344.59 cm^{-1}, while the experimental value peak assigned to the N–H stretching vibration appears at 3319.15 cm^{-1}. There is a little difference between experimental and theoretical wavenumbers because it is sensitive to hydrogen bonding with the oxygen atom of carbonyl functional groups in the H–N–C–O interaction. The bending N–H vibration ranges from 1500 cm^{-1} to 1650 cm^{-1}, and this one is experimentally observed at 1584.04 cm^{-1}. We observed the C=N functional group stretching vibrations at 1640.60 cm^{-1} experimentally that well match to range found in litrature start from 1610 cm^{-1} to 1660 cm^{-1}. The thiazole ring consists of a 5-membered ring with a delocalized π-system. The C–N interaction is in plane ring bending vibration. Which is observed from 1020 cm^{-1} to 1360 cm^{-1} theoretically and experimentally, and the aromatic C–N vibration is observed at 1117.57 cm^{-1} and the C–N stretching vibration at 1228.02 cm^{-1} (Fig. 25).

In compound **6i**, one stretching vibration is shown for the N–H functional group at 3371.92 cm^{-1} while experimentally at 3383.72 cm^{-1}. The experimental and theoretical values show a difference in wavenumber due to hydrogen bonding with the oxygen atom of carbonyl group in both H–N–C–O interactions. The N–H bending vibrations are observed theoretically at 1545.17 cm^{-1} and 1604.15 cm^{-1} and experimentally at 1574.54 cm^{-1}. In compound **6i**, the C=N functional group experimentally shows stretching vibrations at 1630.14 cm^{-1}, which is in the range from 1610 cm^{-1} to 1660 cm^{-1}. C–N vibrations are stretched in-plane that are observed at 1132.11 cm^{-1} and 1229.10 cm^{-1} theoretically and experimentally observed at 1118.70 cm^{-1} and 1224.23 cm^{-1} (Fig. 26).

3.5.5.2. Carbonyl group (C=O) vibrations. The IR vibrational range for the carbonyl group (C=O) was reported to be from 1630 cm^{-1} to 1850 cm^{-1},[50] while the stretching vibrational range for the ketonic carbonyl (C=O) group is from 1650 cm^{-1} to 1850 cm^{-1}. In compound **6h**, two modes of vibrations are at 1676.28 cm^{-1} and 1766.76 cm^{-1} with the highest potential energy distribution (PED) contribution of 72%. This ketonic carbonyl (C=O) group, which is highly polarized (π-bond), shows the symmetric stretching vibrational mode at 1676.28 cm^{-1}, as predicted by the IR data. The experimental value of this ketonic carbonyl group is shown at 1667.22 cm^{-1}. In compound **6i**, three modes of vibrations are shown at 1655.08 cm^{-1}, 1667.57 cm^{-1} and 1711.73 cm^{-1} with the highest PED contribution. Theoretically, this ketonic carbonyl (C=O), which is polar in nature, shows the stretching vibrations at 1655.08 cm^{-1}, while the experimental value of the carbonyl functional group was observed at 1654.82 cm^{-1}.

3.5.5.3. Aromatic ring C–H vibrations. The aromatic ring C–H vibrations are reported at 3000 cm^{-1} to 3100 cm^{-1}, and the aliphatic C–H vibrations are reported at 2850 cm^{-1} to 2960 cm^{-1}.[50] In the IR study, theoretical and experimental calculations of C–H vibrations are observed right after the N–H vibrations. In compound **6h**, the aromatic ring C–H vibrations range from 2885.84 cm^{-1} to 3068.29 cm^{-1} theoretically and C–H vibrations are observed at 2979.28 cm^{-1} for experimental calculations. In compound **6i**, the C–H vibrational modes are theoretically observed at 2964.47 cm^{-1} and 3053.76 cm^{-1} but experimentally no C–H stretching vibration peaks were observed in **6i** compound.

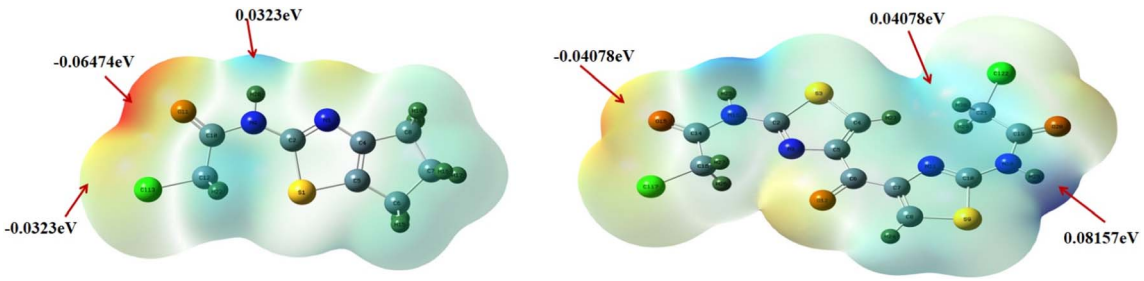

Fig. 24 Molecular electrostatic potential (MEP) contour and map of compounds **6h** and **6i**.

Table 8 Chemical shift (δ) values of ^{1}H and ^{13}C NMR of compounds **6h** and **6i**

Carbon	δ_C experimental	δ_C theoretical	Proton	δ_H experimental	δ_H theoretical
6h Compound					
10-C	164.2	158.8581	20-H	12.5	7.985457
2-C	—	157.5015	21-H	4.28	6.401765
4-C	148.2	153.7083	22-H	4.28	5.7118
5-C	118.9	124.8353	17-H	2.54	4.081958
12-C	—	47.99194	14-H	2.87	3.871611
7-C	26.0	29.11105	18-H	2.52	3.657483
8-C	30.9	21.45014	15-H	2.87	3.482611
6-C	28.2	18.3616	16-H	2.54	3.102562
			19-H	2.52	2.79344
6i Compound					
6-C	192.9	197.9515	24-H	8.98	7.796086
14-C	—	188.8477	23-H	8.98	7.606245
19-C	—	187.3156	25-H	12.4	7.030382
10-C	—	177.1132	28-H	12.4	6.484283
2-C	—	172.8862	27-H	4.87	5.484209
5-C	113.9	172.265	30-H	4.87	5.305767
7-C	164.5	166.9709	26-H	4.87	5.073771
4-C	144.2	158.5567	29-H	4.87	4.94707
8-C	42.7	148.9024			
16-C	—	67.20365			
21-C	—	65.9386			

3.5.5.4. C–Cl vibrations. The stretching vibrational frequency for C–Cl ranges between 600 cm^{-1} and 800 cm^{-1} (Bisong *et al.*, 2020). Chlorine is a heavy atom (in mass in comparison to hydrogen and carbon) and electron withdrawing that lowers the vibrational wavenumber due to this heavy atom of chlorine. In compound **6h**, the stretching vibrations of C–Cl occur from 627.95 cm^{-1} to 792.11 cm^{-1}. The C–Cl vibrational frequency mode was observed at 679.62 cm^{-1} theoretically and at 672.37 cm^{-1} experimentally. In compound **6i**, the stretching vibrations of C–Cl are observed in the range from 622.31 cm^{-1} to 795.62 cm^{-1}. The C–Cl functional group was observed at 661.28 cm^{-1} wavenumber theoretically and at 670.82 cm^{-1} wavenumber experimentally.

3.5.6. NMR analysis. Nuclear magnetic resonance (NMR) is a spectroscopic technique used to understand the organic compound structure. The computational study was performed using Gaussian 09W for theoretical information, which is later used for the validation of experimental results. The computational study was conducted using the GIAO method for proton (^{1}H) and carbon (^{13}C) NMR spectra of the synthesized compounds **6h** and **6i** at the B3LYP 6-311G basis set.[51] The

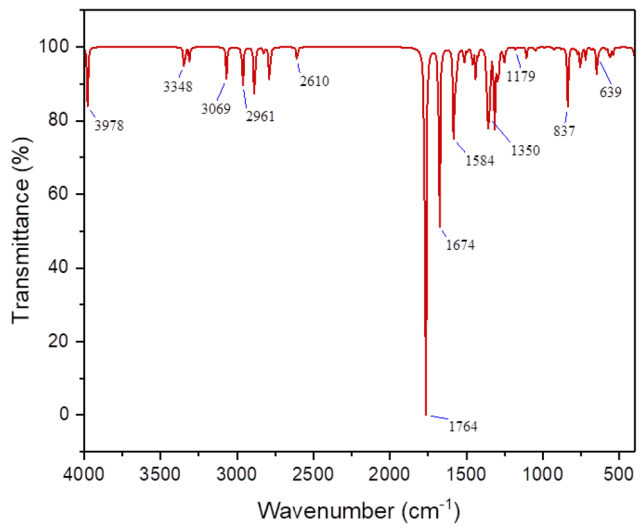

Fig. 25 Theoretical vibrational analysis of compound **6h** in the IR study.

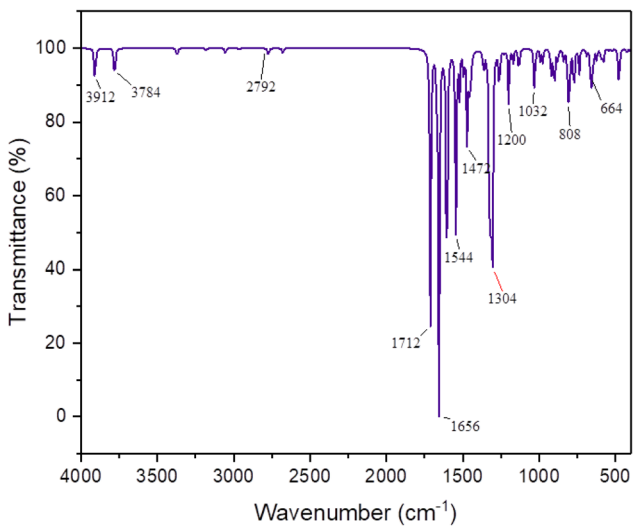

Fig. 26 Theoretical vibrational analysis of compound **6i** in the IR study.

chemical shift values of ^{1}H and ^{13}C NMR for these compounds are presented in ppm along with the reference of TMS in Table 8.

Theoretical and experimental shift values of ^{13}C NMR for these compounds are accordance to each other and their experimental values are observed by dissolving in DMSO solvent. For **6h** compound, experimental chemical shift value range from C-6 to C-10 is 164.2 ppm–28.2 ppm. In ^{13}C NMR analysis, 10-C in **6h** compound show the highest peak in theoretical study at 158.85 ppm and in experimental show at 164.2 ppm due to the ketonic group presence. 4-C and 5-C in compound **6h** show aromatic carbon shift values at 153.70 ppm and 124.83 ppm (Fig. S28 (SI)).

For the ^{1}H NMR study, the theoretical values of compound **6h** were compared with the experimental values. In the proton NMR, 20-H shows the anomalously high chemical shift value at 7.985 ppm, while the experimental value at 12.5 ppm confirms the intramolecular H-bonding because this is attached to the nitrogen atom. In experimental proton NMR analysis, protons 21-H, 22-H shows same peaks at 4.28 ppm, 14-H, 15-H shows same peaks at 2.87 ppm while 18-H, 19-H also show same peaks at 2.52 ppm. The experimental and theoretical analysis comparison for proton and carbon NMR of compound **6h** in graphical representation is shown in Fig. S29 (SI).

For compound **6i**, both proton and carbon NMR chemical shift values were analyzed by dissolving this compound in a DMSO solvent. In ^{13}C NMR spectral data analysis, 6-C in **6i** compound show the highly de-shielded effect with the highest peak at 192.9 ppm in experimental spectrum and in theoretical spectral data show chemical shift value at 197.95 ppm due to the carbonyl group adjacent to electron withdrawing oxygen atom (O-12). In compound **6i**, 8-C adjacent to S-9 shows the lowest chemical shift value for theoretical 148.90 ppm and experimental 42.7 ppm due to the electron-donating effect from sulfur and the shielding effect. In compound **6i**, 2-C and 5-C show the same aromatic carbon shift values at 172.88 ppm and 172.26 ppm (Fig. S30: SI).

In the ^{1}H NMR analysis of **6i** compound, 23-H to 30-H protons show the experimental chemical shift range from 12.4 to 4.87 ppm and the theoretical range from 7.796 to 4.947 ppm; 26-H, 27-H, 29-H and 30-H show the same peak value at 4.87 ppm; 24-H proton attaches on 8-C, which is near S-9, showing the deshielding effect due to potential hydrogen bonding, at chemical shifts of 7.80 ppm theoretically and 8.98 ppm experimentally; and 25-H and 28-H protons attach to the electronegative atom (N13, N18), showing intramolecular hydrogen bonds due to the strong deshielding effect and a high chemical shift value at 12.4 ppm. The comparison of theoretical and experiment analyses of ^{1}H NMR and ^{13}C NMR for compound **6i** in graphical representation is shown in Fig. S31 (SI).

3.5.7. Hirshfeld surface population analysis. The charge distribution analysis of the compound **6h** by Hirshfeld surface showed the details of its electronic distribution and charge of atoms. The sulfur atom (atom 1) has a moderately positive Hirshfeld charge (Q-H = 0.0526), indicating that there is a weak electron donation. The nitrogen atoms present at position 3 and 9 in compound **6h** have quite negative Hirshfeld charges (Q-H = −0.223 and −0.100), which suggests that they are highly electronegative and partake of electron-rich sites (Table 9). Oxygen atom (atom 11) displays a great negative charge (Q-H = −0.280) consistent with its functionality as a major site of electron withdrawals. Carbon atoms are distributed with positive–negative Hirshfeld charge degrees, starting with slightly positive (*e.g.*, atom 2 at Q-H = 0.101) through to about modestly negative (*e.g.*, atoms 5 to 8 at Q-H = −0.045 to −0.052), due to the distinct binding surroundings in the molecule. These hydrogen atoms are uniformly and strongly positively charged and the maximum possible Hirshfeld value is found in atom 20 (Q-H = 0.160), probably because such an atom is attached to a highly electronegative or conjugated system. The above discussed trends are confirmed by CM5 charges (Q-CM5) as the values of electronegative atoms are highly negative (up to −0.430 at nitrogen), whereas the values of hydrogen atoms are large positive (*e.g.*, +0.362 in atom 20). The molecule is therefore significantly polarized toward charges. The chlorine atom (atom 13) also has a slightly negative charge (Q-H = −0.106), and this takes part in electron-withdrawing properties in its immediate vicinity. In general, the Hirshfeld and CM5 studies of compound **6h** promote a sense of the existence of easily recognizable regions of electron richness and electron deficiency, which is essential in terms of understanding its chemical reactivity and possible interaction (Fig. 27 and Table 9).

The Hirshfeld analysis for the charge distribution of compound **6i** offers the specific observation of the electronic structure: The computed Hirshfeld charges (Q-H) confirm that electronegative atoms, *i.e.*, oxygen (*e.g.*, atoms 12 and 15) have quite negative values (Q-H = 0.268–0.270), which means that they very actively attract electrons. The nitrogen atoms (*e.g.*, atoms present at position-1, 11, 13 and 18) also have negative charges (Q-H 10 −0.10 to −0.20), in agreement with the electronegativity (Table 10). Contrastingly, the hydrogen atoms portray a positive charge because the values acquire high values of up to Q-H = 0.156 (atom 25), implying that they may be involved in polar bonding. The Hirshfeld charges of sulfur atoms (atoms 3 and 9) are moderately positive (∼0.078 to 0.101), and the carbon atoms exhibit different values, which are indicators of different bonding conditions at all points of the molecule. These observations are supported by the Q-CM5 charges, which give good charge estimate that takes into consideration the molecular dipoles where oxygen and nitrogen atoms have very negative values (up to −0.43) and hydrogen has highly positive values (up to 0.35). There is also a slight negative charge on the Cl atoms (atoms 17 and 22), which is indicative of certain level of localization of the electronic density. Altogether, the distribution of the charge in compound **6i** indicates the presence of specific areas of electron density, which affects the chemical reactivity and could undergo biological processes or interactions with other molecules (Fig. 28 and Table 10).

3.5.8. Non-covalent bond interactions (NCI) analysis. Fig. 29 presents the diagram detailing non-covalent interaction (NCI) and reduced density gradient (RDG) plot of the compound **6h** using density functional theory (DFT). Fig. 29 (part A) depicts the molecular structure of **6h**, as shown in the colored

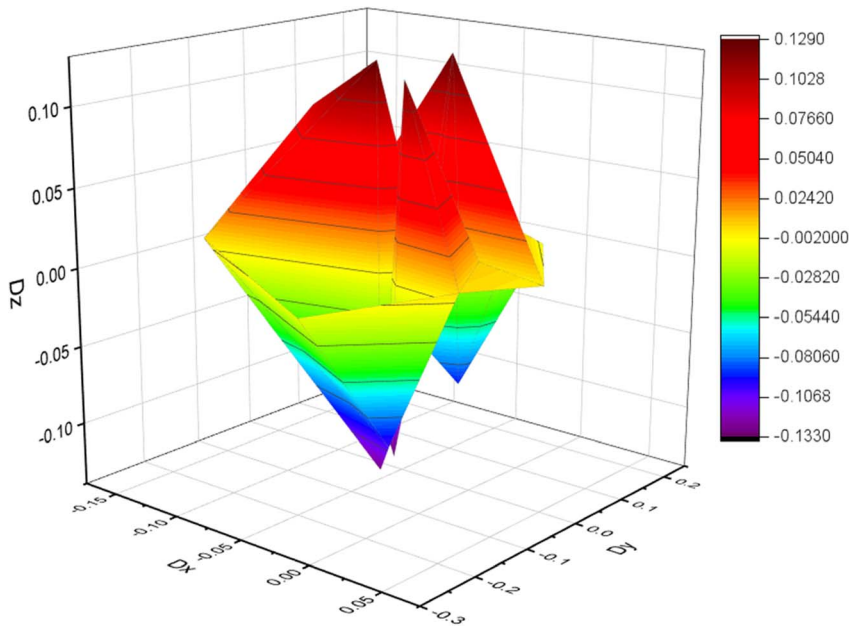

Fig. 27 Graphical representation of Hirshfeld dipoles for compound **6h**.

isosurfaces to indicate the presence of different non-covalent interactions. Green isosurfaces show weak van der Waals forces, blue surfaces show strong attractive forces including hydrogen bonding and red colors are abolished by steric repulsion. The RDG *versus* $(\lambda_2)\rho$ plot shown in Fig. 29 (part B) is utilized to determine the nature and the strength of these interactions. Attractive interactions (blue) are represented by the negative values of $(\lambda_2)\rho$, which are close to zero values, indicated by green color (van der Waals interactions), and repulsive interactions, indicated by red color, by a positive value of $(\lambda_2)\rho$. This analysis helps to have a detailed visualization of how non-covalent forces are adding to the stability and electron structure of the compound **6h**.

Fig. 30 shows the non-covalent interaction (NCI) and reduced density gradient (RDG) of compound **6i**, which provides an understanding and visualizes weak intermolecular and intramolecular interactions using DFT-calculated electron density. In Fig. 30 (part A), the 3D isosurface of the NCI is

Table 9 Hirshfeld charges and dipoles on all atoms of compound **6h**

S. no.	Atoms	Q-H	S–H	D_x	D_y	D_z	Q-CM5
1	S	0.052581	0	−0.10383	0.10676	0.012915	0.032333
2	C	0.101472	0	0.072774	−0.01084	−0.00544	0.253843
3	N	−0.22317	0	−0.03542	−0.23115	−0.0091	−0.39461
4	C	0.025584	0	−0.01655	0.140314	0.011738	0.085696
5	C	−0.05204	0	0.027068	−0.10138	0.004714	−0.04235
6	C	−0.05184	0	−0.02789	−0.01269	0.00077	−0.15253
7	C	−0.04559	0	0.005154	−0.00031	0.008675	−0.15263
8	C	−0.04892	0	−0.00988	0.011386	0.0008	−0.14731
9	N	−0.10035	0	−0.01429	0.016501	0.004748	−0.42946
10	C	0.191464	0	−0.031	0.009398	−0.00082	0.279809
11	O	−0.28036	0	−0.15658	−0.12058	0.004974	−0.31793
12	C	−0.00226	0	0.045451	0.013045	0.000319	−0.09221
13	Cl	−0.10608	0	−0.11253	0.020695	−0.00369	−0.11463
14	H	0.043254	0	−0.02216	−0.07298	0.1212	0.097898
15	H	0.045233	0	−0.02097	−0.10242	−0.10264	0.099879
16	H	0.040062	0	−0.0553	−0.00196	−0.13263	0.095082
17	H	0.041387	0	−0.11082	−0.01974	0.0903	0.095657
18	H	0.04457	0	−0.03512	0.055456	0.127172	0.100274
19	H	0.047426	0	−0.04472	0.102661	−0.09445	0.103257
20	H	0.160124	0	−0.01795	0.205089	−0.00488	0.362167
21	H	0.058132	0	−0.04787	−0.05699	0.128317	0.118357
22	H	0.059331	0	−0.04155	−0.06482	−0.12844	0.119429

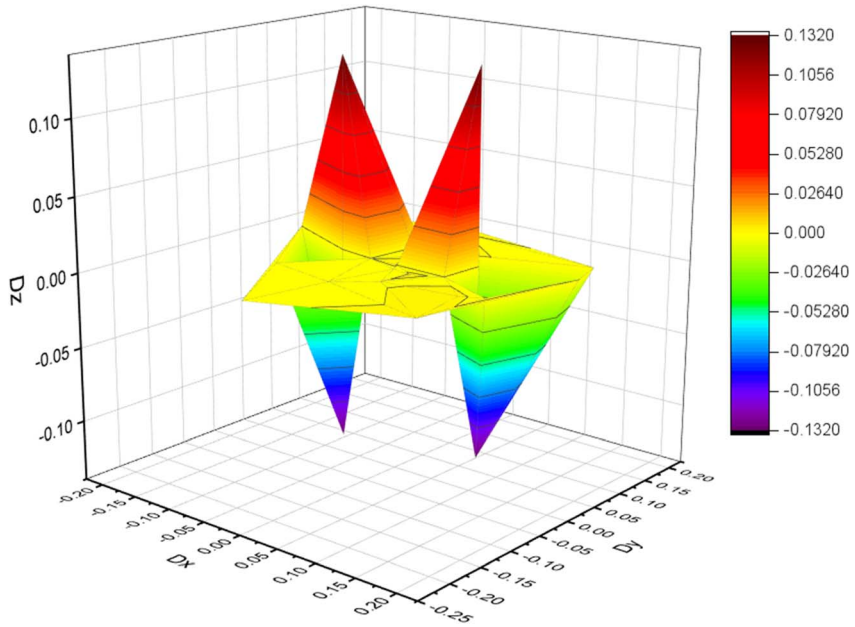

Fig. 28 Graphical representation of Hirshfeld dipoles for compound **6i**.

displayed the molecular conformation that green surfaces demonstrate van der Waals weak interactions, blue surfaces denote an attractive hydrogen bond formation interaction and red surfaces exemplify steric repulsion. Fig. 30 (part B) presents the RDG *vs.* sign $(\lambda_2)\rho$ scatter plot, whose distribution of points tells something about the strength and nature of non-covalent

Table 10 Hirshfeld charges and dipoles on all atoms of compound **6i**

S. no.	Atoms	Q-H	S–H	D_x	D_y	D_z	Q-CM5
1	N	−0.1934	0	0.124148	−0.1293	-3.7×10^{-5}	−0.35937
2	C	0.112533	0	−0.05472	−0.04975	0.000005	0.249657
3	S	0.078672	0	−0.01072	0.154275	-8×10^{-6}	0.069008
4	C	−0.05531	0	0.028256	−0.06034	-8×10^{-6}	−0.08712
5	C	0.028273	0	−0.02864	0.067994	-1.6×10^{-5}	0.092246
6	C	0.128231	0	0.008871	−0.01393	-9.4×10^{-5}	0.162595
7	C	0.027198	0	−0.01117	−0.09745	-6.3×10^{-5}	0.087222
8	C	−0.03866	0	0.019808	0.078705	0.000055	−0.09341
9	S	0.10149	0	−0.09922	−0.07953	-6.4×10^{-5}	0.108364
10	C	0.112308	0	0.067035	−0.00326	-1.6×10^{-5}	0.268064
11	N	−0.20562	0	−0.01548	0.170965	0.000133	−0.3839
12	O	−0.26821	0	0.134528	−0.13756	0.000034	−0.29944
13	N	−0.10363	0	0.002612	−0.00013	-3.7×10^{-5}	−0.43416
14	C	0.204433	0	0.036435	−0.01995	0.000017	0.291084
15	O	−0.2701	0	0.177188	0.081351	0.000013	−0.30814
16	C	0.006357	0	−0.03602	0.002269	-7×10^{-6}	−0.08273
17	Cl	−0.12025	0	0.120082	−0.05079	0.000017	−0.12857
18	N	−0.10332	0	−0.00086	0.000943	0.000071	−0.43433
19	C	0.203106	0	−0.01197	0.036074	-3.4×10^{-5}	0.290233
20	O	−0.26493	0	−0.18201	0.057322	-3.9×10^{-5}	−0.30305
21	C	0.002207	0	0.033044	−0.02387	0.000003	−0.08757
22	Cl	−0.10675	0	−0.04483	0.09918	-3×10^{-6}	−0.11516
23	H	0.063078	0	0.143825	−0.03779	-2.8×10^{-5}	0.126208
24	H	0.084987	0	−0.09943	0.159465	0.000157	0.144925
25	H	0.155833	0	−0.03043	−0.2079	-2.3×10^{-5}	0.355682
26	H	0.069127	0	0.069964	0.05358	0.131787	0.131809
27	H	0.069126	0	0.06999	0.053625	−0.13173	0.131819
28	H	0.156973	0	0.162255	0.133737	−0.00015	0.357041
29	H	0.063251	0	−0.08074	0.010005	0.131151	0.125613
30	H	0.063227	0	−0.08083	0.00993	−0.13106	0.125606

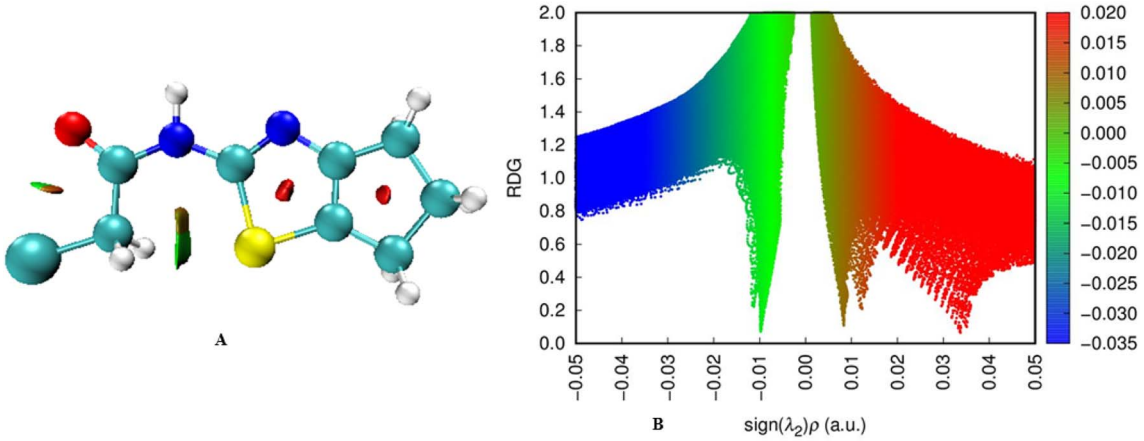

Fig. 29 (A) Non-covalent interaction (NCI) of compound **6h**. (B) Graphical representation of the reduced density gradient (RDG) of compound **6h**.

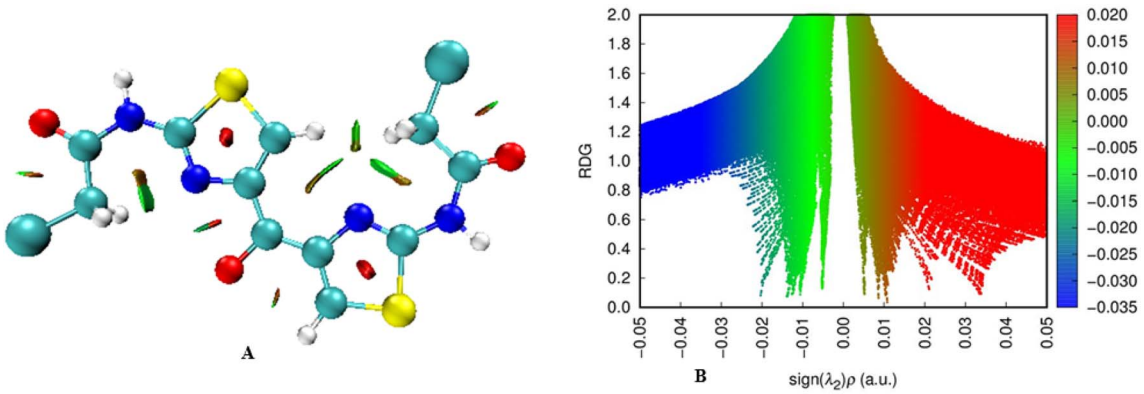

Fig. 30 (A) Non-covalent interaction (NCI) of compound **6i**. (B) Graphical representation of the reduced density gradient (RDG) of compound **6i**.

interactions. In the graphical representation, blue peaks represent the presence of attractive forces, red peaks indicate the presence of repulsive forces and the green areas indicate the presence of weak dispersive forces. The work was analyzed by the NCI and RDG performed using the Multiwfn program and isosurfaces analyzed using VMD, providing a close insight into the non-covalent interaction surface of compound **6i**.

3.5.9. Electron localization function (ELF) and localized orbital locator (LOL) analysis. In Fig. 31 the analysis of the electron localization function (ELF) and localized orbital locator (LOL) of compound **6h** are presented, which provide information about all electron pair localization and chemical bonding. Fig. 31 (part A) shows the ELF contour map with large values (dark areas around the carbon atoms), showing strong electron localization, which is usually attributed to bonding pairs or lone pairs. This visualization can be used to determine the areas of covalent bonding and electron density. The three-dimensional version of the LOL surface (top) and the associated 2D contour map (bottom), which increased the LOL values in both cases (darker colors), similarly indicate the localized regions of electrons, as shown in Fig. 31 (part B). The LOL analysis is an addition to the ELF since it highlights the presence of localized orbitals, especially within the bonding and non-bonding regions. Collectively, these roles use a detailed view to represent the electronic structure, which, in turn, is useful to make interpretations about the chemical bonding and reactivity of the molecular system and the distribution of lone pairs.

Fig. 32 represents the electron localization function (ELF) and localized orbital locator (LOL) calculations of the compound **6i** carried out using density functional theory (DFT) to investigate the electronic structure and bonding of the compound. Fig. 32 part (A) presents the ELF contour map, in which dense lines surrounding nitrogen, carbon and hydrogen atoms represent the regions of great electron localization including bonding and lone pairing regions. It is worthy to note that the high localization around the nitrogen atoms implies the existence of the lone-pair electrons, which adds to the electronic behavior of the compound **6i**. A 2D contour map of the LOL is presented in Fig. 32 (part B), and a 3D surface plot of the LOL is also shown, giving an idea of how localized orbitals are spatially distributed. The colored areas, particularly red and yellow domains, signal the great localization that usually pertains to bonding between atoms in the conjugated core of compound **6i**. The ELF and LOL represented in Fig.

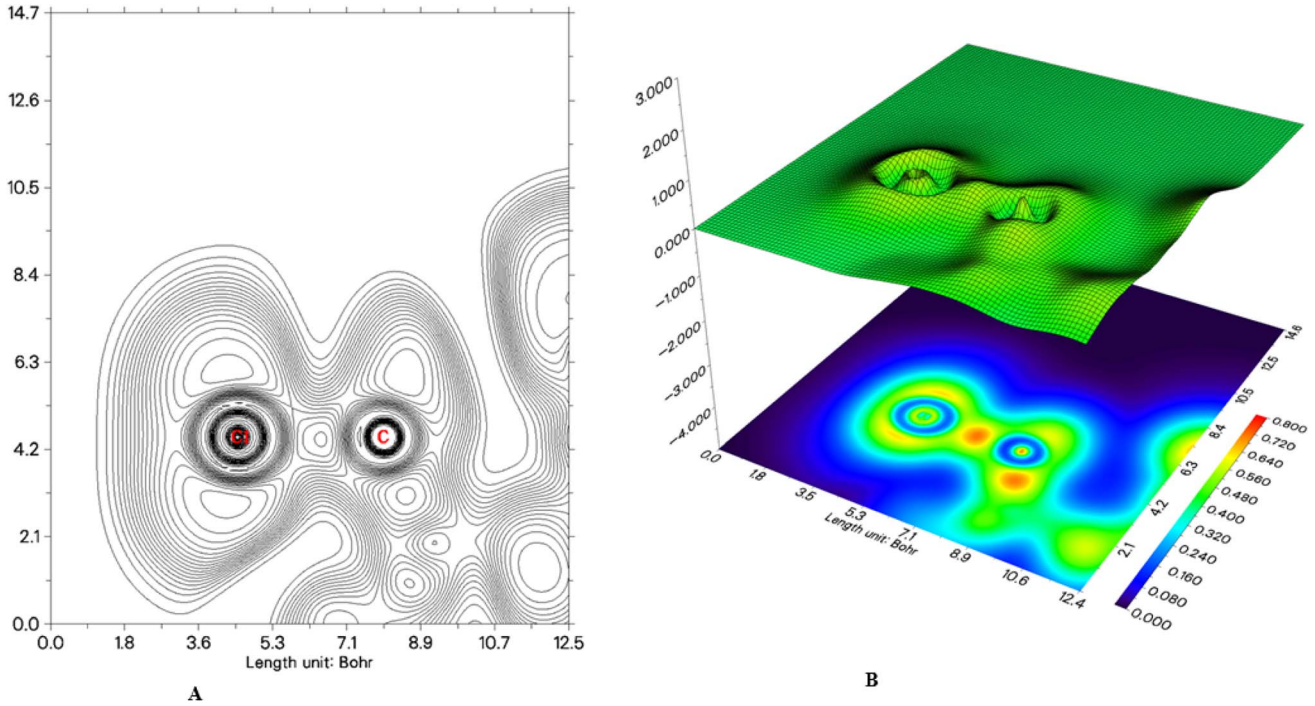

Fig. 31 (A) Graphical representation of the electron localization function (ELF) for compound **6h**. (B) Graphical representation of the localized orbital locator (LOL) for compound **6h**.

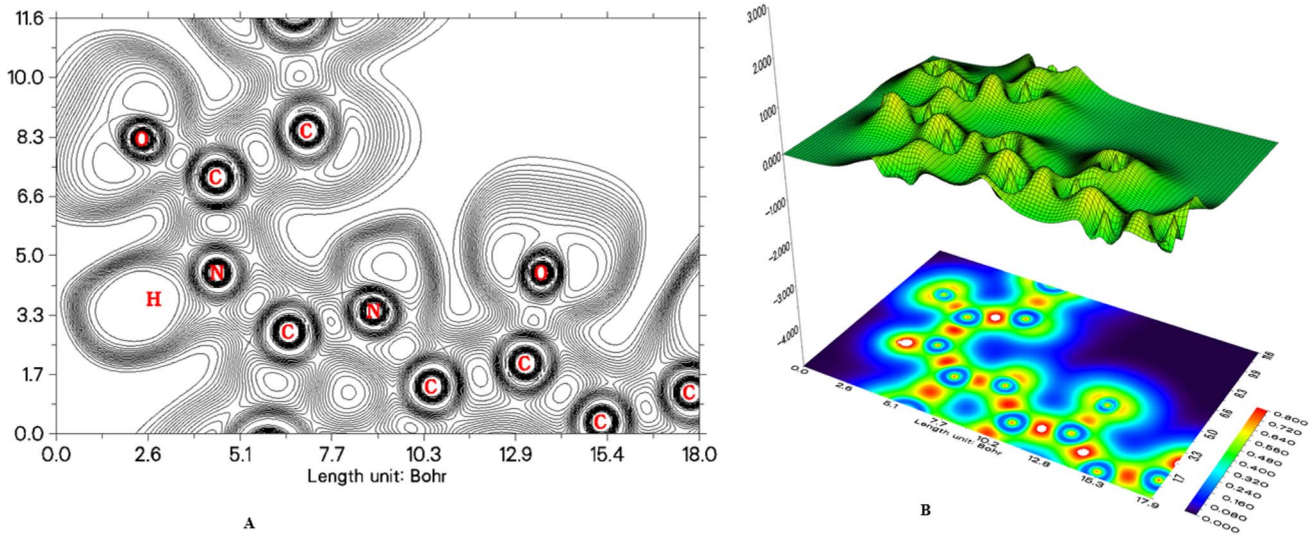

Fig. 32 (A) Graphical representation of the electron localization function (ELF) for compound **6i**. (B) Graphical representation of the localized orbital locator (LOL) for compound **6i**.

32 explains the better bonding system and delocalization of electrons which further assists in learning more on reactivity and stability of this compound.

4 Conclusion

Thiazole derivatives have been synthesized *via* two routes: the reaction of aminothiazole and chloroacetyl chloride leads to the formation of phenyl thiazole acetamide and the reaction of aminothiazoles and diazonium salt leads to the excellent yield of azothiazole. Two cell lines of chronic myeloid leukemia model, namely, K562 and U937 were used for biological potential evaluation against cancer. By using these cell lines, 2-amino-4-methylthiazole (**3a**), 2-amino-4-phenylthiazole (**3b**), bis(2-aminothiazole-4-yl)methanone (**3c**) and 2-chloro-*N*-(4-phenylthiazole-2-yl acetamide) (**6j**) compounds show poor results towards cytotoxicity. After the *in vitro* study, an *in silico* study was performed for further analyses of these thiazole

derivatives. The docking studies were performed to check the pharmacologically active compounds with four proteins. Six compounds (**3e**, **3f**, **6h**, **6i**, **6j** and 7) were screened out from the 2GQG protein, 6 compounds (**3b**, **3e**, **3d**, **6g**, **6h** and **6i**) from the 5MO4 protein, 4 compounds (**3b**, **3f**, **6h** and 7) from the 2AZ5 protein and 5 compounds (**3c**, **3f**, **6h**, **6i** and **6j**) from the 5MAR protein. The MMGBSA study showed excellent results with the 5MO4 protein. Further screening of two compounds (**6h** and **6i**) was carried out using density functional theory, as these two compounds showed a good binding affinity score with the receptor site of all proteins. The DFT analysis provided us the detail about structural parameters and molecular geometry. After that a research created between experimental and computational studies. Overall, the lead synthesized compounds **6h** and **6i** proved to be effective drugs for future use due to the enhanced activity and cost-effective method.

Author contributions

Zaheer Ahmad: supervision, editing, evaluation of results; Labaina Shakorr: synthesis, biological activity, drafting; Aneeqa Batool: library preparation, molecular docking; Nusrat Shafiq: conceptualization, paper drafting, write up, data analysis, literature and funding; Syeda Aaliya Shehzadi: two-way ANOVA application on activity data; Mohamed Mohany: helped reviewing and data analysis; Lei Zhang & Salim S. Al-Rejaie: validation, proof editing; Humaira Razzaq & Sajid Mahmood: resolution and alignment of all figures.

Conflicts of interest

The authors have no conflict of interest.

Data availability

All data files are available as supplementary information (SI). Supplementary information: Tables S1, S2, S3, S4 and S5. Fig S1–S31. All ^{1}H-NMR and ^{13}C-NMR spectra. See DOI: https://doi.org/10.1039/d5ra07232h.

Acknowledgements

The authors acknowledge and appreciate the Ongoing Research Funding Program (ORF-2025-120), King Saud University, Riyadh, Saudi Arabia. The authors thank the Pakistan Science Foundation (Grant # CRP/PSF/TH-22) for supporting this study.

References

1 E. Abele, R. Abele and E. Lukevics, Oximes of five-membered heterocyclic compounds with two heteroatoms 2: Reactions and biological activity, *Chem. Heterocycl. Compd.*, 2007, **43**, 945–977.

2 N. Siddiqui, M. F. Arshad, W. Ahsan and M. S. Alam, Thiazoles: A Valuable Insight into the Recent Advances and Biological Activities, *Int. J. Pharmaceut. Sci. Drug Res.*, 2009, **1**, 136–143.

3 N. Siddiqui, S. K. Arya, W. Ahsan and B. Azad, Diverse biological activities of Thiazoles: A Retrospect, *Int. J. Drug Dev. Res.*, 2011, **3**, 55–67.

4 S. J. Kashyap, V. K. Garg, P. K. Sharma, N. Kumar, R. Dudhe and J. K. Gupta, Thiazoles: having diverse biological activities Review Article, *Med. Chem. Res.*, 2012, **21**, 2123–2132.

5 D. Goulson, REVIEW: An overview of the environmental risks posed by neonicotinoid insecticides, *J. Appl. Ecol.*, 2013, **50**, 977–987.

6 L. M. Fox and L. D. Saravolatz, Nitazoxanide: a new thiazolide antiparasitic agent, *Clin. Infect. Dis.*, 2005, **40**, 1173–1180.

7 J. B. Sperry and D. L. Wright, Furans, thiophenes and related heterocycles in drug discovery, *Curr. Opin. Drug Discovery Dev.*, 2005, **8**, 723–740.

8 R. E. Dolle and K. H. Nelson, Comprehensive Survey of Combinatorial Library Synthesis: 1998, *J. Comb. Chem.*, 1999, **1**, 235–282.

9 C. Zhang, G. Li, C. Fan, J. Xu, J. Cao and N. L. Shen Liu, Comparison of efficacy of different route of administration of chemotherapy on unresectable, advanced gastric cancer, *World J. Surg. Oncol.*, 2012, **10**, 1–14.

10 S. Seth, A Comprehensive Review on Recent advances in Synthesis & Pharmacotherapeutic potential of Benzothiazoles, *Inflamm. Anti-Allergy Agents Med. Chem.*, 2015, **14**, 98–112.

11 F. Al-Omran, R. M. Mohareb and A. A. El-Khair, New route for synthesis, spectroscopy, and X-ray studies of 2-[aryl-(6′-hydroxy-4′,4′-dimethyl-2′-oxocyclohex-6′-enyl)methyl]-3-hydroxy-5,5-dimethylcyclohex-2-enone and 1,8-dioxo-octahydroxanthenes and antitumor evaluation, *Med. Chem. Res.*, 2014, **23**, 1623–1633.

12 U. Arshad, S. Ahmed, N. Shafiq, Z. Ahmad, A. Hassan, N. Akhtar, S. Parveen and T. Mehmood, Structure-Based Designing, Solvent Less Synthesis of 1,2,3,4-Tetrahydropyrimidine-5-carboxylate Derivatives: A Combined In Vitro and In Silico Screening Approach, *Molecules*, 2021, **26**, 1–22.

13 P. Schneider and G. Schneider, De novo design at the edge of chaos: Miniperspective, *J. Med. Chem.*, 2016, **59**, 4077–4086.

14 S. A. A. Anand, C. Loganathan, K. Saravanan and S. Kabilan, Comparison of molecular docking and molecular dynamics simulations of 1, 3-thiazin-4-one with MDM2 protein, *Int. Lett. Chem., Phys. Astron.*, 2015, **60**, 161–167.

15 S. Roy, R. Sharma and A. Kumar, 17 Molecular Docking and Molecular Dynamics in Signal Analysis, *Signal Analysis in Pharmacovigilance: Principles and Processes*, 2024, p. 210.

16 S. Chinnasamy, G. Selvaraj, A. C. Kaushik, S. Kaliamurthi, A. S. Nangraj, C. Selvaraj, S. K. Singh, R. Thirugnanasambandam, K. Gu and D.-q. Wei, Identification of potent inhibitors against Aurora kinase A using molecular docking and molecular dynamics simulation studies, *Preprints.org*, preprint, 2019, DOI: 10.20944/preprints201908.0238.v1.

17 O. O. Elekofehinti, I. R. Adetoyi, H. O. Popoola, F. O. Ayodeji, F. A. Taiwo, M. O. Akinjiyan, O. F. Koledoye, O. Iwaloye and A. E. Adegboyega, Discovery of potential epidermal growth

factor receptor inhibitors from black pepper for the treatment of lung cancer: an in-silico approach, *Silico Pharmacol.*, 2024, **12**, 28.

18 A. O. Fadaka, R. T. Aruleba, N. R. S. Sibuyi, A. Klein, A. M. Madiehe and M. Meyer, Inhibitory potential of repurposed drugs against the SARS-CoV-2 main protease: a computational-aided approach, *J. Biomol. Struct. Dyn.*, 2022, **40**, 3416–3427.

19 V. T. Sabe, G. F. Tolufashe, C. U. Ibeji, S. B. Maseko, T. Govender, G. E. Maguire, G. Lamichhane, B. Honarparvar and H. G. Kruger, Identification of potent L, D-transpeptidase 5 inhibitors for Mycobacterium tuberculosis as potential anti-TB leads: Virtual screening and molecular dynamics simulations, *J. Mol. Model.*, 2019, **25**, 1–16.

20 S. V. Pattar, S. A. Adhoni, C. M. Kamanavalli and S. S. Kumbar, In silico molecular docking studies and MM/GBSA analysis of coumarin-carbonodithioate hybrid derivatives divulge the anticancer potential against breast cancer, *Beni-Suef Univ. J. Basic Appl. Sci*, 2020, **9**, 1–10.

21 N. Muddagoni, R. Bathula, M. Dasari and S. R. Potlapally, Homology modeling, virtual screening, prime-MMGBSA, AutoDock-identification of inhibitors of FGR protein, *Biointerface Res. Appl. Chem.*, 2021, **11**, 11088–11103.

22 A. A. Braga, G. Ujaque and F. Maseras, A DFT study of the full catalytic cycle of the Suzuki− Miyaura cross-coupling on a model system, *Organometallics*, 2006, **25**, 3647–3658.

23 A. Tomberg, An introduction to computational chemistry using G09W and Avogadro software, *Gaussian 09w Tutorial*, 2013, pp. 1–36.

24 M. Zunita, M. David and W. Natola, Prediction of CO2 with amine functionalized ionic liquids interaction using density functional theory, *Case Stud. Chem. Environ. Eng.*, 2023, **8**, 100355.

25 S. M. Putra, T. K. Wungu and I. Arif, Ab-Initio Calculation of Chlorophyll-b UV-Vis Absorbance Spectra using Gaussian 09 based Density Functional Theory (DFT), *Int. J. Nanoelectron. Mater.*, 2021, **14**, 11–26.

26 G. Kotan and H. Yüksek, Experimental (Ft-Ir, Nmr) And Theoretical (B3pw91, B3lyp, Hf) Analyses Of 2-((3-Ethyl-4, 5-Dihydro-1h-1, 2, 4-Triazol-5-On-4-Yl)-Azomethine)-Benzoic Acid, *Caucasian J. Sci.*, 2019, **6**, 64–75.

27 M. Sheikhi, E. Balali and H. Lari, Theoretical investigations on molecular structure, NBO, HOMO-LUMO and MEP analysis of two crystal structures of N-(2-benzoyl-phenyl) oxalyl: A DFT study, *J. Phys. Theor. Chem.*, 2016, **13**, 155–169.

28 S. C. North, K. R. Jorgensen, J. Pricetolstoy and A. K. Wilson, Population analysis and the effects of Gaussian basis set quality and quantum mechanical approach: main group through heavy element species, *Front. Chem.*, 2023, **11**, 1152500.

29 H. Benaissi, M. Drissi, S. Yahiaoui, Y. Megrouss, A. Chouaih and F. Hamzaoui, Hirshfeld surface analysis, topological features and nonlinear optical properties of phthalonitrile derivative: low temperature experimental charge density and quantum chemistry studies, *J. Optoelectron. Biomed. Mater.*, 2018, **10**, 73–82.

30 G. Amudha, R. Santhakumari, D. Chandrika, S. Mugeshini, N. Rajeswari and S. Sagadevan, Growth, spectroscopic and Hirshfeld surface analysis on pyridine urea single crystal, *J. Mol. Struct.*, 2022, **1257**, 132606.

31 N. E. Amraoui and D. Hammoutè, DNA base pairs sensors: DFT, QTAIM and NCI-RDG study, *Comput. Chem.*, 2024, **12**, 75–90.

32 D. A. Dhas and S. Balachandran, Structural, Spectroscopic, and CH···O Hydrogen Bonding Interaction on Structure (Monomer and Dimer) Vibrational Spectroscopic, Fukui, NCI, AIM, and RDG Analysis Molecular Docking and Molecular Dynamic Simulation of Biological Active Pencycuron, *Polycyclic Aromat. Compd.*, 2023, **43**, 8494–8543.

33 S. Janani, H. Rajagopal, S. Muthu, S. Javed and A. Irfan, Structural, electronic properties (different solvents), chemical reactivity, ELF, LOL, spectroscopic insights, molecular docking and in vitro anticancer activity studies on methyl (4-nitro-1-imidazolyl) acetate, *J. Indian Chem. Soc.*, 2022, **99**, 100438.

34 F. Akman, A. Demirpolat, A. S. Kazachenko, A. S. Kazachenko, N. Issaoui and O. Al-Dossary, Molecular structure, electronic properties, reactivity (ELF, LOL, and Fukui), and NCI-RDG studies of the binary mixture of water and essential oil of Phlomis bruguieri, *Molecules*, 2023, **28**, 2684.

35 D. P. Khrustalev, A. A. Suleimenova and S. D. Fazylov, Synthesis of 2-amino-4-phenylthiazole under Conditions of microwave Irradiation, *Russ. J. Appl. Chem.*, 2008, **81**, 863–900.

36 J. Sun, B. R. Liu, W. J. Hu, L. X. Yu and X. P. Qian, In vitro anticancer activity of aqueous extracts and ethanol extracts of fifteen taditional Chinese medicines on human digestive tumor cell lines, *Phytother Res.*, 2007, **21**, 1102–1104.

37 Y. Ohsaki, A. F. Gazdar, H.-C. Chen and B. E. Johnson, Antitumor activity of magainin analogues against human lung cancer cell lines, *Cancer Res.*, 1992, **52**, 3534–3538.

38 Y. K. Janapati and S. Junapudi, Progress in experimental models to investigate the in vivo and in vitro antidiabetic activity of drugs, *Anim. Models Exp. Med.*, 2024, **7**, 297–309.

39 J. J. Sahayarayan, K. S. Rajan, M. Nachiappan, D. Prabhu, R. G. R. Rao, J. Jeyakanthan, A. H. Mahmoud, O. B. Mohammed and A. M. Morgan, Identification of potential drug target in malarial disease using molecular docking analysis, *Saudi J. Biol. Sci.*, 2020, **27**, 3327–3333.

40 B. K. Kumar, n. Faheem, K. V. G. C. Sekhar, R. Ojha, V. K. Prajapati, A. Pai and S. Murugesan, Pharmacophore based virtual screening, molecular docking, molecular dynamics and MM-GBSA approach for identification of prospective SARS-CoV-2 inhibitor from natural product databases, *J. Biomol. Struct. Dyn.*, 2022, **40**, 1363–1386.

41 P. T. Tasli, Ç. K. Atay, T. Demirturk and T. Tilki, Experimental and computational studies of newly synthesized azo dyes based materials, *J. Mol. Struct.*, 2020, **1201**, 127098.

42 G. Khanum, A. Ali, S. Shabbir, A. Fatima, N. Alsaiari, Y. Fatima, M. Ahmad, N. Siddiqui, S. Javed and M. Gupta, Vibrational Spectroscopy, Quantum Computational and

Molecular Docking Studies on 2-[(1H-benzimidazol-1-yl)-methyl] benzoic acid, *Crystals*, 2022, **12**, 337.

43 S. Rekha, S. Tamilselvan, V. Vetrivelan, J. C. Mishma, S. Kadaikunnan, G. Abbas and S. Muthu, Effect of different solvents, molecular level vibrational energies, electronic, electrostatic, donar-acceptor and pharmaceutical studies on 3-methoxy phenyl acetonitrile-anti depressant agent, *J. Mol. Liquids*, 2023, **386**, 122308.

44 K. Chaitanya, C. Santhamm, K. Prasad and V. Veeraiah, Molecular structure, vibrational spectroscopic (FT-IR, FT-Raman), first order hyperpolarizability, NBO analysis, HOMO and LUMO analysis, thermodynamic properties of 3, 5-dimethylbenzophenone by ab inito HF and density functional method, *J. At. Mol. Sci.*, 2012, **3**(1), 1–22.

45 Z. Demircioğlu, C. A. Kaştaş and O. Büyükgüngör, Theoretical analysis (NBO, NPA, Mulliken Population Method) and molecular orbital studies (hardness, chemical potential, electrophilicity and Fukui function analysis) of (E)-2-((4-hydroxy-2-methylphenylimino) methyl)-3-methoxyphenol, *J. Mol. Struct.*, 2015, **1091**, 183–195.

46 T. B. Issa, F. Sayari, H. Ghalla and L. Benhamada, Synthesis, crystal structure, DFT calculations and molecular docking of L-pyroglutamic acid, *J. Mol. Struct.*, 2019, **1178**, 436–449.

47 K. Ramirez-Balderrama, E. Orrantia-Borunda and N. Flores-Holguin, Calculation of global and local reactivity descriptors of carbodiimides, a DFT study, *J. Theor. Comput. Chem.*, 2017, **16**(3), 1750019.

48 S. Parveen, A. Batool, N. Shafiq, M. Rashid, A. Sultan, G. F. Wondmie, *et al.,* Developmental landscape of computational techniques to explore the potential phytochemicals from Punica granatum peels for their antioxidant activity in Alzheimer's disease, *Front. Mol. Biosci.*, 2023, **10**, 1252178.

49 B. Chandralekha, R. Hemamalini, S. Muthu and S. Sevvanthi, Spectroscopic (FT-IR, FT-RAMAN, NMR, UV–Vis) investigations, computational analysis and molecular docking study of 5-bromo-2-hydroxy pyrimidine, *J. Mol. Struct.*, 2020, **1218**, 128494.

50 E. A. Bisong, H. Louis, T. O. Unimuke, J. O. Odey, E. I. Ubana, M. M. Edim, et al. Vibrational, electronic, spectroscopic properties, and NBO analysis of p-xylene, 3, 6-difluoro-p-xylene, 3, 6-dichloro-p-xylene and 3, 6-dibromo-pxylene: DFT study, *Heliyon*, 2020, **6**(12), e05783.

51 G. Bella and A. Rotondo, Theoretical prediction of 13C NMR spectrum of mixed triglycerides by mean of GIAO calculations to improve vegetable oils analysis, *Chem. Phys. Lipids*, 2020, **232**, 104973.